Fabrication and Integration of Nanostructured Optical Devices

Adam Filipkowski

A thesis submitted for the degree of

Doctor of Philosophy

Heriot-Watt University

School of Engineering and Physical Sciences

June 2015

Abstract

The main goal of this thesis is the numerical and experimental verification of the concept of nanostructured micro-optical elements integrated into an optical fibre. The elements are fabricated with a stack and draw technique. This technology, based on the well-known method of photonic crystal fibres (PCFs) production, allows the fabrication of Nanostructured Gradient Index (nGRIN) microlenses and axicons with individual nanorods with diameter of 100-300nm. The necessary parameters of materials used in stack and draw method are described and two glasses are chosen for the nanostructured elements fabrication. The procedure of synthesis of clear and doped Poly(methyl methacrylate) (PMMA) is introduced, which will allow using PMMA in the future in stack and draw technique. Numerical simulations of a Gaussian beam focusing nGRIN microlenses attached to optical fibres are performed using a FFT BPM method. This shows that nGRIN microlenses can be described using the effective refractive index also in the case of the optical fibre illumination. The procedure of fabricating, cutting and polishing of elements 125μm in diameter and 20-60μm long is introduced and explained. Both simulation and experimental results show that the fabricated nanostructured lenses and axicons focus light for the fibre source with wavelength 1550nm.

Acknowledgements

First of all, I would like to thank Prof. Mohammad R. Taghizadeh and Prof. Ryszard Buczynski for recruiting me into the project, and furthermore I would like to thank them for their great patience, kindness and support during the difficult moments of my work.

Many people helped me during my studies and it is not easy to mention them all here by name. I want to express a particular gratitude to Darek Pysz and Irek Kujawa from Institute of Electronic Materials Technology (ITME) as well as Neil Ross for providing me with training in a micro-optical technology. I also want to express my gratitude to Dr Andrew Waddie, who greatly helped me in the numerical and theoretical parts of the work. I am also grateful to my colleagues Jedrzej Nowosielski and Adrian Dziupalski for invaluable help during this work.

Last but not least, I want to thank my wife Maria for support and a lot of patience and understanding.

ACADEMIC REGISTRY
Research Thesis Submission

Name*:*	Adam Stefan Filipkowski		
School/PGI:	School of Engineering and Physical Sciences		
Version: *(i.e. First, Resubmission, Final)*	Final	Degree Sought (Award **and** Subject area)	PhD, Physics

Declaration

In accordance with the appropriate regulations I hereby submit my thesis and I declare that:

1) the thesis embodies the results of my own work and has been composed by myself
2) where appropriate, I have made acknowledgement of the work of others and have made reference to work carried out in collaboration with other persons
3) the thesis is the correct version of the thesis for submission and is the same version as any electronic versions submitted*.
4) my thesis for the award referred to, deposited in the Heriot-Watt University Library, should be made available for loan or photocopying and be available via the Institutional Repository, subject to such conditions as the Librarian may require
5) I understand that as a student of the University I am required to abide by the Regulations of the University and to conform to its discipline.

* *Please note that it is the responsibility of the candidate to ensure that the correct version of the thesis is submitted.*

Signature of Candidate*:*		Date:	

Submission

Submitted By *(name in capitals):*	
Signature of Individual Submitting:	
Date Submitted:	

For Completion in the Student Service Centre (SSC)

Received in the SSC by *(name in capitals):*			
1.1. Method of Submission *(Handed in to SSC; posted through internal/external mail):*			
1.2. E-thesis Submitted (**mandatory for final theses)**			
Signature:		Date:	

Table of Contents

AUTHOR'S JOURNAL CONTRIBUTIONS

1) A. Filipkowski, D. Pysz, P. Gdula, K. Welikow, K. Harasny, A. J. Waddie, K. Borzycki, A. Kraft, R. Piramidowicz, R. Stepien, M. R. Taghizadeh, R. Buczynski, *Development of large core microstructured polymer optical fiber*, Proc. SPIE 8426, Microstructured and Specialty Optical Fibres, 842616 (2012)

2) J. Nowosielski, J., R. Buczynski, A. J. Waddie, A. Filipkowski, D. Pysz, A. McCarthy, R. Stepien, M. R. Taghizadeh, *Large diameter nanostructured gradient index lens*, Optics Express 20(11), 11767-11777 (2012)

3) R. Buczynski; A. J. Waddie; J. Nowosielski; A. Filipkowski; D. Pysz; R. Stepien; M. R. Taghizadeh, *Development of elliptical nanostructured gradient index microlens*, Proc. SPIE 8902, Electron Technology Conference 2013, 890214 (2013)

4) R. Buczyński A. J. Waddie; J. Nowosielski; A. Filipkowski; I. Kujawa; D. Pysz; R. Stępień; M. R. Taghizadeh, *Beam propagation in all-glass nanostructured gradient index microlenses*, 18th Microoptics Conference (MOC), 1-2 (2013)

5) D. Pysz, I. Kujawa, R. Stępień, M. Klimczak, A. Filipkowski, M. Franczyk,

L. Kociszewski, J. Buźniak, K. Haraśny, R. Buczyński, *Stack and draw fabrication of soft glass microstructured fiber optics,* Bulletin of the Polish Academy of Sciences, Technical Sciences, 62(4) (2014)

6) R. Buczyński, A. Filipkowski; B. Piechal; D. Pysz; M. Klimczak; B. Siwicki; A. J. Waddie; M. R. Taghizadeh; R. Stępień, *Nanostructured gradient index microoptics*, 17th International Conference on Transparent Optical Networks (ICTON), 1 – 4 (2015)

7) A. Filipkowski, B. Piechal, D. Pysz, R. Stepien, A. Waddie, M. R. Taghizadeh, R. Buczynski, *Nanostructured gradient index microaxicons made by a modified stack and draw method*, Optics Letters 40 (22), 5200-5203 (2015)

8) R. Buczynski, A. Filipkowski, A. J. Waddie, B. Piechal, J. Nowosielski, D. Pysz, R. Stepien, M. R. Taghizadeh, *Large elliptical nanostructured gradient-index microlens*, Applied Optics 55 (1), 89-94 (2016)

1. INTRODUCTION

The main focus of this thesis is the numerical and experimental verification of the concept of small nanostructured optical elements integrated with optical fibres. Most of the work concerns components with an external diameter in the range of 120-130μm and an overall length not exceeding 200μm. The internal nanostructure has a diameter in the range 19-22μm with feature sizes in the range of 100-300nm.

The fundamental concept for this work was provided by Professors M.R. Taghizadeh and R. Buczyński with the initial research of the nanostructured elements being performed by J. Nowosielski [1.1] and F. Hudelist [1.2]. In previous works the viability of the large (diameter ~130μm) step index (seven discrete refractive index steps) lenses in free space was proven. In this thesis I focus on the next step and further develop optical nanostructures. The principle of operation of the nanostructured gradient-index (nGRIN) optical elements can be described by an effective medium theory (EMT) which is a basic mixing rule inspired by the Maxwell-Garnet formula [1.3]. This method can be utilised provided the feature size of the nanostructure is sufficiently smaller than the wavelength of the propagating light. In this approach, the effective permittivity can be simply approximated by the volume average of the permittivity in the neighbourhood of a given point. The use of the EMT allowed the design of various nanostructured micro-optical elements such as lenses and axicons from only two glasses with different refractive indexes.

The nanostructured elements were fabricated using the stack-and-draw technique which is commonly used in photonic crystal fibre production. The novelty in this thesis of the nanostructured optical elements lies in the use of this technique for the fabrication of other optical elements i.e. nGRIN optical elements. The general idea behind this method is the construction of the desired structure on a macroscopic level, using rods with a diameter of ~1mm. The rods, with different refractive indices, are arranged according to a designed pattern and the whole structure is drawn down using a fibre drawing tower. The cross-section of the structure is scaled down during the drawing. Usually the drawing process is repeated in order to reach the desired diameter of the final structure.

This thesis expands upon this basis to allow the creation of small optical elements that could be easily integrated in fibre optic systems. In order to achieve this small diameter (~20μm) elements had to be designed and fabricated with flat-parallel surfaces.

Chapter 2 covers the background of the GRIN elements fabrication. Ion exchange technique, chemical vapour deposition, direct writing in a diffusion-driven photopolymer as the most popular methods of GRIN fabrication are described. In section 2.4 nanostructured GRIN elements fabricated by other research groups are described.

In Chapter 3 the modelling method used in this thesis is introduced. In section 3.1 theoretical predictions based on the ray optics concerning size and refractive index distribution of the optical lenses are described. Section 3.2 details the refractive index distribution and ray optics of axicons. In section 3.3 the chosen modelling method is introduced. In this thesis the Fast Fourier Transform Beam Propagation Method (FFT BPM) was used. The software utilised was developed by Andrew Waddie at the Heriot-Watt University. The method is based on Helmholtz equation. This method was chosen as it is much less resource consuming and it can handle much larger structures than Finite Differential Time Domain (FDTD) method. A scalar implementation of FFT BPM is exploited. In section 3.3 BPM simulations are shown for the propagation of gaussian beam through ideal GRIN lens and ideal GRIN axicon. In those simulations coupling losses between various elements of the simulated setup are not considered.

In Chapter 4 numerical verification of the optical elements attached to the optical fibre is performed. In section 4.1 various lengths of a lens with continuous refractive index distribution are tested. The tests are performed for 20μm, 40μm and 60μm lens length, which represents 0.066, 0.13 and 0.20 of the pitch of the selected lens. In section 4.2 the same simulations are performed for 20μm, 40μm and 60μm length of the axicon with continuous refractive index distribution.

In Chapter 5 shows the discretisation process that allows the creation of nanostructured lenses based on the desired ideal refractive index distribution. Section 5.1 briefly introduces the effective medium theory, which is the basis for our discretisation method. According to that theory a continuous refractive index distribution in a given optical element can be substituted with a discrete subwavelength distribution of glass rods with only two refractive indexes. In sections 5.2 and 5.3 the Simulated Annealing (SA) algorithm and its use in the design of nanostructured micro-optics is described. The original algorithm was developed by F. Hudelist and J. Nowosielski for calculating rod distribution in materials with uniform refractive index. For the purposes of this thesis the algorithm was modified in order to obtain rod distribution according to the specified refractive index profile, e.g. refractive index profile of a GRIN lens, or axicon. As direct analytical or numerical calculation of the rod arrangement corresponding to the desired

distribution of the effective refractive index is not possible, a stochastic optimization method is needed. The SA algorithm is useful when there is an optimisation problem with a large number of degrees of freedom. In the case of the nanostructured micro-element the refractive index of each rod may be thought of as one degree of freedom. Section 5.4 shows FFT BPM simulations of light propagation through optical elements with continuous refractive index distribution and comparison to the discreet designs obtained through Simulated Annealing algorithm.

In Chapter 6 materials used in nanostructure fabrication are discussed. In the section 6.1 various glasses that were available are introduced and criteria that the glasses need to fulfil are explained Section 6.2 of this Chapter deals with proof of concept for the future use of polymers in nanostructure fabrication. Section 6.2.1 describes in detail the free radical polymerisation method utilised in this thesis. The polymerisation method utilised in this thesis is an optimisation of the method developed by Adrien Maniquet, a masters student at Heriot-Watt University. The goal of this thesis was to obtain two PMMA based polymers with similar thermal and mechanical parameters but different refractive indexes. Section 6.2.2 describes polymerisation of the clear PMMA material, while section 6.2.3 describes changes introduced to the polymerisation process in order to obtain doped PMMA. In section 6.3 two tests performed on the PMMA materials are described. In the first test only clear PMMA is used to fabricate a photonic structure, in the second test clear and doped PMMA were used to fabricate an optical fibre. In both tests fibres were constructed using stack and draw method which was tested and proven for the glasses. These tests show the possibility of using two distinct polymer materials for creating various micro structured components utilising stack and draw method.

In Chapter 7 the fabrication process of the various optical elements used in this thesis is described. In section 7.1.1 details of the assembly process of such preforms, and the limitations of this technology are introduced. In section 7.1.2 the drawing tower and fibre fabrication process are explained. In the two-stage drawing process elements with structure size about 20μm in diameter can be fabricated as explained in section 7.1.3. When the drawing process consists of three stages the larger structures can be obtained. In section 7.1.4 fabrication of such an element - the elliptical lens with external diameter of 125×75μm is described. Such elements can be successfully cut, ground and polished in order to create optical elements with previously designed external dimensions. The two step process described in sections 7.2.1 and 7.2.2 allows preparing simultaneously up to 30 elements for integration using equipment available at the time of writing this

thesis. Each element has similar diameter as typical optical fibre – 125μm, and length in range from 10μm to 200μm. The last section describes the integration process which allows the optical elements to be attached to the optical fibres with a precision of ± 2μm. To achieve this precision active alignment of the optical element with the optical fibre has to be used.

In Chapter 8 the first test of the new optical element is described. The simulations and experimental verification was conducted for a large elliptical lens. This is a direct continuation of previous work done by J. Nowosielski [1.1]. As the lens tested in this Chapter is larger than all of the other optical elements described in this thesis, measuring ~125×75μm, it could not be attached to the optical fibre. In section 8.1 we described numerical verification of the step index elliptical lens. The dimensions of the simulated lenses are similar to the fabricated lenses – 125×75μm. Computer simulations are performed for the infinite lenses in order to obtain pitch lengths for step index and ideal lenses. Further simulations show light propagation through the 140μm long lens, again both for ideal and step index lens. Section 8.2 shows experiments done to the fabricated lenses. Initially 140μm long lens was tested. A second set of experiments was performed for the lens that had length equal to 170μm. Experiments were conducted for the 630nm and 1550nm wavelengths of the incident light.

In Chapter 9 computer simulations and experimental verification of a small nanostructured lens are shown. Section 9.1 describes the simulations performed in order to find the best spacer length for a 20μm in diameter lens attached to the optical fibre. The second sets of simulations in this section shows light propagation after nanostructured lenses of various lengths. In section 9.3 the results of experimental verification are shown. A nanostructured lens, with a diameter around 20μm was attached to an optical fibre. The nanostructured lens is 11.96μm long and with spacer 71.46μm long. Experiments were conducted for the 1550nm incident light.

In Chapter 10 for final testing of the new optical elements simulations and experimental verification of the nanostructured axicon was performed. The experimental and computational set up was the same as described in Chapter 9. The first series of simulations was performed in order to find the best axicon length and the length of the spacer used between the axicon and fibre as described in section 10.1. The section 10.2 describes the development process. In section 10.3 the results of experimental verification are shown. A nanostructured axicon, with a diameter of around 20μm was attached to an optical fibre. Experiments were performed for two axicons. The first

axicon tested was 22.75µm long with a spacer 17.58µm long. The second axicon was 32µm long, with an attached spacer 78µm long.

1.1. References

[1.1] J. M. Nowosielski, *Nanostructured Birefringent and Gradient-Index Micro-Optical Elements*, Thesis collection, Heriot Watt University (2014)

[1.2] F. Hudelist, *Design and Characterisation of Nanostructured Gradient Index Lenses*, Thesis collection, Heriot Watt University (2010)

[1.3] A. Sihvola, *Electromagnetic Mixing Formulas and Applications*, ISBN 0-85206-772-1, London: The Institution of Electrical Engineers (1999)

2. GRIN OPTICAL ELEMENTS

The development of GRIN optical technology started over 100 years ago, with the Maxwell fisheye lens, which was never fabricated [2.1]. In 1905 Wood's published text [2.2] indicating the sinusoidal propagation of light through GRIN rod and constructed a GRIN lens [2.3] made of gelatine. Recently, with the advances in micro-fabrication and development of micro-optics, the GRIN lenses research is expanding, such as Moor and his research group studies on GRIN optical [2.4] elements. A more complete review of GRIN technology, can be seen in paper by Borrelli [2.5]

Gradient-index (GRIN) microlenses are optical elements in which light is deflected by a refractive index gradient within the lens body. This differs from surface profile microlenses in which light is refracted because of the overall lens shape. The GRIN lenses can be grouped depending on the refractive index distribution. GRIN rod lenses (fig. 2.1a) have refractive index distribution rotationally symmetrical along the optical axis [2.4]. Cylindrical GRIN lenses (fig. 2.1b) have parabolic refractive index distribution in one direction perpendicular to the optical axis and constant in the direction of the optical axis [2.6].

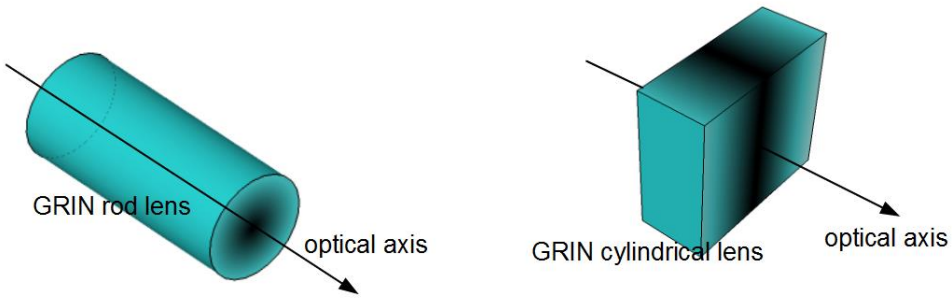

Figure 2.1 - (a) GRIN rod lens, (b) GRIN cylindrical lens. Refractive index gradient is illustrated with colour.

Currently the most popular method for obtaining the structured GRIN lenses is based on photonic crystals (PCs). Photonic crystal is a name used for periodic dielectric materials, which are often used as optical elements [2.8-2.10]. By combining graded index lenses with photonic crystals the concept of nonuniform 2D PCs is realised. Centeno *et al*. first used the name graded (index) photonic crystals, in 2006, for such photonic structures [2.11, 2.12]. In their papers refractive index profiles of the lenses are obtained by

changing the lattice spacing perpendicular to the light propagation (fig. 2.2). In literature similar structures can be found which can act as GRIN lenses [2.13, 2.14]. If the pitch of the PC lattice is sufficiently subwavelength, it can be described by the effective medium theory as leading to changes in the refractive index distribution. Kurt *et al*. proposed GRIN photonic crystal with varied pitch [2.12] and implemented it for the microwave wavelengths. The structure is built out of aluminium rods, which can be considered as dielectric material for the microwaves. Those rods are subwavelength in diameter, with the filling factor highest at the centre of the photonic crystal (Fig. 2.2a). Light focusing properties of a GRIN PC are shown in Fig. 2.2b.

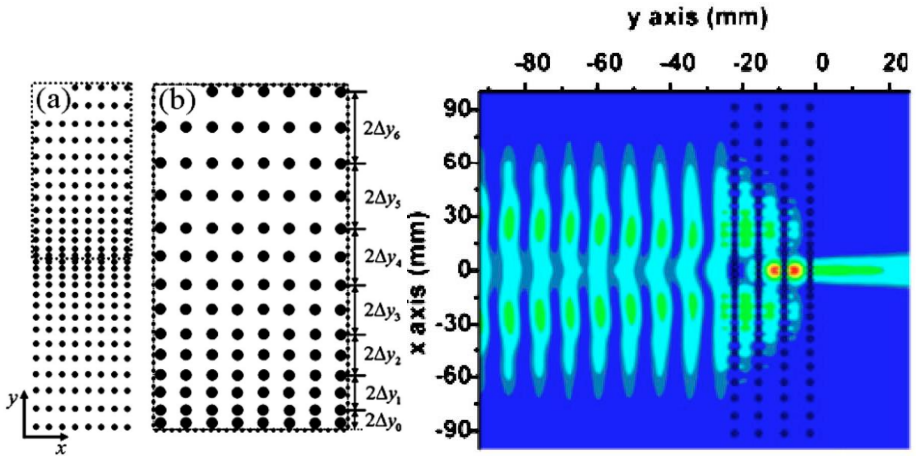

(a) (b)

Figure 2.2 - (a) Schematic of the GRIN PC. (b) Electric field distribution within GRIN PC [2.12].

C. Tan *et al.* [2.13] proposed fabrication of the gradient of the effective refractive index in the GRIN PC by using laser interference lithography (LIL). The structure described consists of rods arranged in a square array, which have varied diameters from 228nm in the centre to 70nm at the sides. During the LIL process four laser beams create an interference pattern in the recording material. In places where the beam interference intensity is higher than a certain material threshold there is a different refractive index to the rest of the material.

In paper [2.14] Gaufillet *et al.* describes the design and the experimental verification of a graded index photonic crystal lens. The refractive index gradient has been designed so that the flat-parallel lens converts the wave issued from a point source into a plane wave, which means that it operates as a convex lens. The gradient of index results from varying the filling factor of the photonic crystal in the direction perpendicular to that of the propagation of the electromagnetic field [2.14].

The GRIN PCs can be also used for creation of negative index material to act as a convex lens. A.O. Pinchuk et al. reports the design of the lens with its refractive index profile in the transverse direction to the propagating light [2.15]. This means that the modulus of the refractive index is smallest at the centre of the lens and increases towards the edges, which stands in contrast to a regular graded index lens whose index profile has a maximum at the centre of the GRIN rod. Such a negative profile can be obtained by increasing the air-hole radius from the centre towards the edges of the GRIN rod [2.16]. This lens was only verified numerically, but the simulations were performed to analyse the focusing properties of various graded negative profiles lenses over a range of frequencies [2.15]. Those simulations proved that a negative GRIN PC lens can reduce the chromatic aberration and can be used in focusing of parallel incident light.

GRIN PCs can be made using semiconductor fabrication technologies. Currently there are several methods of fabricating glass or polymer based GRIN lenses with the required refractive index distribution:

1) Ion exchange technique,
2) Chemical vapour deposition,
3) Sol-Gel Technique,
4) Reactive Ion Etching, and
5) Direct writing.

2.1. Ion exchange technique

The ion exchange technique is the best developed method of GRIN lens fabrication [2.6, 2.18, 2.19]. In this method a glass is shielded with a mask with small circular holes that define the microlens. The shielded glass is lowered into a bath of molten salt. The metal ions of the salt diffuse into the glass at high temperature (e.g. 370°C [2.4]). The rate of ion exchange at a given location and the resulting change in refractive index depends on the electrochemical activities between the exchanged ions, strength of bonds of the alkali ions in the used glass and the ion mobility within the glass [2.4]. This process leads to the desired change of the refractive index with the increased distance in the glass from the surface.

Both axially [2.6] and radially symmetrical [2.19] lenses can be obtained using this method. By using elliptical openings in the mask it is possible to fabricate astigmatic lenses, also in a planar substrate, a whole 2D array of planar GRIN lenses can be fabricated [2.20].

Modifications to this process can be applied to optimize the resulting index distribution in the fabricated lens. In a paper by Bahr [2.21] the mask structured ion exchange (MSI) is described. A lithographically structured mask is used to enhance the control over the three-dimensional index distribution. In work by Oikawa [2.22] field assisted ion exchange is described. In this method the ion mobility is enhanced by the use of an electric field. This filed is positioned at the interface between the substrate and the salt melt and it accelerates the movement of the ions from the melt into the substrate at the same time as it increases the penetration depth of the ions.

2.2. Chemical vapour deposition

A less popular method of GRIN fabrication is Chemical vapour deposition (CVD) [2.4]. In this method a glass tube is used as a substrate for the GRIN fabrication. On this substrate layers of glass with different refractive indices are deposited, which results in a structure continuous along optical axis and with rotational symmetry. The preform fabricated using this method has diameter around 1cm. It is drawn in a drawing tower in order to obtain the target diameter, typically in the order of 100μm. This difference of diameters produces subwavelength thickness of a single deposited glass layer. Drawn fibre can be cut into short pieces which can act as GRIN rod lenses.

In paper [2.23] Reed introduces microprobes for low-coherence interferometry fabricated using CVD. The described GRIN fibre lenses have a nearly parabolic negative refractive index profile, an outer diameter in the range 100 - 130μm and a GRIN fibre core diameter of 70 - 125μm. This GRIN fibre lenses are spliced to the single mode fibre (SMF).

2.3. Sol-Gel Technique

A sol-gel method for making a GRIN rod lens was developed by Shingyouchi *et al.* [2.27, 2,28]. In this method tetramethylorthosilicate (TMOS) is combined with germanium tetraethoxide (Ge(OEt)4), ethanol, EtOH, water, and hydrochloric acid. In this mixture gel particles are formed by germanium and silicon. The gel is then placed in water to leach out some of the germanium and washed in methanol to fix the germanium concentration gradient. This solution is then dried and sintered into gradient index glass [2.24]. Shingyouchi *et al.* also used this method to create gel using titanium and silica [2.26]. In both germanium and titanium based gels, the leaching was considered to proceed by a diffusion, as only germanium or titanium was detected in the solution after leaching [2.30, 2.31]. The process in this method may be used for the preparation of large GRIN rod lenses [2.25]. By leaching for 20 hours a wet gel about 6mm in diameter and

30mm in length and then sintering it at 1200°C a rod of about 2mm in diameter with the refractive index at the centre axis of 1.491 and a Δn of 0.013 was obtained [2.29 - 2.31]. Additionally, Caldwell *et al*. [2.27] studied the preparation of GRIN glass rods from ternary and quaternary based gels using techniques similar to that of Shingyouchi *et al.* Most of the GRIN glass rods fabricated using this method were about 4.5 mm in diameter with a Δn in range from 0.013 to 0.03. It takes about 5 – 7 days to fabricate GRIN rods.

2.4. Direct writing

Direct writing techniques make use of precision-steered beams to locally expose photoresist films, which results in change of the refractive index at the exposed spot. Arbitrary index structures can be achieved by creating different beam intensity patterns. This is achieved by changing the size and power of the writing beam and the exposure time [2.28].

In paper [2.29] Ye *et al.* proposed a method based on exposing photopolymer to a CW laser. The photopolymer layer 1 mm thick was positioned between two glass slides mounted on a high precision 3D translation stage. By moving the photopolymer in a preselected pattern a refractive index pattern is created. The process is ended when the whole area of the photopolymer is exposed to uniform light. This cures the whole lens area. Using this technique, it is possible to produce GRIN lens which are 40 to 1000μm in diameter, with the magnitude of refractive index change around 0.001.

Direct writing techniques are of particular interest for the fabrication of planar continuous relief and hybrid microlenses and are suitable for fabrication of lenslet arrays. Depending on the photoresist used various methods for the direct writing with the commercially available, semiconductor lithography equipment can be used. Those methods include: focused ion beam writing [2.30], electron beam [2.31] and direct laser writing [2.28].

2.5. References

[2.1] C. Gomez-Reino, M. V. Perez, C. Bao, *Gradient-Index Optics: Fundamentals and Applications*, ISBN 978-3-662-04741-5, Springer-Verlag Berlin Heidelberg (2002)

[2.2] R. A. Wood, *Physical Optics*, The Macmillan Company (1905)

[2.3] N. Morton, *Gradient refractive index lenses*, Physics Education, 19, 86-90 (1984)

[2.4] D. T. Moore, *Gradient index optics: a review*, Appl. Opt. 19 (7), 1035–1038 (1980)

[2.5] N. F. Borrell, *Micro-optics Technology*, Marcel Dekker Inc., New York, Basel, 59–105 (1999)

[2.6] B. Messerschmidt, T. Possner, R. Goering, *Colorless gradient-index cylindrical lenses with high numerical apertures produced by silver-ion exchange*, Applied Optics, 34 (34), 7825-7830 (1995)

[2.7] J. D. Joannoupoulos, P. R. Villeneuve, S. Fan, *Photonic crystals: putting a new twist on light*, Nature, 386, 143-149 (1997).

[2.8] H. Benisty, J. M. Lourtioz, A. Chelnokov, S. Combrie, X. Checoury, *Recent advances toward optical devices in semiconductor-based photonic crystals,* Proceedings of the IEEE, 94, 997-1023 (2006).

[2.9] B. S. Song, S. Noda, T. Asano, *Photonic devices based on in-plane hetero photonic crystals*, Science 300, 1537 (2003).

[2.10] E. Centeno, D. Cassagne, *Graded photonic crystals*, Opt. Lett., 74, 2278-2280 (2005).

[2.11] E. Centeno, D. Cassagne, J. P. Albert, *Mirage and superbending effect in two-dimensional graded photonic crystals*, Phys. Rev. B, 73, 235119-235119 (2006).

[2.12] H. Kurt, E. Colak, O. Cakmak, H. Caglayan, E. Ozbay, *The focusing effect of graded index photonic crystals,* Applied Physics Letters, 93 (17), 171108 (2008).

[2.13] C. Tan, T. Niemi, C. Peng, M. Pessa, *Focusing effect of a graded index photonic crystal lens,* Optics Communications, 284 (12), 3140-3143 (2011)

[2.14] F. Gaufillet, E. Akmansoy, *Design and experimental evidence of a flat graded-index photonic crystal lens,* Journal of Applied Physics; 114 (8), 083105 (2013)

[2.15] A.O. Pinchuk G.C. Schatz, *Metamaterials with gradient negative index of refraction,* J. Opt. Soc. Am. A Opt Image Sci Vis., 24(10), A39-A44 (2007).

[2.16] Q. Wu, J. M. Gibbons, W. Park, *Graded negative index lens by photonic crystals,* Optics Express**,** 16 (21), 16941-16949 (2008)

[2.17] N. Soodbiswas, S. K. Sarkar, A. Basuray, *Radial GRIN glasses in Li2O-Na2O-Al2O3-TiO2-SiO2 systems,* Journal of Materials Science, 33, 5401-5403 (1998)

[2.18] H. Ottevaere, R. Cox, H. P. Herzig, T. Miyashita, K. Naessens, M. Taghizadeh, R. Volkel, H.J. Woo, H. Thienpont, *Comparing glass and plastic refractive microlenses fabricated with different technologies,* Journal of Optics A: Pure and Applied Optics, 8, S407-S429 (2006)

[2.19] S. Sinzinger & J. Jahns, *Microoptics*, Weinheim, ISBN: 9783527403554, Germany: Wiley-VCH, second ed. (2003)

[2.20] S. Sinzinger, K. Brenner, J. Moisel, T. Spick, M. Testorf, *Astigmatic gradient-index elements for laser-diode collimation and beam shaping*, Applied Optics, 34(29), 6626-6632 (1995)

[2.21] J. Bahr, U. Krackhardt, K. H. Brenner, *Fabrication and testing of planar microlens arrays by ion exchange technique in glass*, Proc. SPIE 4455 (2001)

[2.22] M. Oikawa, K. Iga, T. Sanada, *Distributed-index planar microlens array prepared from deep electromigration*, Electron. Lett., 17(13), 452-454 (1981)

[2.23] W. A. Reed, M. F. Yan, M. J. Schnitzer, *Gradient-index fiber-optic microprobes for minimally invasive in vivo low-coherence interferometry*, Optics Letters, 27(20), 1794-1796 (2002)

[2.24] K. Shingyouchi, S. Konishi, K. Susa, I. Matsuyama, *r-GRIN glass rods prepared by a sol-gel method*, Electron. Lett., 22, 99 (1986).

[2.25] D. R. Uhlmann, D.R. Ulrich, ISBN 0-471-52986-9, *Ultrastructure processing of advanced materials*, John Wiley & Sons (1992)

[2.26] K. Shingyouchi, A. Makishima, M. Tutumi, S. Takenouchi, S. Konishi, *Determination of diffusion coefficient of titanium ion in TiO_2 – SiO_2 wet gel prepared from metal alkoxide during leaching* J. Non-Cryst. Solids, 100, 383 (1988).

[2.27] J. B. Caldwell, Thesis collection, Institute of Optics, University of Rochester (1989)

[2.28] M.T. Gale, *Direct writing of continuous relief micro-optics Micro-optics: Elements, Systems and Applications*, ISBN: 0-7484-0481-3, edited by H.P Herzig, London: Taylor and Francis (1997)

[2.29] C. Ye, R. R. McLeod, *Grin lens and lens array fabrication with diffusion driven photopolymer*, Optics Letters, 33(22), 2575-2577 (2008)

[2.30] L. R. Harriott, R. E. Scott, K. D. Cummings, A. F. Ambrose, *Micromachining of integrated optical structures*, Appl. Phys. Lett., 48, 1704 (1986)

[2.31] E. B. Kley, T. Possner R. Goring, *Realization of micro-optics and integrated optic components by electron-beam lithographic surface profiling and ion exchange in glass*, Int. J. Optoelectron. 8, 513–527 (1993)

3. GEOMETRICAL OPTICS OF THE GRIN ELEMENTS

In this Chapter the modelling methods used to determine the performance of nanostructured micro-optical elements are described. In section 3.1 the theoretical predictions based on the ray optics concerning the size and refractive index distribution of the GRIN lenses [3.1-3.3] are presented. Section 3.2 details the refractive index distribution of GRIN axicons [3.4,3.5]. In section 3.3 a scalar implementation of the Fast Fourier Transform Beam Propagation Method (FFT BPM) [3.6] is used. This method was chosen as it is much less resource consuming and it can handle much larger structures than a fully vectoral algorithm such as the Finite Difference Time Domain (FDTD) method. In the section 3.3 the results of the simulations are shown and compared with the theoretical predictions for the optical elements presented in this thesis.

3.1. Geometrical optics of GRIN lenses

We can assume the distribution of the permittivity n^2 for the lens equals to [3.7 - 3.9].

$$n^2(x,y) = n_0^2[1 - A^2(x^2 + y^2)] \tag{3.1}$$

Where n is the refractive index at a distance $r = \sqrt{x^2 + y^2}$, from the optical axis; n_o is the refractive index on the optical axis, and A is a positive constant which characterizes the steepness of the index gradient 3.7]. X and Y axes are perpendicular to the light propagation direction.

The exact solution of the equation is hard to obtain (3.1), but for practical applications it is sufficient to use the paraxial approximation. In this approximation only these rays which are nearly parallel to the optical axis (Z axis) are considered. This allows to write the paraxial ray equations as [3.7-3.9]

$$\frac{d}{dz}(n\dot{x}) = \frac{\partial n}{\partial x}, \tag{3.2a}$$

$$\frac{d}{dz}(n\dot{y}) = \frac{\partial n}{\partial y}. \tag{3.2b}$$

It also allows to assume that all rays are in the proximity of the optical axis [3.7-3.9]

$$A^2(x^2 + y^2) \ll 1, \tag{3.3}$$

First order approximation of the refractive index distribution can be described as [3.7-3.9]

$$\mathrm{n}(x,y) = n_0\left[1 - \frac{A^2}{2}(x^2 + y^2)\right]. \tag{3.4}$$

For example, let us take a cylindrical optical element with thickness L and radius r suspended in air where the refractive index distribution is described by Eq. (3.4). Now let us use this element as a lens, as shown in the schematic in Fig. 3.1. From this the working distance f_w and effective focal length f of the lens can be calculated using the field ray H_f and Snell's law. The ray trajectory within the lens can be described as [3.7 - 3.9].

$$x_{in}(z) = x_{in}(0)H_f(z) = x_{in}(0)cos(\mathrm{A}z), \tag{3.5}$$

and on the exit plane (V') of the lens [3.7-3.9]

$$x_{in}(L) = x_{in}(0)cos(\mathrm{A}L). \tag{3.6}$$

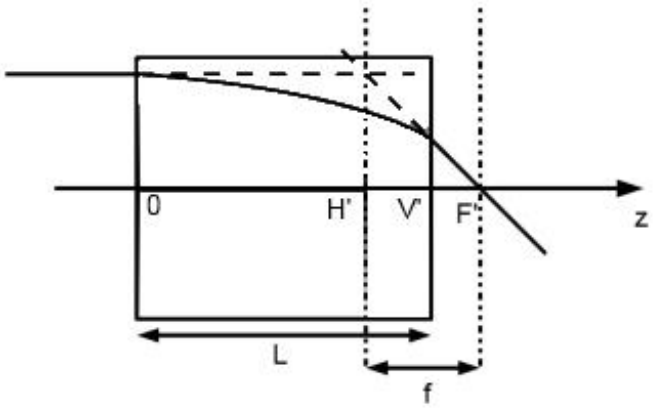

Figure 3.1 - The schematic of the focusing using GRIN lens. $V'F'$ – working distance f_w. f - effective focal length.

Refraction on the exit plane of the lens can be written in relation to Snell's law as [3.7-3.9]

$$\dot{x}_{in}(L)n_0 = \dot{x}_{out}(L), \tag{3.7}$$

where $\dot{x}_{out}$ out describes the ray slope behind the GRIN rod and is equal to [3.7-3.9]

$$\dot{x}_{out}(L) = \frac{-x_{in}(L)}{V'F'} \tag{3.8}$$

Equations (3.5) and (3.7, 3.8) give [3.7 - 3.9]

$$\dot{x}_{in}(L) = -\mathrm{A}sin(\mathrm{A}L)x_{in}(0) \tag{3.9a}$$

$$\dot{x}_{out}(L) = -\mathrm{A}sin(\mathrm{A}L)x_{in}(0)n_0 \tag{3.9b}$$

Which in turn leads to the working distance f_w being described as [3.7-3.9]

$$f_w = V'F' = \frac{-x_{in}(L)}{\dot{x}_{out}(L)} = \frac{1}{\mathrm{A}n_0 tan(\mathrm{A}L)} \tag{3.10}$$

For the lens length $L = L_{qp} = \pi/2\mathrm{A}$ the working distance f_w equals 0. In this situation the focal point is located on the exit plane of the lens and the lens length $L_{qp} = \pi/2\mathrm{A}$ is called the quarter pitch length.

When considering Fig. 3.1 it can be seen that [3.7-3.9]

$$\frac{-x_{in}(0)}{f} = \dot{x}_{out}(L), \tag{3.11}$$

which means that effective focal length *f* equals to [3.7-3.9]

$$f = \frac{x_{in}(0)}{\dot{x}_{out}(L)} = \frac{1}{\mathrm{A}n_0 sin(\mathrm{A}L)}. \tag{3.12}$$

For the lens with a diameter of 20μm, refractive index difference Δn = 0.0331 and maximum refractive index in the centre n_0= 1.5432, the full pitch equals 303.38μm. This means that the half pitch of such a lens equals 151.69μm.

3.2. Geometrical optics of GRIN axicons

Based on the surface profile axicons can be divided into two types: linear axicons and binary axicons [3.10]. Binary axicons are characterised by two levels of refractive index, usually forming concentric alternating rings perpendicular to the optical axis of the axicon. In this thesis the linear axicons are considered. Linear axicons have a conical refractive index change, such as a classical conical prism. While an ordinary lens creates a plane of focus, the result from light propagation through an axicon is a focal line extended along the optical axis [3.4,3.5]. Depending on the design of the axicon, the lengths of the line reach from a couple of millimetres [3.11] up to several kilometres [3.12]. The principle behind this is to refract all rays at approximately the same angle as shown in Fig. 3.4. The focal line is also very narrow through interference effects. This length of the focal line, the depth of focus of the axicon is the main reason of using axicons in this thesis.

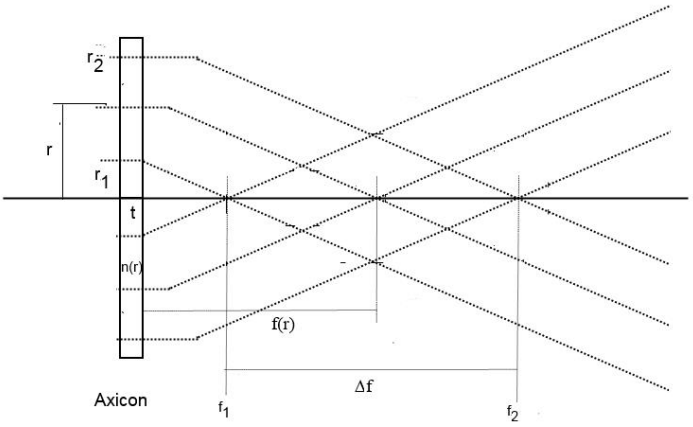

Figure 3.4 - Principle of an axicon. The axicon, creates conical wavefronts which form the narrow focal line. The shape of the axicon can be adjusted to yield different on-axis intensity distributions.

The GRIN axicon lens has a planar surface with a radial gradient index profile. When the incident light is collimated and perpendicular to the GRIN lens, the working distance is proportional to the incident ray height, shown in Fig. 3.4. Thus, the working distance can be expressed as [3.13,3.14].

$$f_w(r) = f_1 + \frac{r - r_1}{r_2 - r_1}\Delta f \ , \tag{3.13}$$

where r is the radial ray position, $r_{1,2}$ is the minimum and maximum ray heights allowed, $f_{1,2}$ is the working distance for the ray height of $r_{1,2}$, Δf is the depth of focus that is equal to f_2 - f_1, and $n(r)$ is the radial gradient index profile.

Assuming the GRIN axicon is a thin lens, there is a negligible beam displacement through the lens [3.13,3.14]. In this case the index profile of the lens can be determined by the optical path argument. The radial position at the end plane of the axicon can be considered as equal to the position at the front plane of the axicon. This can be expressed as $n(0)t = n(r)t + \varphi(r)$, where $\varphi(r)$ is the wavefront displacement at the radial position r and t is the thickness of the lens. The index profile of the lens is [3.13,3.14]

$$n(r) = n_0 - \frac{\varphi(t)}{t}, \tag{3.14}$$

where n_0 is the index of refraction at the centre of the lens. Given that the geometrical ray angle is equal to the slope of the wavefront normal, and assuming the wavefront

displacement φ(r) is much smaller than the working distance $f_w(r)$, the slope of the transmitted wavefront is [3.13,3.14]

$$\tan\theta = -\frac{d\varphi(r)}{dr} = \frac{r}{f(r)}. \tag{3.15}$$

The wavefront displacement $\varphi(r)$ equals [3.13,3.14]

$$\varphi(r) = \int_{r_1}^{r_2} \frac{r}{f(r)}\, dr. \tag{3.16}$$

By replacing $f_w(r)$ with equation (3.13), the wavefront slope can be described by the equation [3.13,3.14]

$$\varphi(r) = \frac{r_2 - r_1}{\Delta f} r - \left(f_1 - \frac{r_1}{r_2 - r_1}\Delta f\right)\left(\frac{r_2 - r_1}{\Delta f}\right)^2 \ln\left[f_1 + \frac{\Delta f}{r_2 - r_1}(r_2 - r_1)\right]_{r_1}^{r_2}. \tag{3.17}$$

Substituting $\varphi(r)$ with equation (4.2) in equation (4.6), the index profile can be simplified to the equation [3.13,3.14]

$$n(r) = n_0 - \frac{r_2}{t(\Delta f)^2}\left[r\Delta f - r_2 f_1 \ln\left(1 + \frac{r\Delta f}{r_2 f_1}\right)\right]. \tag{3.18}$$

In the case when the focus begins at the back surface of the lens the index profile is [3.12,3.13]

$$\lim_{f_1 \to 0} n(r) = n_0 - \frac{r_2}{t\Delta f} r. \tag{3.19}$$

In this case, the index profile has a linear form, similar to a classic conical axicon prism.

3.3. Modelling of the optical elements with Beam Propagation Method

The fast Fourier transform beam propagation method (FFT-BPM) [3.6] is the simulation technique utilised in the presented work. The BPM software utilised in this thesis was developed by Andrew Waddie at Heriot-Watt University. A scalar implementation of FFT-BPM is exploited. The method is based on the numerical solution of the Helmholtz equation. BPM is much less resource consuming, which means that for the same amount of resources used it can handle much larger structures than FDTD. Initial comparison between FTDT and BPM method was performed by J. Nowosielski [3.7], which shows that BPM is sufficient to accurately simulate nanostructures. BPM is used, for a comparison of a performance of a microlens with a quantised refractive index profile to the performance of the corresponding unquantised microlens.

3.3.1. Beam Propagation Method

The BPM is derived from the scalar Helmholtz equation [3.6, 3.7].

$$\frac{\partial^2\varphi}{\partial x^2}+\frac{\partial^2\varphi}{\partial y^2}+\frac{\partial^2\varphi}{\partial z^2}+k_0^2n^2\varphi=0 \tag{3.20}$$

where k_0 is the wavenumber in vacuum and $n(x,y)$ is the refractive index distribution. As incident light is considered to be a monochromatic wave, a field component can be written as $\varphi(x,y,z)exp(i\omega t)$.

Assuming incident light propagation in the free space where $n(x,y,z) = n_0$, an approach based on the angular spectrum of plane waves (ASPW) can be utilised. The angular spectrum approach is a mathematical technique to describe optical fields. The complex wave fields are represented as a superposition of plane waves and evanescent waves, which are solutions of Maxwell's equations. ASPW utilises a 2D spatial Fourier transform in order to decompose wavefields within a single plane into its plane wave components. Each plane wave is then propagated through the Fourier domain to a destination plane. At the destination plane those plane waves are then reconstructed using an inverse spatial Fourier transform [3.15].

By using Fourier integral form, the solution to the equation (3.20) can be written as [3.7]

$$\varphi(x,y,z)=\iint_{-\infty}^{\infty}\Psi(v_x,v_y,z)exp\left[i2\pi\left(v_xx+v_yy\right)\right]dv_xdv_y\ . \tag{3.21}$$

$\Psi(v_x,v_y,z)exp\left[i2\pi\left(v_x+v_yy\right)\right]$ describes a plane wave, which is characterised by the spatial frequencies v_x and v_y. By substituting of equation (3.21) into equation (3.20) one can achieve the equation for $\Psi(v_x,v_y,z)$ [3.7]

$$\frac{\partial^2\Psi}{\partial x^2}+\beta^2\Psi(v_x,v_y,z)=0\ , \tag{3.22}$$

where [3.7]

$$\beta^2=k_0^2n_0^2-4\pi^2\left(v_x^2+v_y^2\right)\ . \tag{3.23}$$

Equation (3.23) can be solved as [3.7]

$$\Psi(v_x,v_y,z)=\Psi(v_x,v_y,0)exp[-i\beta(z-z_0)]\ . \tag{3.24}$$

If the field distribution (x,y,z_0) is known at $z = z_0$, then by using Fourier transform it is possible to calculate the spectrum $\Psi(v_x,v_y,z_0)$ [3.7].

$$\Psi(v_x,v_y,z_0)=F\left(\varphi(v_x,v_y,z_0)\right)=\iint_{-\infty}^{\infty}\varphi(v_x,v_y,z)exp\left[-i2\pi\left(v_xx+v_yy\right)\right]dv_xdv_y\ . \tag{3.25}$$

From the equation (3.24) it is possible to calculate $\Psi(v_x,v_y,z)$ at any z. Then an inverse Fourier transform helps to obtain $\varphi(x,y,z)$. This is expressed by the equation [3.7].

$$\varphi(x,y,z) = F^{-1}\{F\big(\varphi(x,y,z_0)\big)exp[-i\beta(z-z_0)]\}\,, \tag{3.26}$$

where F is the Fourier transform and F^{-1} is the inverse Fourier transform.

Now let us turn to the case in which refractive index distribution is described by *n(x, y).* Complex field $\varphi(x,y,z)$ can be described as [3.6,3.7]:

$$\varphi(x,y,z) = \phi(x,y,z)exp(-ik_0\bar{n}z) \tag{3.27}$$

where $\bar{n}$ equals to the averaged refractive index in the cross-section of the simulation space. By substituting equation (3.27) into scalar Helmholtz equation (3.20) one can obtain equation [3.6,3.7]

$$\nabla^2\phi - 2ik_0\acute{n}\frac{\partial\phi}{\partial z} + k_0^2(n^2-\bar{n}^2)\phi = 0\,, \tag{3.28}$$

where [3.6,3.7]

$$\nabla^2 = \frac{\partial^2}{\partial x^2} + \frac{\partial^2}{\partial y^2} + \frac{\partial^2}{\partial z^2}\,. \tag{3.29}$$

This can be further simplified if one assumes a low contrast structure. Then one can write $(n^2-\bar{n}^2) \approx 2\bar{n}(n-\bar{n})$. This allows to write equation (3.29) as [3.6,3.7]

$$\frac{\partial\phi}{\partial z} = -i\frac{1}{2k_0\acute{n}}\nabla^2\phi - ik_0(n-\acute{n})\phi\,. \tag{3.30}$$

The first term of the Eq. (3.30) describes a free space propagation in the medium with refractive index $\bar{n}$. , which can be described using the operator representation as [3.6,3.7]

$$\frac{\partial\phi}{\partial z} = (\mathrm{A}+\mathrm{B})\phi\,, \tag{3.31}$$

where [3.6,3.7]

$$\mathrm{A} = -i\frac{1}{2k_0\acute{n}}\nabla^2 \tag{3.32a}$$

$$\mathrm{B} = -ik_0(n-\bar{n}) \tag{3.33b}$$

By using formal integration of the equation (3.31) one can write [3.6,3.7]

$$\phi(x,y,z+h) = exp(\mathrm{A}+\mathrm{B})\phi(x,y,z) \tag{3.34}$$

Using Baker-Hausdorff theorem [3.8] which states that

$$exp(\alpha A+\beta B) = exp(\alpha A)\,exp(\beta B)\,exp(\frac{\alpha\beta}{2}C) \tag{3.35}$$

and assuming that h is small it is possible to approximate [3.6,3.7]

$$exp(h\mathrm{A}+h\mathrm{B}) \approx exp(h\mathrm{A})exp(h\mathrm{B})\,. \tag{3.36}$$

This means that one can express equation (3.34) as [3.6, 3.7]

$$\phi(x,y,z+h) = exp(h\mathrm{A})exp(h\mathrm{B})\phi(x,y,z)\ . \tag{3.37}$$

The term $exp(h\mathrm{A})$ describes the free space propagation. The term $exp(h\mathrm{B})$ can be described as a phase correction term and is related to the medium inhomogeneity. If for a particular *z* a $\phi(x,y,z)$ distribution is known, then to calculate $\phi(x,y,z+h)$ for small *h* one can propagate wave in the free space. To get the correct answer for the propagation in inhomogeneous medium phase correction term has to be then applied. This procedure can be expressed using complex field $\psi(x,y,z)$ [3.6, 3.7].

The free space propagation by the small distance *h* in the homogenous medium is given by equation (3.26) and equation (3.23) [3.6, 3.7]

$$\psi_{fs}(x,y,z+h) = F^{-1}\{F\big(\varphi(x,y,z)\big)exp(-i\beta h)\} \tag{3.38}$$

The phase correction is given by [3.6, 3.7]

$$\psi_{fs}(x,y,z+h) = exp(h\mathrm{B})\varphi_{fs}(x,y,z+h) = exp[-ik_0(n-\bar{n})h]\varphi_{fs}(x,y,z+h) \tag{3.39}$$

This procedure can be used for calculating field $\psi(x,y,z)$ in the planes perpendicular to *Z* axis starting from the known initial field for z = z_0. In the BPM simulations Fourier transforms are realised by the discrete Fourier transform (DFT) using fast Fourier transform (FFT) algorithm. Minimum lateral resolution of the simulation is determined by the sampling theorem [3.15], which states that lateral steps Δx and Δy satisfy the condition [3.6,3.7]:

$$\Delta x \leq \frac{\lambda_0}{2n_{max}} \tag{3.40}$$

where n_{max} describes a maximum refractive index in the system and λ_o is the vacuum wavelength. Distance *h* has to satisfy the condition [3.6, 3.7]:

$$h = \frac{\lambda_o}{2\pi|n-\acute{n}|}\ . \tag{3.41}$$

3.4. Propagation through GRIN lens

Using the FFT BPM described in the previous section, an ideal refractive index distribution lens was modelled. The schematic of the simulation is shown of Fig.3.2 while the refractive index distribution of the lens is shown on Fig.3.3.

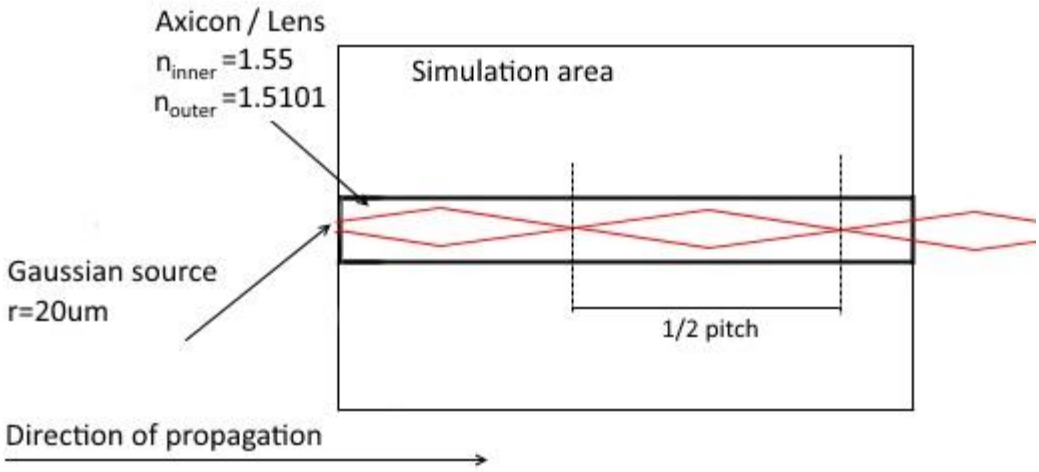

Figure 3.2 - Simulation schematic. The simulation area is the area in which FFT-BPM was used to calculate field propagation, with all the parameters in front of the simulation area presented as boundary conditions for the simulation.

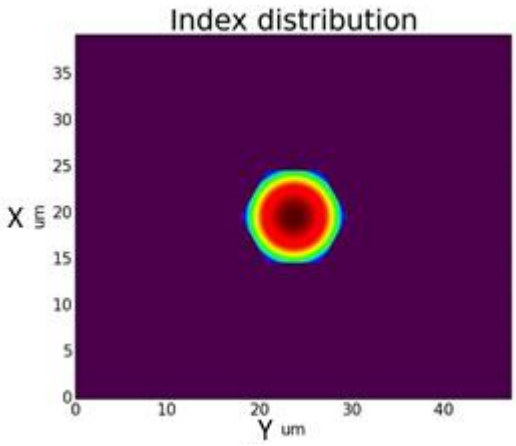

Figure 3.3 - Refractive index distribution of the ideal lens.

The lens used in the simulation has the same parameters as the one describe at the end of the section 3.1. The diameter of the lens equals to 20μm, refractive index difference Δn = 0.0331 and maximum refractive index in the centre n_0= 1.5432. Light propagation through this lens is shown on fig 3.4. Both focal planes are shown on fig. 3.5, which shows that the field amplitude at the second focal plane is equal to 76% of the amplitude at the first focal plane.

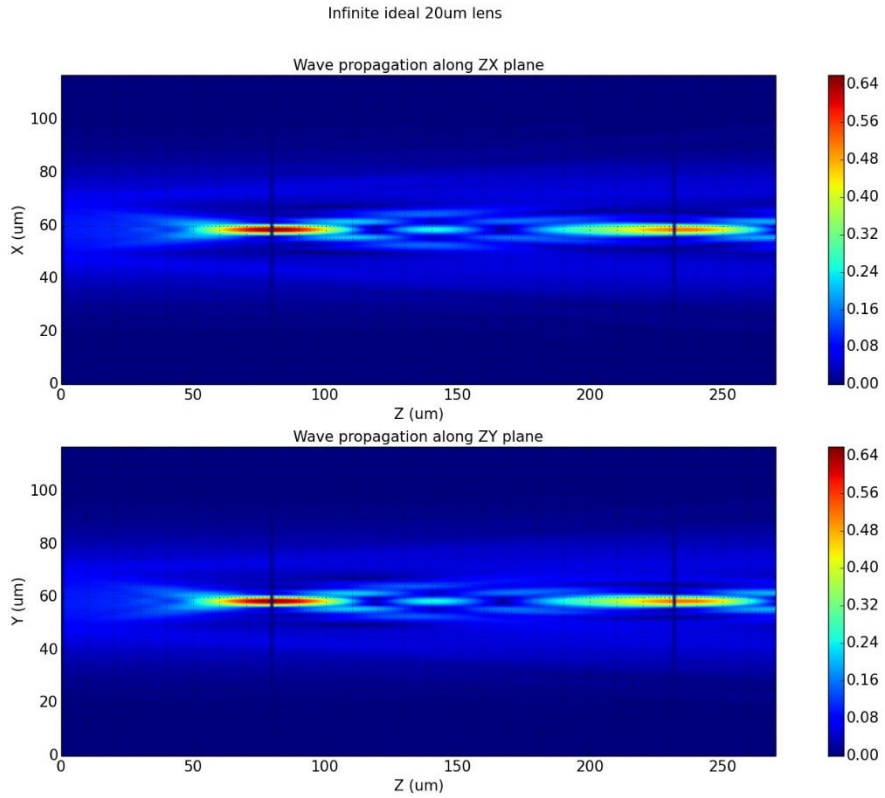

Figure 3.4 - Light propagation through infinite ideal lens with diameter of 20μm. Two closest focal points are shown. Blue vertical lines show positions of the highest amplitudes for both points.

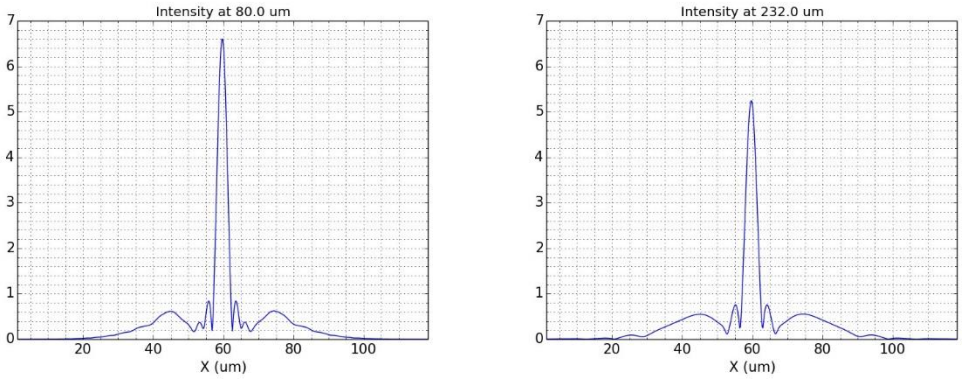

(a) (b)

Figure 3.5 - First (a) and second (b) focal point along the light propagation through the infinite ideal lens. Both peaks show field amplitude as fractions of the initial source amplitude. Amplitude of the second focal point equals to 76% of the first.

The half pitch of the lens is equal to 152μm. Given that the simulation step is 1μm this is exactly the same as the theoretical predictions from section 3.1.

3.5. Conclusions

Comparison of the theoretical predictions and computer simulations show that for ideal structures the FFT BPM used in this thesis accurately represents the operation of the optical elements that are main theme of this thesis. For the lens with diameter of 20μm, refractive index difference Δn = 0.0331 and maximum refractive index in the centre n_0= 1.5432 the pitch of such a lens equals 303.38μm. This means that quarter pitch of such a lens equals to 75.84μm.

	Geometrical optics results	Simulation results
Quarter pitch length	75.84μm	76μm

Table 3.1 - Comparison of theoretical and simulation lens parameters.

3.6. References

[3.1] E. Centeno, D. Cassagne, *Graded photonic crystals*, Opt. Lett., 30, 2278-2280 (2005)

[3.2] H. Kurt, E. Colak, O. Cakmak, H. Caglayan, E. Ozbay, *The focusing effect of graded index photonic crystals*, Applied Physics Letters, 93(17), 171108 (2008)

[3.3] C. Tan, T. Niemi, C. Peng, M. Pessa, *Focusing effect of a graded index photonic crystal lens*, Optics Communications, 284(12), 3140-3143 (2011)

[3.4] F. Aieta, P. Genevet, M. A. Kats, N. Yu, R. Blanchard, Z. Gaburro, F. Capasso, *Aberration-Free Ultrathin Flat Lenses and Axicons at Telecom Wavelengths Based on Plasmonic Metasurfaces*, Nano Lett, 12(9), 4932–4936, (2012)

[3.5] A. Burvall, *Axicon imaging by scalar diffraction theory*, Thesis collection, Royal Institute of Technology, Stockholm (2004)

[3.6] K. Okamoto, *Fundamentals of Optical Waveguides*, ISBN: 9-7801-2525-0962, San Diego: Academic Press (2000)

[3.7] J. M. Nowosielski, *Nanostructured Birefringent and Gradient-Index Micro-Optical Elements*, Thesis collection, Heriot Watt University (2014)

[3.8] D. Marcuse, *Light Transmission Optics*, ISBN: 0-8946-4305-3, New York: Van Nostrand Reinhold Company (1972)

[3.9] B. A. E. Saleh, M.C. Teich, *Fundamentals of Photonics*, ISBN: 978-0-471-35832-9, John Wiley and Sons (1991)

[3.10] V. V. Kotlyar, S. S. Stafeev, L. O'Faolain, V. A. Soifer. *Tight focusing with a binary microaxicon*, Optics Letters, 36(16), 3100-3102, (2011)

[3.11] V. E. Peet, R. V. Tsubin, *Third-harmonic generation and multiphoton ionization in Bessel beams*, Physical Review A, 56(2), (1997)

[3.12] T. Aruga, *Generation of long-range nondiffracting narrow light beams*, Applied Optics, 6(16), 3762-3768 (1997)

[3.13] C. Ye, *Three-dimensional Gradient Index Optics Fabricated in Diffusive Photopolymers*, Thesis collection, University of Colorado (2012)

[3.14] D. J. Fischer, C. J. Harkrider, D. T. Moore, *Design and manufacture of a gradient-index axicon*, Applied Optics, 39(16), 2687-2694, (2000)

[3.15] J. W. Goodman, *Introduction to Fourier Optics*, ISBN: 0-9747-0772-4, MaGraw-Hill, 2nd ed. (1996)

4. PERFORMANCE OF THE GRIN ELEMENTS COMBINED WITH THE OPTICAL FIBRE

In this Chapter numerical verification of light propagation in the system composed of the optical elements attached to the optical fibre was performed. As a light source, a single mode fibre with core diameter 4.6μm propagating 1550nm wavelength was used. Section 4.1 shows numerical tests performed for various lengths of a lens with continuous refractive index distribution. The simulations are for 20μm, 40μm and 60μm lens length, which represents 0.066, 0.13 and 0.20 of the pitch of the selected lens. Section 4.2 the same simulations are performed for ideal axicons, with lengths 20μm, 40μm and 60μm.

4.1. Performance of the GRIN lens

According to the theory and simulations from Chapter 2 the quarter pitch length of the lens with ideal refractive index distribution is equal to 76μm. In this thesis the optical elements are to be attached to the optical fibres. The first simulation was for the infinite lens attached to the optical fibre. The area of the simulation consisted of a Gaussian source of 4.6μm width introducing light into a 400μm length of a single mode fibre. The core of the fibre has 4.6μm in diameter with refractive index 1.452. The refractive index of the cladding is equal to 1.446. Those parameters closely resemble the SM600 fibre from Thorlabs, as this was the first fibre considered for this thesis. This fibre is an example of the small core diameter fibre, almost half the core diameter of SMF28 fibre (4.6μm compared to 9.6μm). The SM600 fibre has a small mode field and is closer to a point source then SMF28 fibre. This should alleviate the problems posed by the small aperture of the nanostructured lens. Also the SM600 fibre has to be positioned with greater precision for the light to illuminate the centre of the lens, showing the feasibility of our method with wider range of fibres with various core diameters.

The on-axis refractive index of the lens equals $n_0 = 1.5432$. The diameter of the microlens is 20μm leading to a minimum refractive index n_{min} of 1.5101. Those are typical parameters of the GRIN lens fabricated from F2/NC21 glass pair, described in detail in Chapter 5.1 (Fig.4.1)

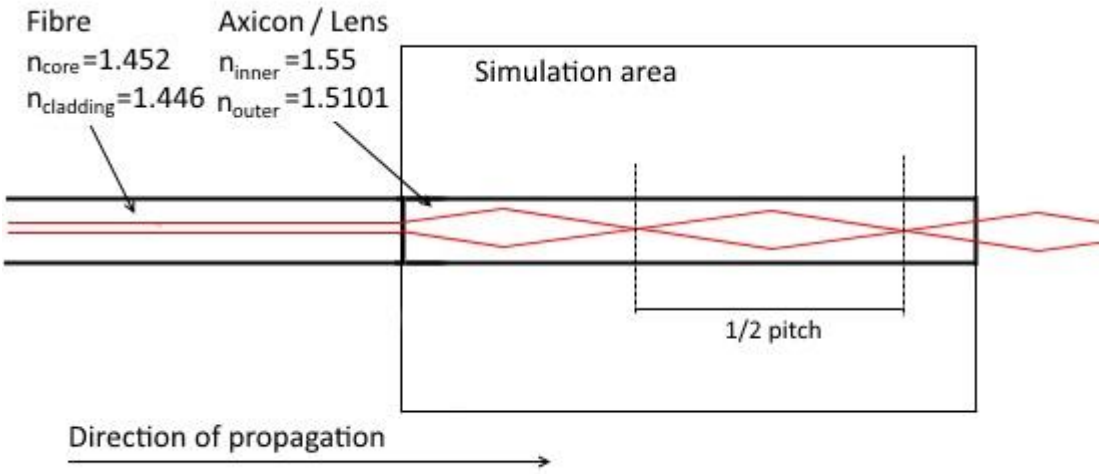

Figure 4.1 - Schematic of the area of the FFT BPM simulation. The simulation area is the area in which FFT-BPM was used to calculate field propagation, with all the parameters in front of the simulation area presented as boundary conditions for the simulation.

As explained in Chapter 2, half of the pitch of the lens equals 151.69μm. The half pitch of a lens should be clearly visible on a field propagation simulation as a distance between closest focal planes inside an infinite lens. As can be seen on Fig 4.2 the half pitch of the simulated ideal lens is equal to 152μm. In fig. 4.3 light intensity at first and second focal plane (separated by ½ of lens pitch) can be seen.

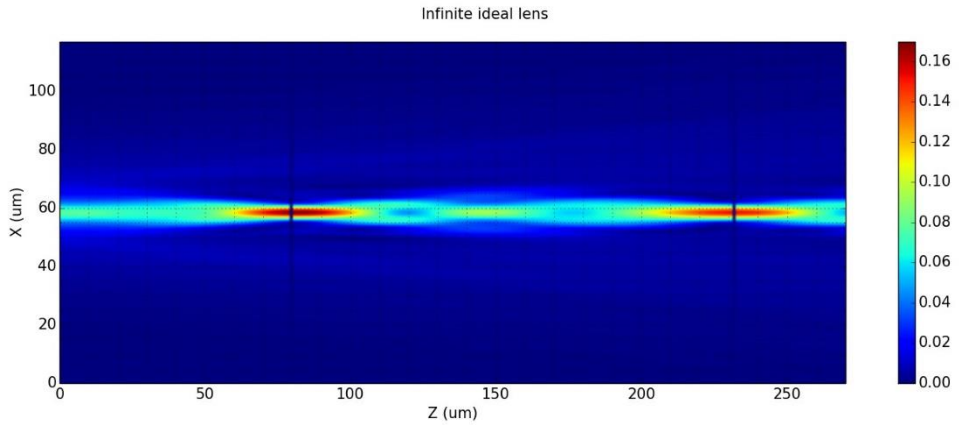

Figure 4.2 - Propagation of the light amplitude through infinite ideal lens. Two closest focal points are shown. Lens is directly attached to the fibre. Blue vertical lines show positions of the highest amplitudes for both points.

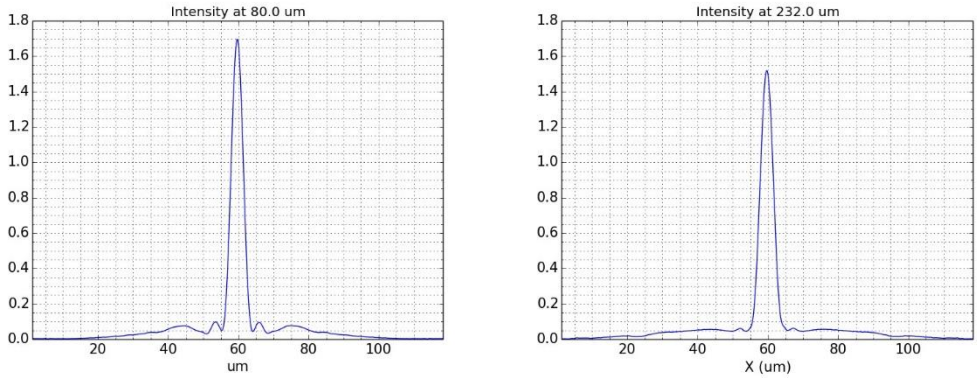

(a) (b)

Figure 4.3 – Intensity at first (a) and second (b) focal plane along the light propagation through the infinite ideal lens. Both peaks show light intensity as fractions of the intensity at the fibre end plane. Intensity of the second focal point equals to 89% of the first.

This is in line with the theoretical results from Chapter 2, the half micron difference stems from the fact that simulation was done with a 1μm step. This size of step was chosen to speed the simulation process, but is still within the limit imposed by the sampling theorem [4.1] (as explained in section 3.3.2). The simulations with the smaller steps (up to 0.1μm) were performed. All those simulations were run for the systems discussed in the thesis by J. Nowosielski [4.2], showing the same results, confirming the validity of the method. Tests performed by J. Nowosielski confirm that this resolution is adequate for a structure that has subwavelength structures perpendicular to the light propagation direction but is continuous along the light propagation direction.

After confirming that the simulations are consistent with the theoretical predictions for the lens with fibre source, a series of simulations showing light propagation after lenses with various lengths with the same light source (Fig.4.4) were performed.

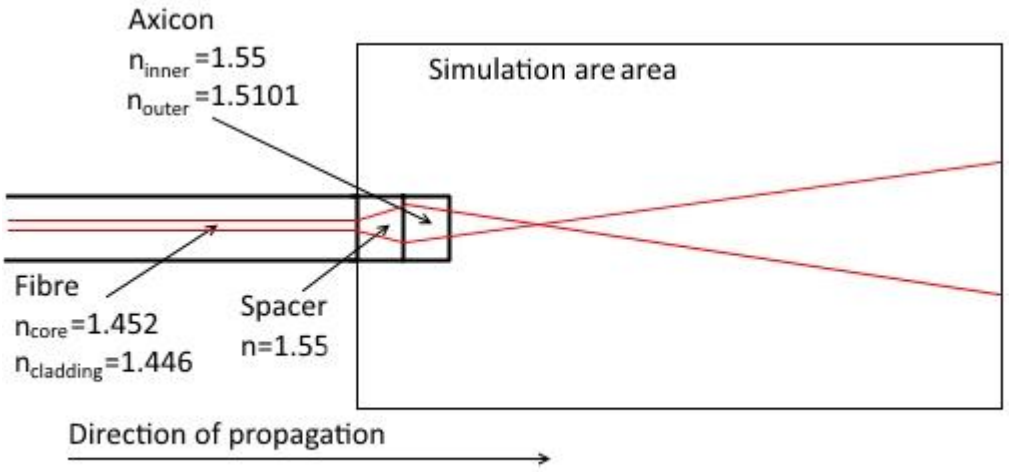

Figure 4.4 - Simulation schematic. The simulation area is the area in which FFT-BPM was used to calculate field propagation, with all the parameters in front of the simulation area presented as boundary conditions for the simulation.

The following set of figures shows the propagation of the light through lenses attached directly to the fibre with lengths 20μm (fig. 4.5, 4.6), 40μm, (4.7, 4.8), 60μm (Fig.4.9, 4.10) and 76μm (Fig. 4.11, 4.12)

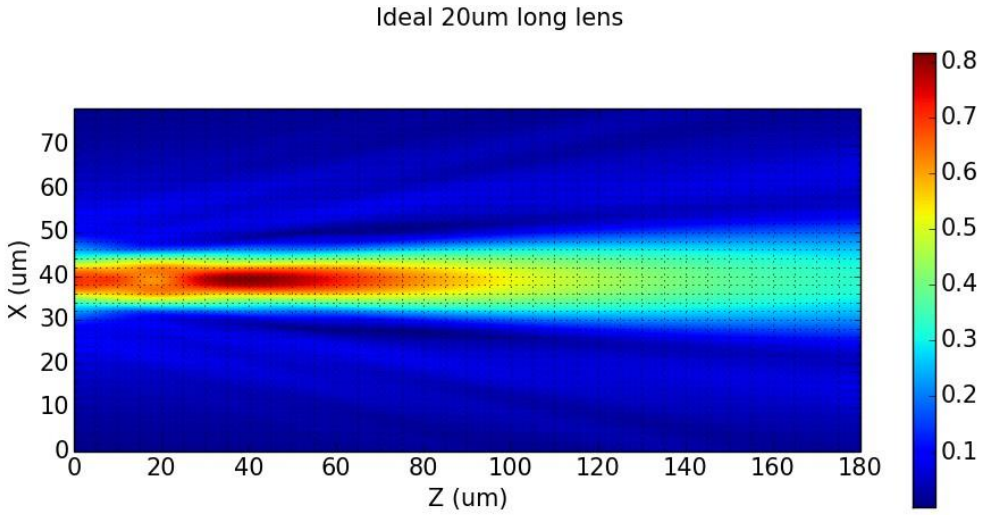

Figure 4.5 - Propagation of the light amplitude after 20μm long ideal lens. The lens is 20μm in diameter and is directly attached to the fibre. Figure shows light propagation after exit plane of the lens (0μm).

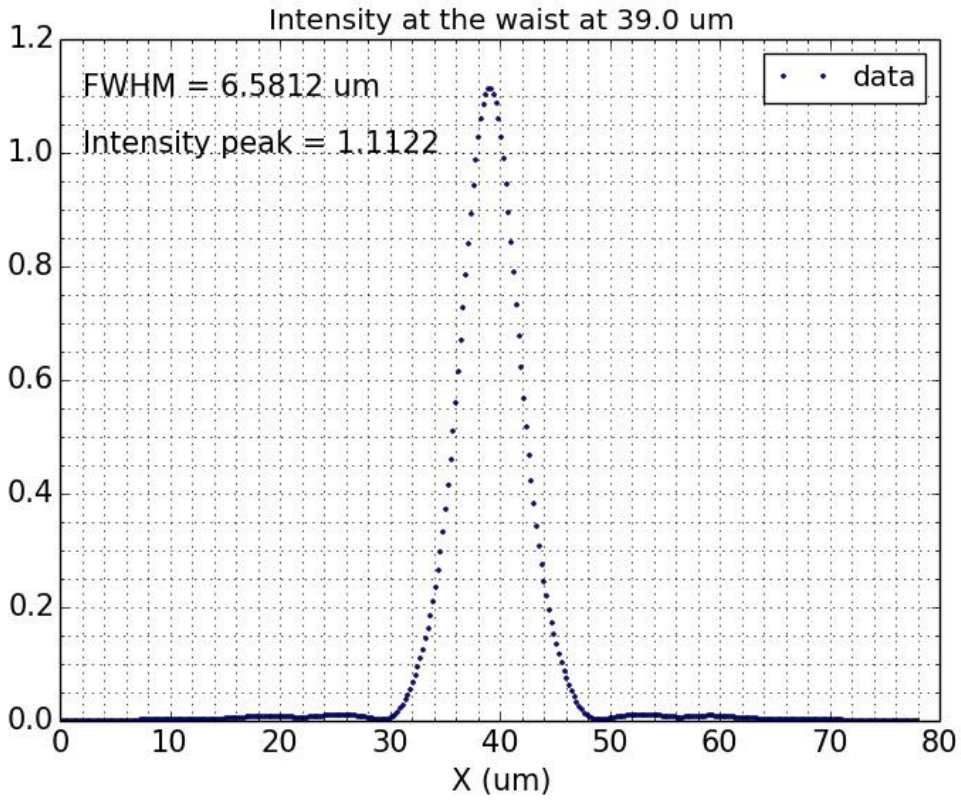

Figure 4.6 - Focal plane along the propagation of the light through the 20μm long ideal lens. The peak shows intensity as fraction of the intensity at the fibre end plane.

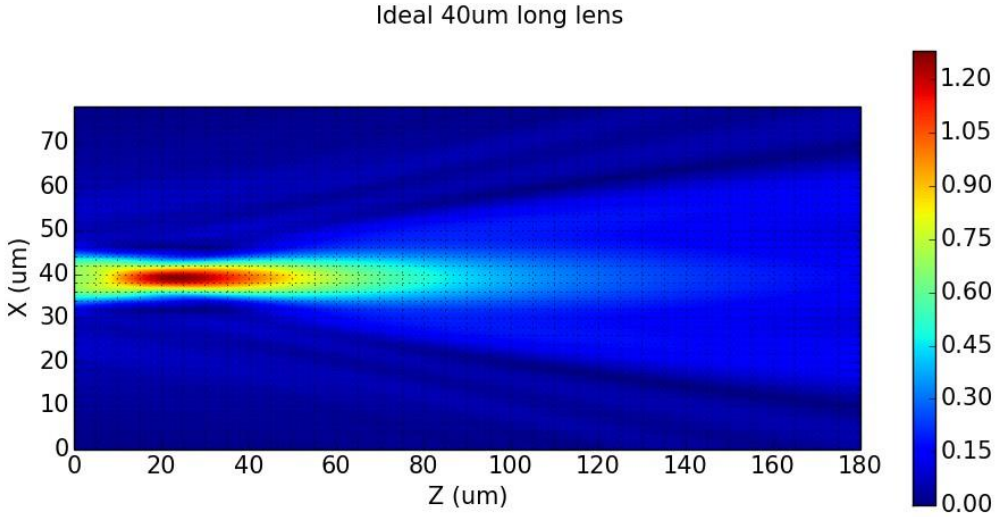

Figure 4.7 - Propagation of the light amplitude after 40μm long ideal lens. The lens is 20μm in diameter and is directly attached to the fibre. Figure shows light propagation after exit plane of the lens (0μm).

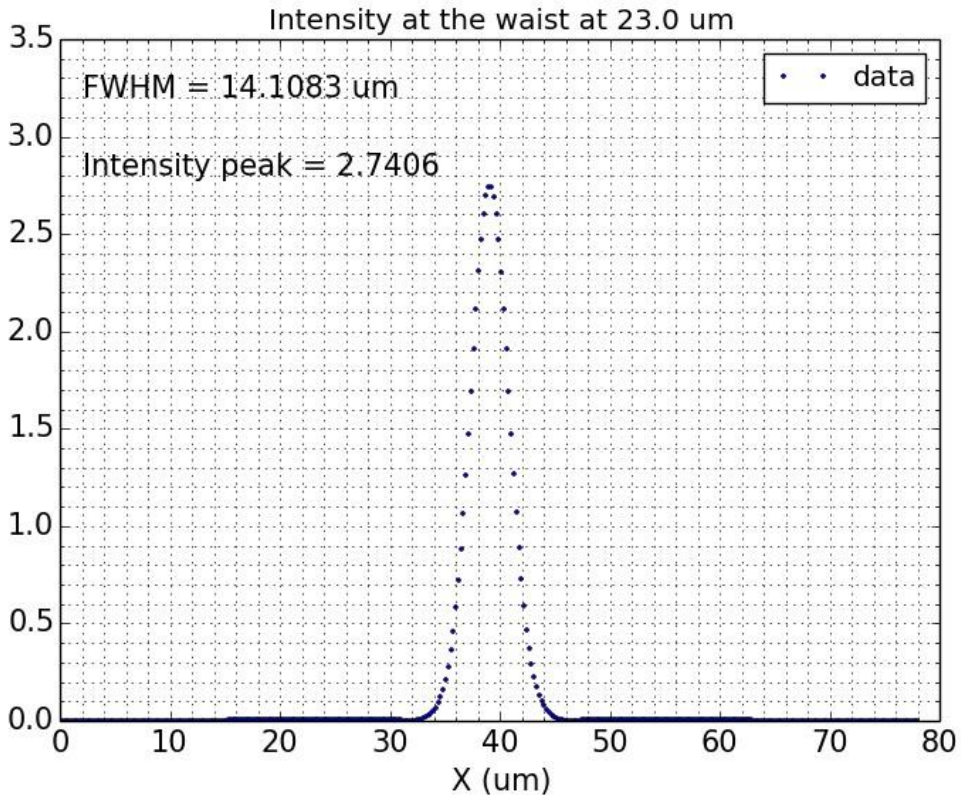

Figure 4.8 - Focal plane along the propagation of the light through the 40μm long ideal lens. The peak shows intensity as fraction of the intensity at the fibre end plane.

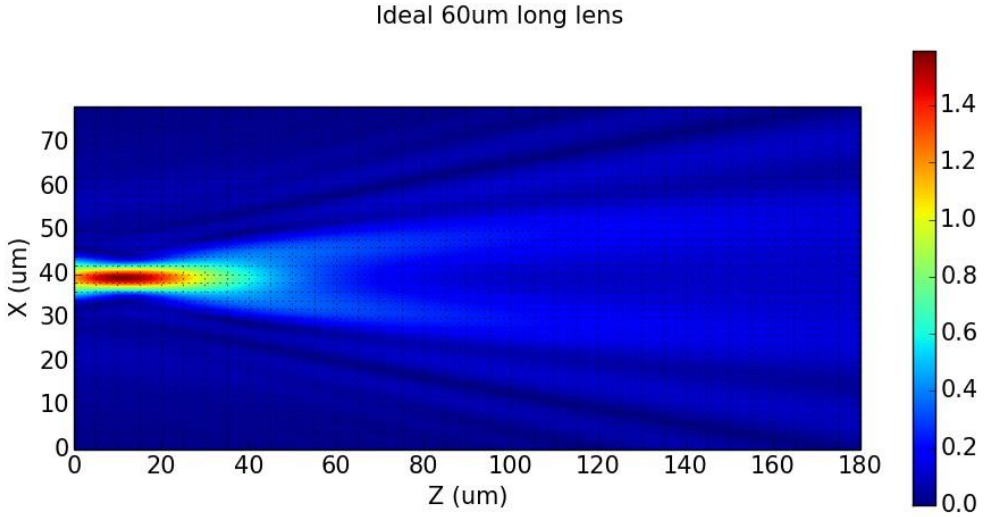

Figure 4.9 - Propagation of the light amplitude after 60μm long ideal lens. The lens is 20μm in diameter and is directly attached to the fibre. Figure shows light propagation after exit plane of the lens (0μm).

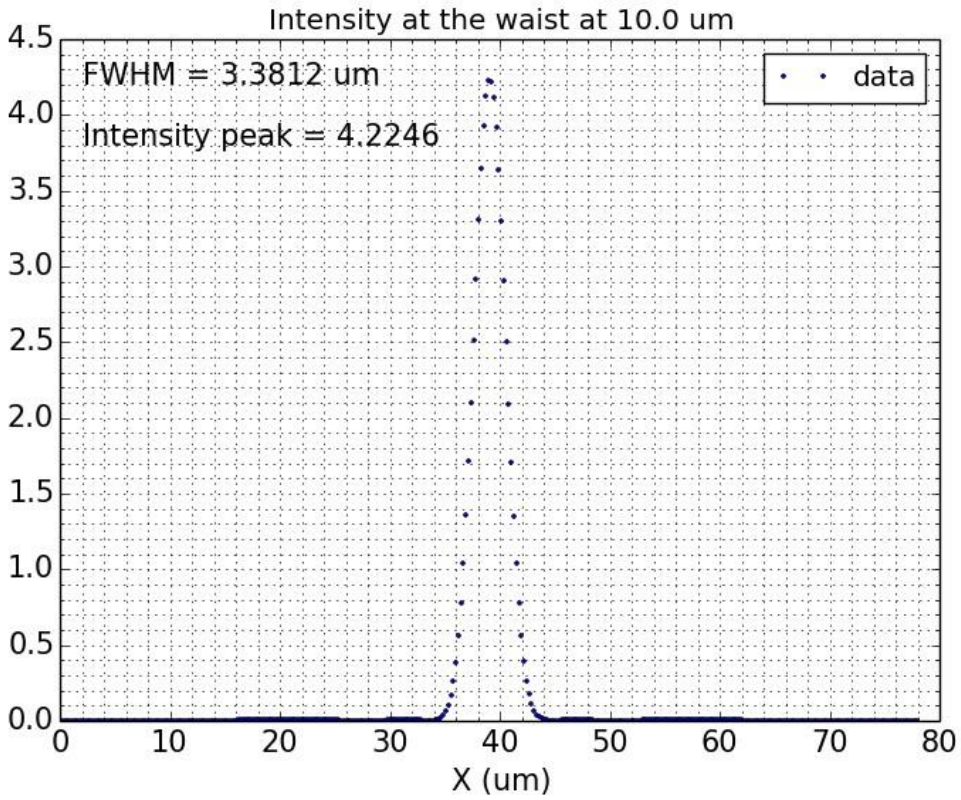

Figure 4.10 - Focal plane along the propagation of the light through the 60μm long ideal lens. The peak shows intensity as fraction of the intensity at the fibre end plane.

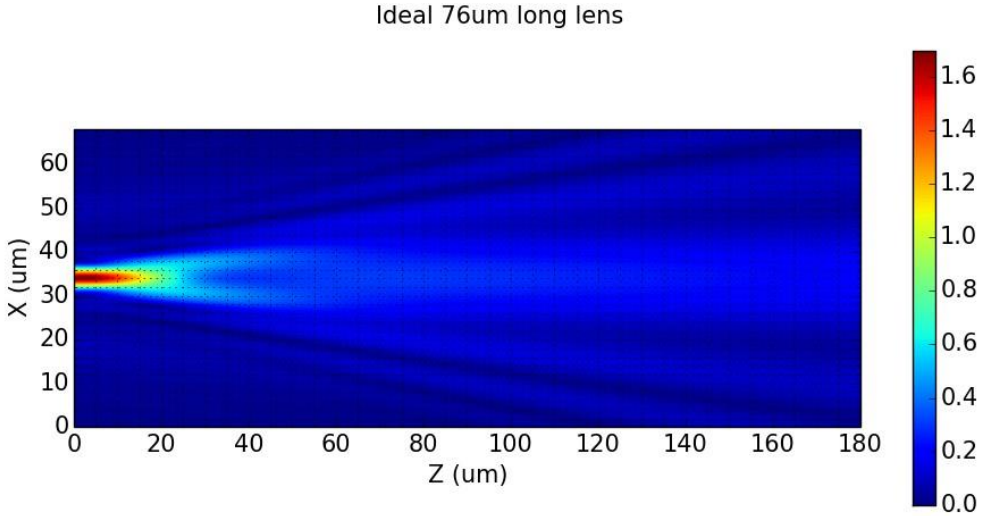

Figure 4.11 - Propagation of the light amplitude after 76μm long ideal lens. The lens is 20μm in diameter and is directly attached to the fibre. Figure shows light propagation after exit plane of the lens (0μm).

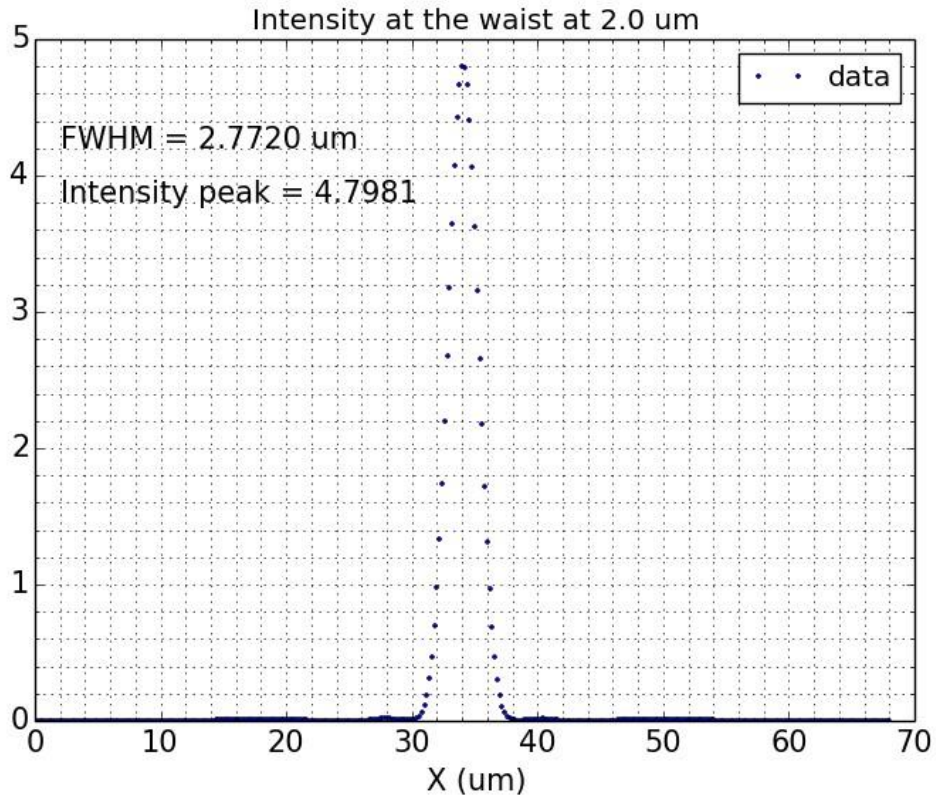

Figure 4.12 - Focal plane along the propagation of the light through the 76μm long ideal lens. The peak shows intensity as fraction of the intensity at the fibre end plane.

As expected, the closer in length the lens is to the quarter pitch length, the intensity of propagating light in focal plane is increasing. For the 20μm lens it equals 2.7 of the incident light, while for the 76μm lens it equals 4.79 of the intensity at the end of the fibre. At the same time focal plane is nearing the exit facet of the lens. For the lens 76μm long (which is close to quarter pitch length of the lens) focal plane is positioned 2μm from exit plane of the lens.

4.2. Performance of the GRIN axicon

The same simulations as shown in figure 4.4 were performed for the ideal axicons using the same experimental setup as for the lenses. The following set of figures shows the propagation of the light through axicons attached directly to the fibre with lengths 20μm (Fig. 4.11, 4.12), 40μm, (Fig. 4.13, 4.14) and 60μm (Fig. 4.15, 4.16)

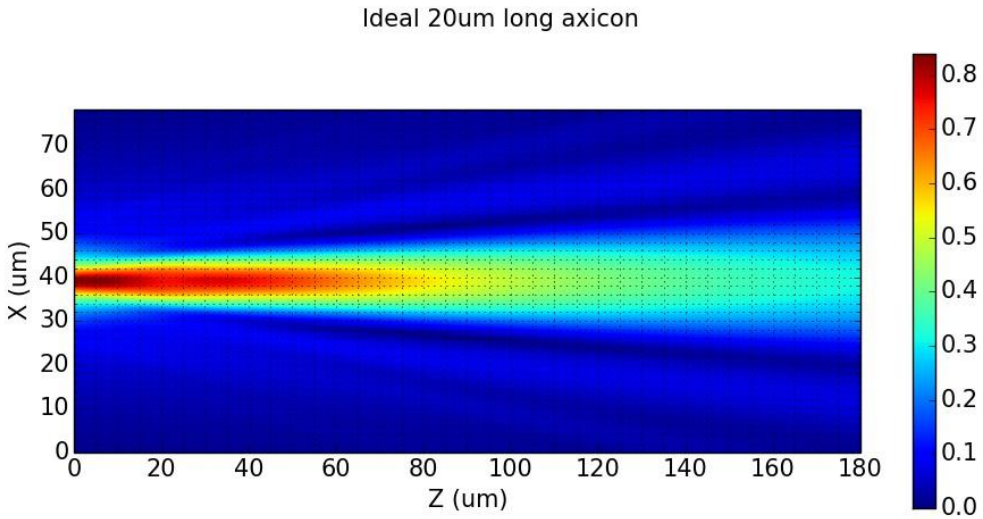

Figure 4.11 - Propagation of the light amplitude after 20µm long ideal axicon. The axicon is 20µm in diameter and is directly attached to the fibre. Figure shows light propagation after exit plane of the axicon (0µm).

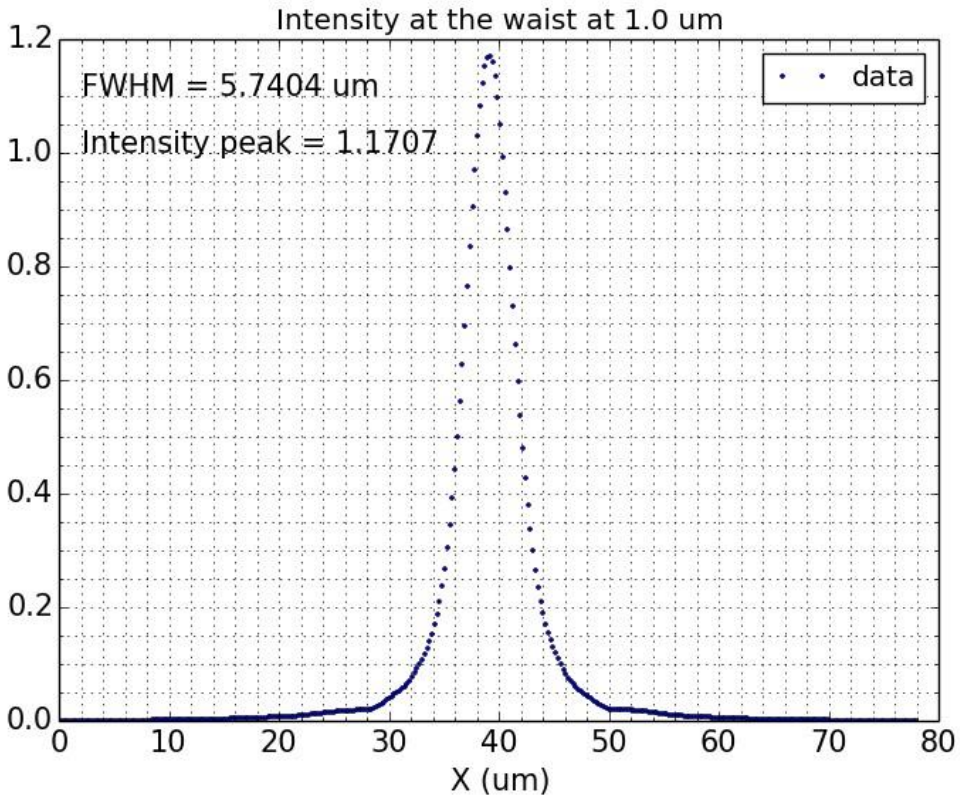

Figure 4.12 - Focal plane along the propagation of the light through the 20µm long ideal axicon. The peak shows intensity as fraction of the intensity at the fibre end plane.

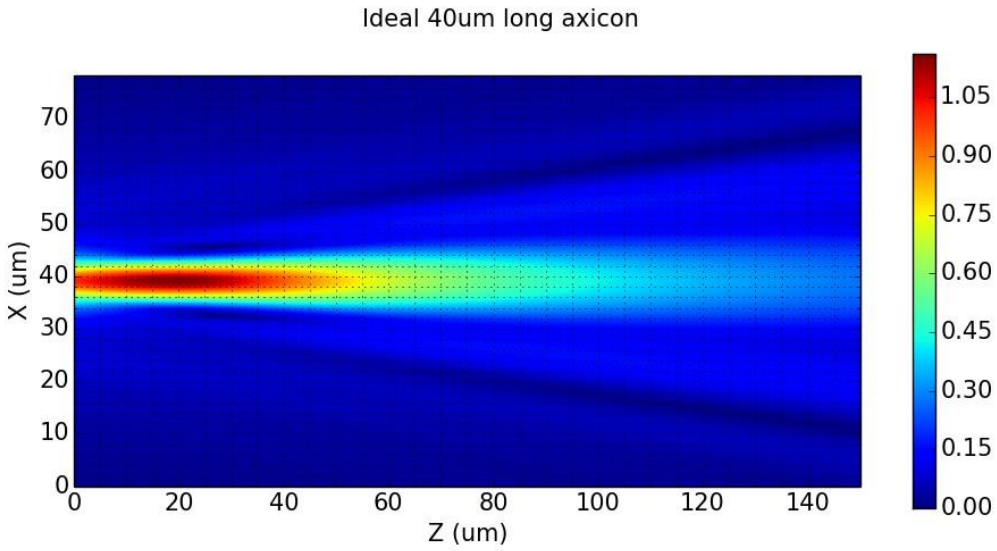

Figure 4.13 - Propagation of the light amplitude after 40μm long ideal axicon. The axicon is 20μm in diameter and is directly attached to the fibre. Figure shows light propagation after exit plane of the axicon (0μm).

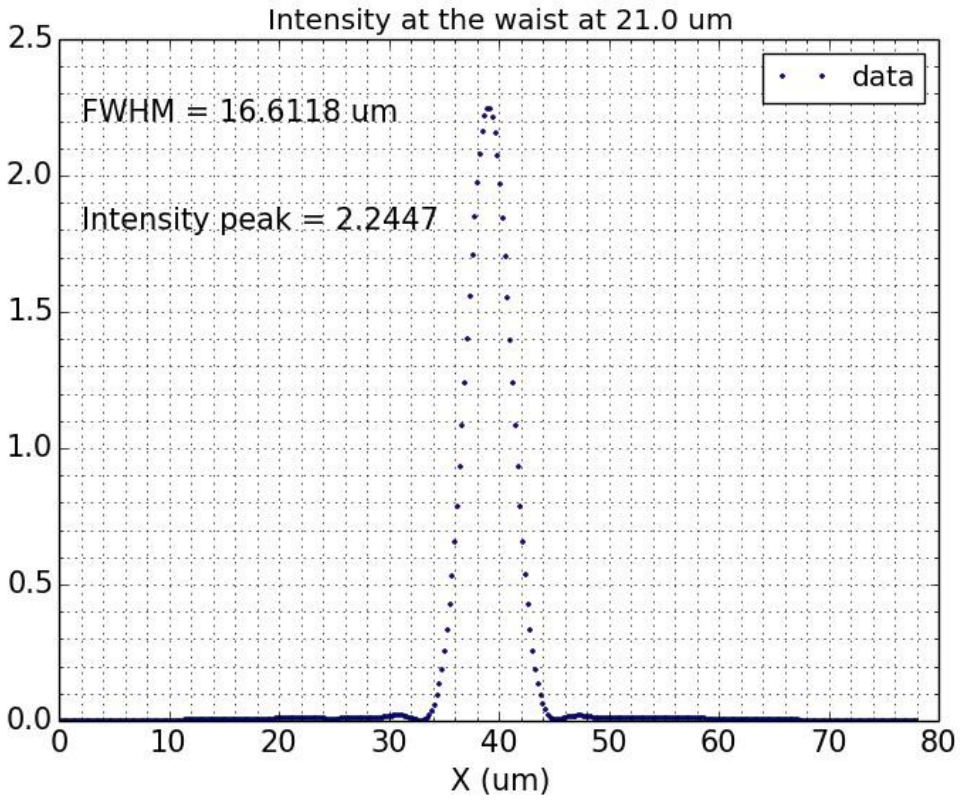

Figure 4.14 - Focal plane along the propagation of the light through the 40μm long ideal axicon. The peak shows intensity as fraction of the intensity at the fibre end plane.

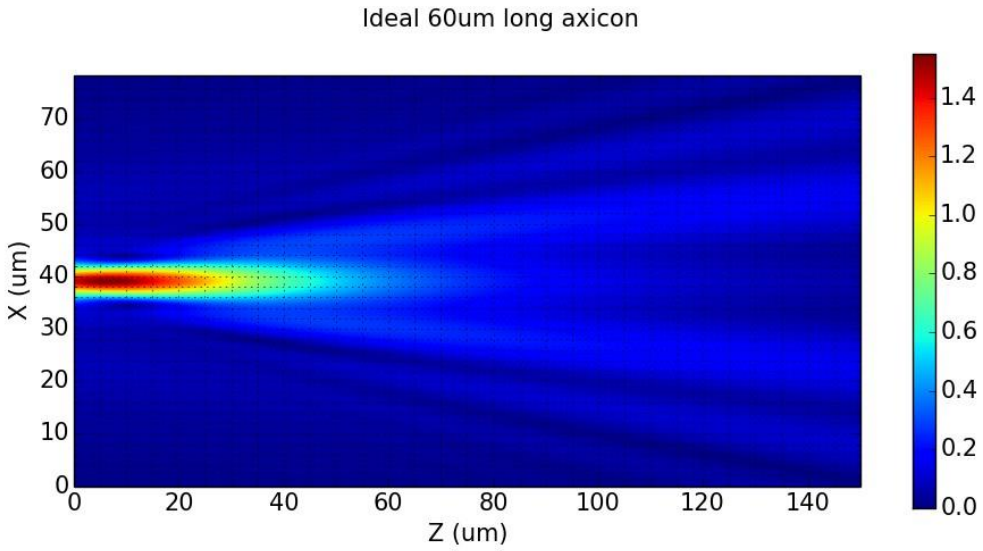

Figure 4.15 - Propagation of the light amplitude after 60μm long ideal axicon. The axicon is 20μm in diameter and is directly attached to the fibre. Figure shows light propagation after exit plane of the axicon (0μm).

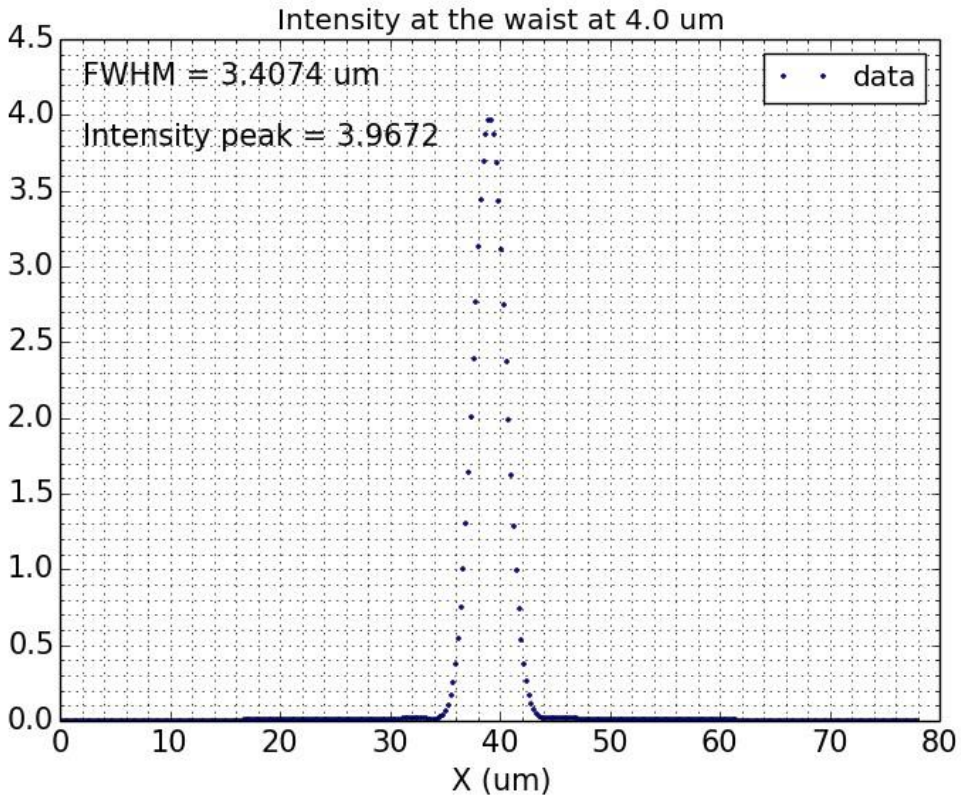

Figure 4.16 - Focal plane along the propagation of the light through the 60μm long ideal axicon. The peak shows intensity as fraction of the intensity at the fibre end plane.

As expected with the increase of the axicon length the intensity of propagating light in focal plane is increasing. For the 20μm axicon it equals 1.17 of the incident light, while for the 60μm axicon it equals 3.96.

As is explained in Chapter 2.1, the reason for using axicons in this thesis was the possibility of obtaining a longer depth of focus compared to lenses. Figure 4.17 shows a comparison of the light intensity along the optical axis for nanostructured lenses and axicons. All graphs in this figure show light propagation after exiting the optical element – 0μm is set at the exit plane of the optical element. In both cases the intensity was averaged over a radius of 1μm from the centre of the propagation axis.

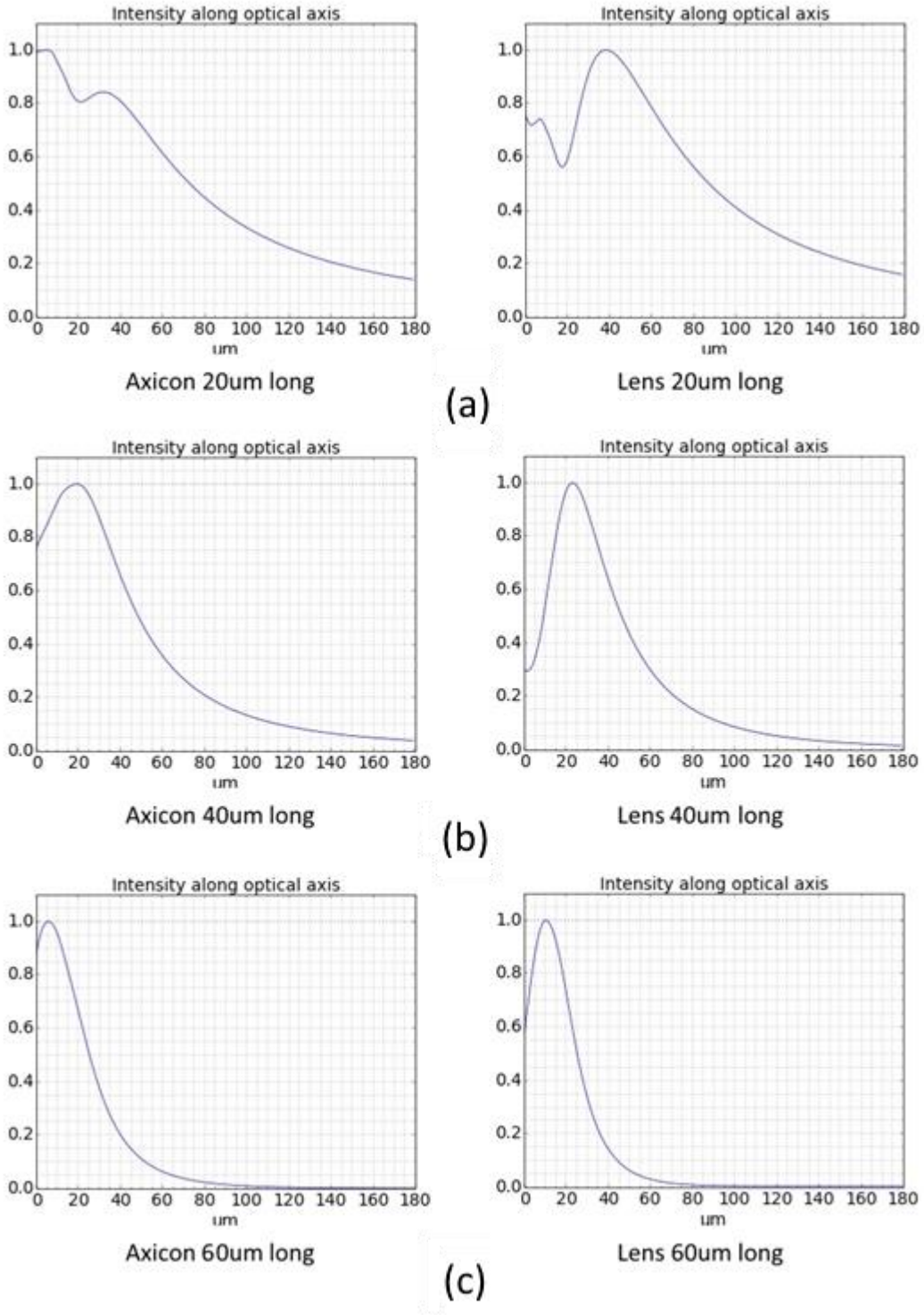

Figure 4.17 - Light intensity along optical axis for axicons and lenses: (a) results for the 20μm long, (b) results for the 40μm long, (c) results for the 60μm long. The intensity is averaged over radius of 1μm from the centre of the propagation axis. In all graphs 0μm is set at the exit plane of the optical element.

Direct comparison shows that depth of focus, defined as the region where light intensity along the optical path is exceeding 0.7 of the maximum light intensity, is longer for the axicons (Table 4.1).

Nanostructured element length	Axicon	Lens	Difference
20μm	52μm	43μm	9μm
40μm	38μm	24.5μm	13.5μm
60μm	19μm	18.5μm	0.5μm

Table 4.1 – Comparison of depth of focus for nanostructured axicons and lenses. Depth of focus is calculated from the exit plane of the optical element.

The 0.5μm difference for the 60μm axicon and lens stems from the fact that for the axicon the working distance is negative, i.e. part of the field of focus is inside the axicon.

4.3. Conclusions

The first FFT BPM simulations for the infinite ideal lens attached to the fibre shows that change of the light source does not change the response of the setup. This confirms that microlenses attached directly to the fibres will work the same as lenses in free space (table 4.1)

	Geometrical optics results	Ideal lens with Gaussian source	Ideal lens with fibre source
Quarter pitch length	75.84μm	76μm	76μm

Table 4.1 - Comparison of theoretical and simulation lens parameters.

The next set of simulations performed for various lengths of the lenses show, as can be expected, that for shorter lenses (20μm) the focal plane has a smaller working distance and greater peak light intensity. This is standard behaviour for lenses with different f-number. The final set of simulations shows that the initial assumptions behind using axicons were correct. Given the same diameter and refractive index differences inside optical element axicons have greater depth of focus (for to 40μm optical element the difference is 13.5μm).

4.4. References

[4.1] J. W. Goodman, *Introduction to Fourier Optics*, ISBN: 0-9747-0772-4, MaGraw-Hill, 2nd ed. (1996)

[4.2] J. M. Nowosielski, *Nanostructured Birefringent and Gradient-Index Micro-Optical Elements*, Thesis collection, Heriot Watt University (2014)

5. DESIGN OF THE ELEMENT STRUCTURE

In this Chapter the discretisation process that allows the creation of nanostructured lenses is shown. The discretisation is based on the desired ideal refractive index distribution.

In section 5.1 the effective medium theory is introduced, which is the base for the discretisation method. According to that theory a continuous refractive index distribution can be substituted by a given discrete subwavelength distribution of glass rods with only two refractive indexes. In sections 5.2 and 5.3 the Simulated Annealing algorithm and its use in this thesis is described. As a direct analytical or numerical calculation of the rod arrangement corresponding to the desired distribution of the effective refractive index is too time and resource consuming, a stochastic optimization method is needed [5.1]. For the 4000 rods, each with two possible states (two different refractive indices) the number of possibilities is 2^{4000}. The Simulated Annealing method belongs to the family of Monte Carlo methods. It is best suited to solving optimisation problems for large search space with discrete elements. In our case the discrete elements in question are all possible refractive indices of every single rod in the nanostructure – around 4000 rods, each with two possible refractive indices. Section 5.4 shows the FFT BPM simulations of light propagation through optical elements with continuous refractive index distribution and comparisons to the discreet designs obtained through Simulated Annealing algorithm.

5.1. Effective medium theory

In order to describe a nanostructured dielectric material in terms of effective permittivity ε_{eff} an effective medium theory (EMT) can be used. This theory is a basic mixing rule inspired by the Maxwell-Garnet formula [5.2]. This can be done as long as the feature size of the nanostructure is smaller than the wavelength of the propagating light. The original Maxwell-Garnet formula has been derived for a situation in which spherical inclusions of permittivity ε_i are randomly distributed inside dielectric medium with permittivity ε_e.

The definition of the relative effective permittivity ε_{eff} of the dielectric medium can be described by an equation [5.2, 5.3, 5.5].

$$\langle \mathbf{D} \rangle = \varepsilon_{eff} \varepsilon_0 \langle E \rangle \,, \tag{5.1}$$

where $\varepsilon_0$describes the vacuum permittivity, < $\boldsymbol{E}$ > describes a volume average of the electric field $\boldsymbol{E}$ and < $\boldsymbol{D}$ > describes a volume average of the electric displacement $\boldsymbol{D}$. The volume average of the electric field can be expressed by an equation [5.2,5.5]

$$\langle E \rangle \geq f E_i + (1-f) E_e \,, \tag{5.2}$$

where *f* is an inclusion fill factor. It is equal to a fraction of the volume occupied by the inclusions. $\boldsymbol{E}_i$ describes the electric field inside such inclusions while $\boldsymbol{E}_e$ describes it outside the inclusions. Analogous equation can be written for the average electric displacement.

This means that the Maxwell-Garnet mixing formula can be written as [5.2, 5.5]

$$\varepsilon_{eff} = \varepsilon_e + 3f\varepsilon_e \frac{\varepsilon_i - \varepsilon_e}{\varepsilon_i + 2\varepsilon_e - f(\varepsilon_i - \varepsilon_e)} \,. \tag{5.3}$$

Because the difference of both permittivities is $\varepsilon_i - \varepsilon_e << 1$, an approximation given by the first order Taylor expansion of formula (5.3) can be used. It means that the effective permittivity can be simplified to form (5.4) if first terms of Taylor expansion are considered [5.2,5.5]

$$\varepsilon_{eff} \approx \varepsilon_e + f(\varepsilon_i - \varepsilon_e) \,, \tag{5.4}$$

As long as the electromagnetic fields are treated as quasi-static, the Maxwell-Garnet formula (5.3) and the simplification of it given by (5.4) can be used for optical fields, despite the fact that it has been derived for the electrostatic case. It is difficult to determine a strict limit of the quasi-static approximation, but it can be assumed that the approximation is working when the feature size of the nanostructure is sufficiently subwavelength.

In this work the effective permittivity distribution inside nGRIN microlenses will be calculated using formula (5.4). The simplified formula can be used because the beam propagates nearly parallel to the nanorods in the direction of *Z* axis, with the refractive index distribution being invariant along *z* axis. The structures discussed in this thesis also have a refractive index difference that changes depending on the pair of glasses used and the wavelength of the incident light, but never exceeds 0.04. This difference also satisfies requirement for the first order Taylor expansion (5.4). The component of wavevector *k* perpendicular to the rods is smaller than $\frac{2\pi}{\lambda}$, which implies that the effective index approach can work for larger rod diameter than $\frac{2\pi}{\lambda}$. The $\frac{2\pi}{\lambda}$ value is given in [5.2] as an estimated limit of the quasi-static approximation.

5.2. Concept of the Simulated Annealing algorithm

As mentioned in the introduction to this chapter, direct analytical or numerical calculation of the rod arrangement corresponding to the desired distribution of the effective refractive index is too time and resource consuming. In order to obtain results a stochastic optimization method called Simulated Annealing (SA) must be used [5.1]. SA solves the problem when a global minimum of a cost function *H(S)* has to be found. A value *E* is assigned to each state *S* of the system through the function *E = H(S),* which is called the cost function for a particular problem. In this case it may be thought of as an error function – difference between state *S* of the rods distribution and the ideal refractive index distribution. In general, the cost function might have some local minima apart from the global minimum. In theory the Simulated Annealing algorithm is able to find a global minimum of the cost function for a given finite problem but it may take infinite time. As time is always limited there is no guarantee to find a global minimum in the strict sense, only a good approximation of the optimal solution provided an efficient cooling protocol is chosen. In Fig. 5.1 a flowchart of the SA method is shown. In the first step random initial state S of the system is chosen. In the next step a random trial state *S'* is chosen. If $H(S') \leq H(S)$ the trial state S' is accepted and the initial state S is substituted by it *(S := S')*.

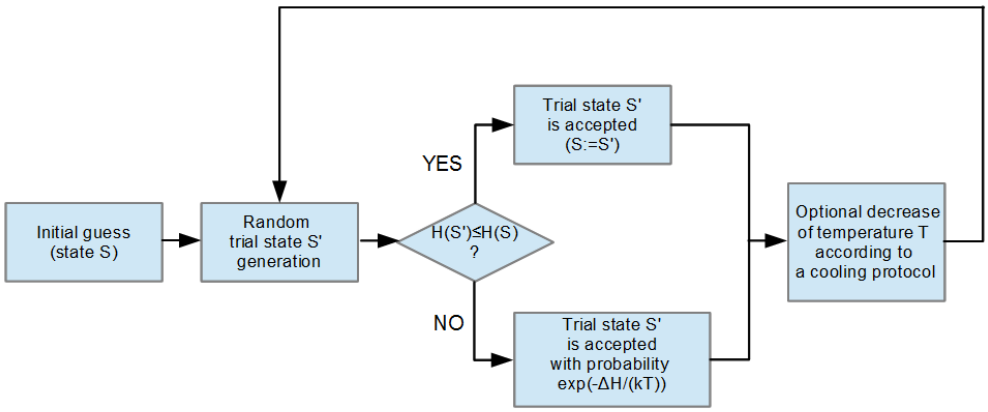

Figure 5.1 - The flowchart describing Simulated Annealing method.

If $H(S') > H(S)$ the probability of acceptance is described by the transition rate $w(S \to S')$ which was introduced by Metropolis *et al.* [5.4,5.5]

$$w(S \to S') = exp\left[\frac{-(H(S')-H(S))}{kT}\right], \tag{5.5}$$

where *k* is a constant and *T* corresponds to the temperature parameter and *H(S)* function corresponds to the error of the given state. In our case the parameter T does not represent a real physical temperature. As the SA algorithm is based on the annealing of metals, the names of the various parameters used represent this basis. After the acceptance or rejection of the new state, the steps are repeated for the new trial state generated. During SA the parameter *T* is decreased gradually. For $T > 0$ a trial state with a higher error function *H(S)* than the last state is accepted with probability $w(S - S')$, so the system does not stop in a local minimum of the cost function. For a fixed *T* the probability that state *S* occurs as the m-th element is given by a Boltzmann distribution [5.1,5.5]

$$P_{eq}(S) = \lim_{m\to\infty} P_m(S) = \frac{1}{Z}\exp\left(\frac{-H(S)}{kT}\right). \quad (5.6)$$

A lower value of *H(S)* has a higher probability $P_{eq}(S)$. The idea of the SA algorithm is to search for the solution for lower and lower temperatures *T*. This translates to a rough search at the beginning (high *T*) followed by a fine search at the end of the procedure ($T \to 0$) [5.5].

5.3. Use of the Simulated Annealing for the element design

In this thesis the Simulated Annealing method is used for optimisation of the rod placement in the nanostructured micro-element. Each nanostructured optical element consists of individual nanorods placed along the optical axis (Z axis of the lens). Therefore, the value of the refractive index within the lens is independent of the z coordinate. This limits the design to a 2D problem in the cross-section plane of the lens.

A particular subwavelength structure can be described as a single state S. As there are two types of nanorods in the structure, characterised by two different refractive indices, a new trial state S' is generated by changing a refractive index of the random rod. A function H(S) is introduced. This function represents the difference between the calculated effective refractive index distribution $n_{eff}(x_i, y_j)$ and the ideal (target) refractive index distribution $n_{ideal}(x_i, y_j)$ at all positions *i* and *j* – an error function [5.1].

$$H(S) = \sum_{i,j}\left|n_{eff}(x_i, y_j) - n_{ideal}(x_i, y_j)\right| \quad (5.7)$$

The sum (5.7) is calculated for all rods included in the structure. The optimisation algorithm tries to minimise the cost function *H(S)* (5.7). When the value of *H(S)* is close to 0 then the effective refractive distribution $n_{eff}(x, y)$ is similar to the ideal (target) refractive index distribution $n_{ideal}(x, y)$.

The algorithm starts with predetermined $T_1 > 0$. For this given temperature large number of trial states are generated. Next the temperature is lowered $T_2 < T_1$ and the procedure is repeated. This procedure is repeated for each decreasing value of temperature, generally over temperature 100 steps are considered. In the last step the temperature is set to be 0 and again a large number of trial states are generated. In fig. 5.2 a target (ideal) refractive index distribution and the corresponding optimised distribution of nanorods inside the nGRIN micro-element are shown in fig.5.3a. The resulting averaged effective refractive index distribution is presented in Fig. 5.3b.

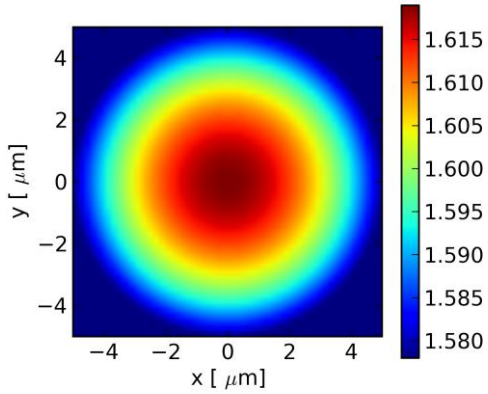

Figure 5.2 - Example of an ideal (target) refractive index distribution in the cross-section of the GRIN micro-element.

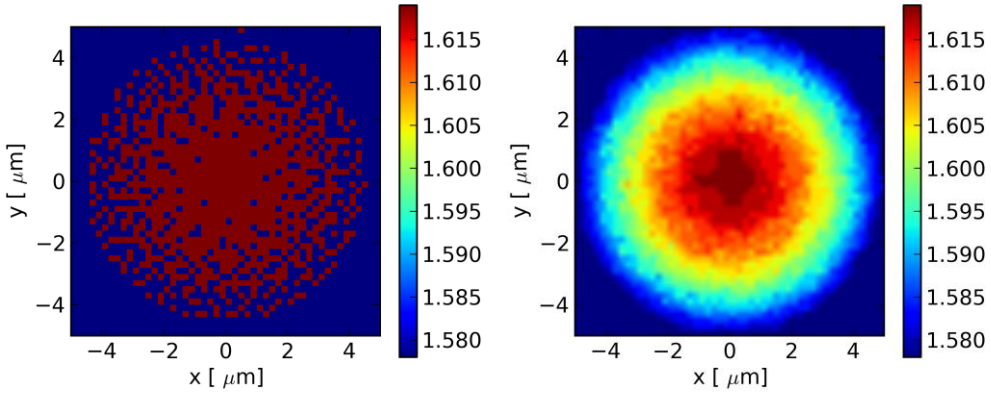

(a) (b)

Figure 5.3 - Example of nanorods arrangement inside nGRIN micro-element (a) and the corresponding effective refractive index distribution (b).

There are a number of parameters that can be varied in order to obtain best possible solution to this problem. There is number of steps that the algorithm takes when lowering the temperature from T_1 to 0. Numerous simulations show that when increasing the

number of temperature steps beyond 140 the cost function remains the same. The simulations were done with maximum number of temperature steps reaching 300 with the same result. The second variable is the number of trial states generated at each temperature. Again repeated simulations show that increasing number of trial states generated for each temperature beyond 200000 does not change the cost function. Those tests were performed with maximum of 1000000 trial states generated for each temperature. Third is the area over which the refractive index is averaged when compared to the ideal distribution. In this case the lowest possible cost function was obtained for 0.99 length unit of the simulation. The simulations were performed for averaging radius changing from 0.1 to 1. The lowest obtained cost function was $H(S) = 2.788$ for 0.99 unit length refractive index averaging, 150 temperature steps and 20000 random states generated for each temperature step (table 5.1).

Cost function H(S)	Temperature steps	Random states for each temperature	Effective index averaging radius
78.4567	150	200000	0.1
14.4208	150	200000	0.3
7.45631	150	200000	0.5
7.81487	150	1000000	0.5
3.04171	150	200000	0.9
3.09654	150	1000000	0.9
2.788	150	200000	0.99

Table 5.1 - Cost function depending on the simulation variables.

Because of the random nature of the states generated at each temperature the cost function for the same initial parameters could vary by 0.1 in subsequent simulations.

5.4. Verification of the element design

The optimisation algorithm, based on the Simulated Annealing (SA) method, has been used for designing the small-diameter nanostructured GRIN micro-elements. The original algorithm was developed by J. Nowosielski [5.5] and F. Hudelist for the calculation of a uniform rod distribution creating optical elements with specified refractive index. For this thesis, this algorithm was modified in order to provide rod distribution according to the specified refractive index profile.

Both the continuous and the corresponding nanostructured GRIN microlenses have been simulated with the BPM technique [5.6, 5.7] using software developed at Heriot Watt University. In the simulations microlenses are enclosed in media with refractive index equal to the lowest refractive index of the nanostructured element. This is done in order to avoid the back reflection from the lens facets, and thus to facilitate an investigation of the Gaussian beam propagation in GRIN medium. 3D simulations have been done for the lenses and axicons investigated in detail during this work. For the purpose of this investigation both elements are infinite in length. This should allow comparing pitch length of the ideal and nanostructured elements.

For the convenience of the reader the same simulations as shown in Chapter 3 are again shown below. The area of the simulation consisted of a Gaussian source with 4.6μm width introducing light into a 400μm length of single mode fibre. The source has wavelength equal to 1550nm. The core of the fibre has 4.6μm in diameter with refractive index 1.452. Refractive index of the cladding equals to 1.446. (Fig.5.4).

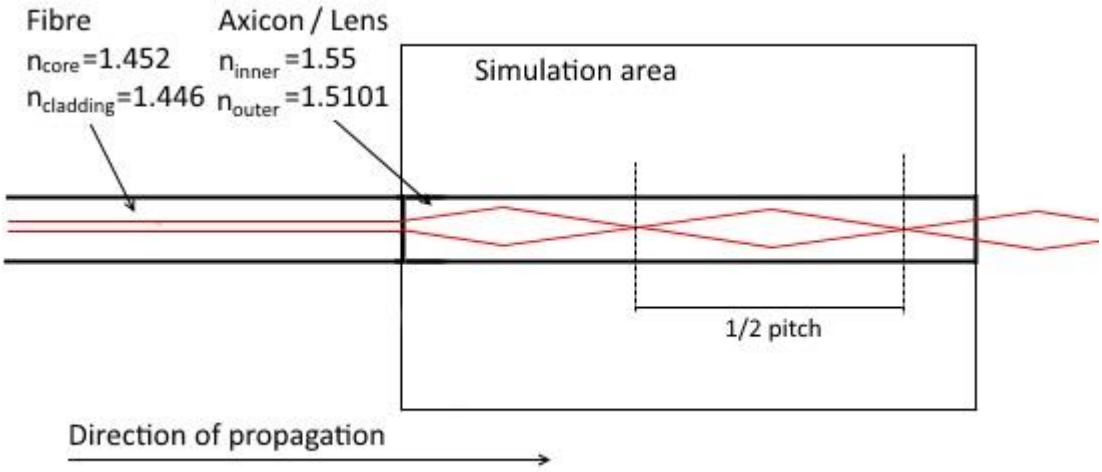

Figure 5.4 - Schematic of the area of the FFT BPM simulation.

As it has been shown in Chapter 3 for the on-axis refractive index of the lens n_0 = 1.5432. The diameter of the microlens is 20μm leading to a minimum refractive index n_{min} of 1.5101. The refractive index distribution within a continuous GRIN microlens is described by Eq. (5.8).

$$n_r = n_0\left(1 - \frac{A}{2}r^2\right) \tag{5.8}$$

As is explained in Chapter 2 a ray incident on the front surface follows a sinusoidal path along the rod. The period of the sinusoidal path ("pitch" of the lens) is given by

$$P = \frac{2\pi}{\sqrt{A}} \tag{5.9}$$

In this case half of the pitch of the lens equals 151.69μm. Half pitch of a lens is clearly visible on a field propagation simulation as a distance between closest focal planes inside infinite lens. As can be seen on fig 5.5 the half pitch of the simulated ideal lens equals to 151μm.

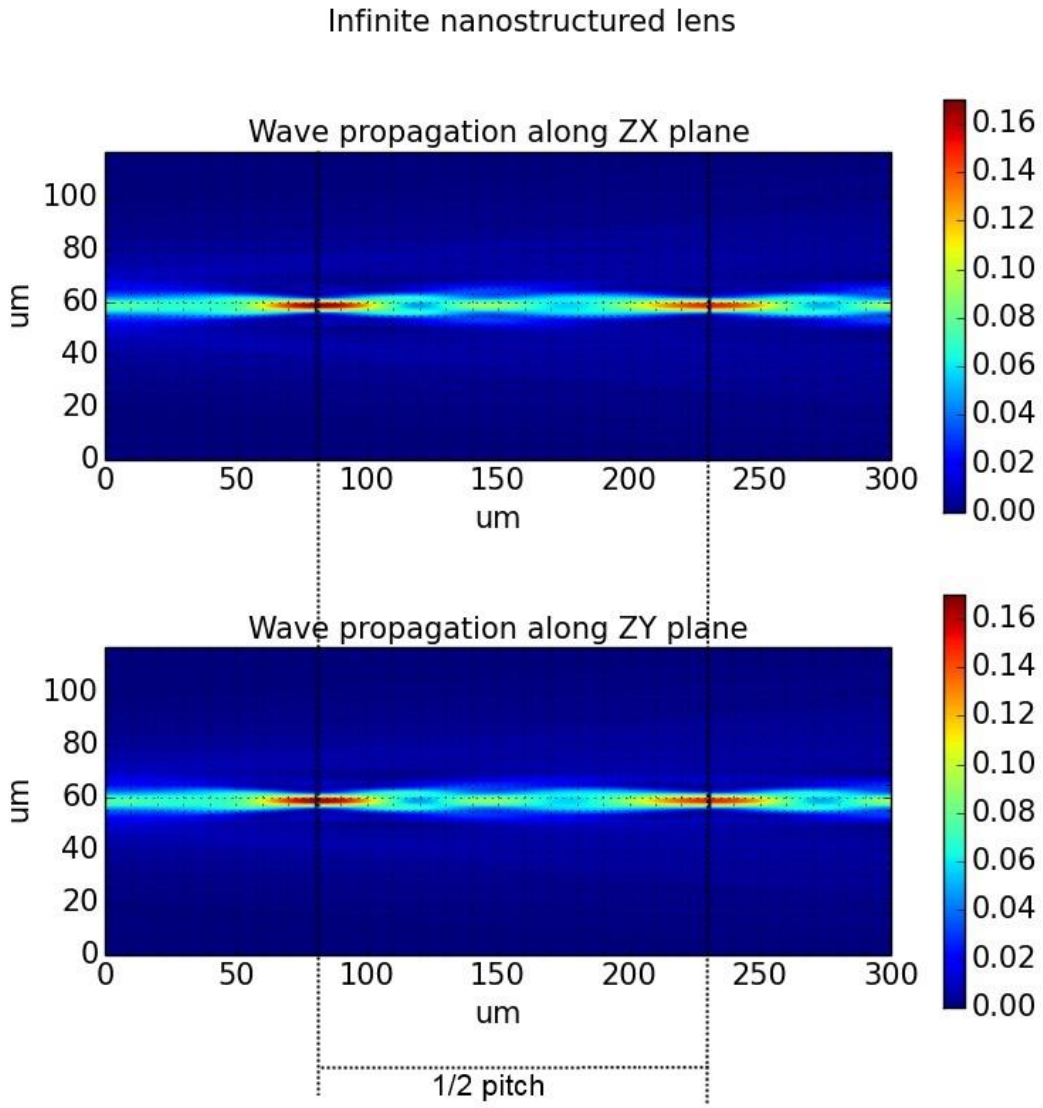

Figure 5.5 - Light propagation through infinite ideal lens. Two closest focal planes are shown. Lens is directly attached to the fibre. Blue vertical lines show positions of the highest amplitudes for both planes.

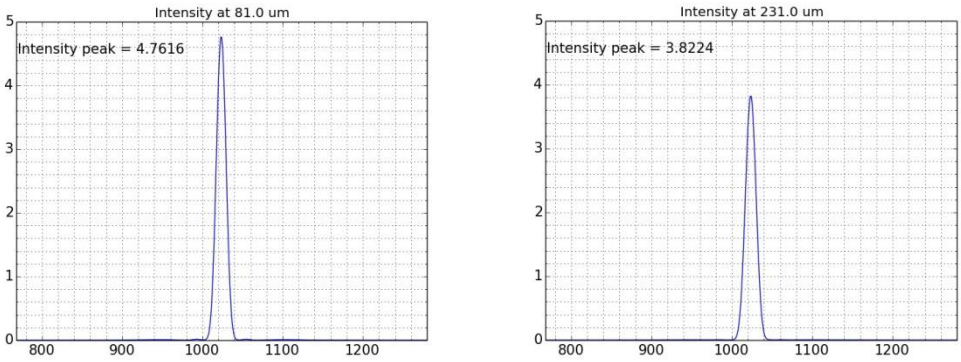

(a) (b)

Figure 5.6 - First (a) and second (b) focal plane along the light propagation through the infinite ideal lens. Both peaks show intensity as fractions of the intensity at end plane of the fibre. Intensity of the second focal equals to 80% of the first.

This is in line with the theoretical results, the half micron difference stems from the fact that the simulation was done with a 1μm step.

Fig 5.8 show the focal planes for the nanostructured lens. The structure of the lens in this simulation is shown in Fig. 5.7. The lens has 100 rods on the diagonal of the hexagon. This means that for the given diameter of 20μm each rod has diameter equal to 200nm. For the λ_0 = 1550 nm incident wavelength each rod is equal to $\frac{\lambda 0}{7.75}$. The cost function for this lens was minimised at H(S) = 2.788.

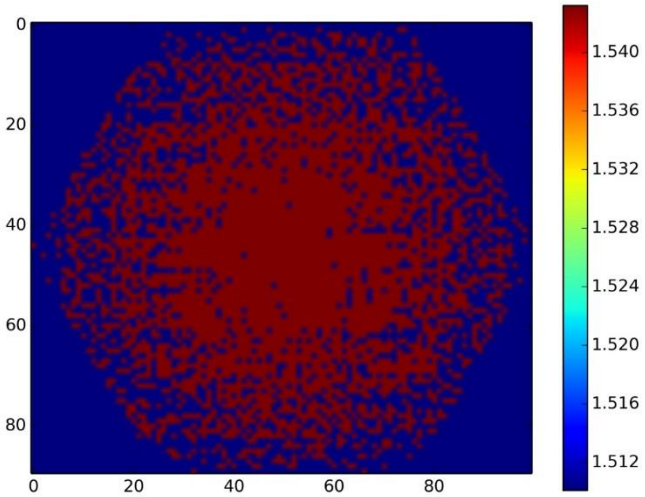

Figure 5.7 - Structure of the nanostructured lens. The cost function of this structure was minimised at 2.788. Each red dot represents glass rod with higher refractive index, while blue represents rods with lower refractive index.

Both the ZX and ZY planes of the simulation are shown. This shows that despite not being ideally circular the refractive index distribution of the nanostructured lens performs in the same way for both propagation planes.

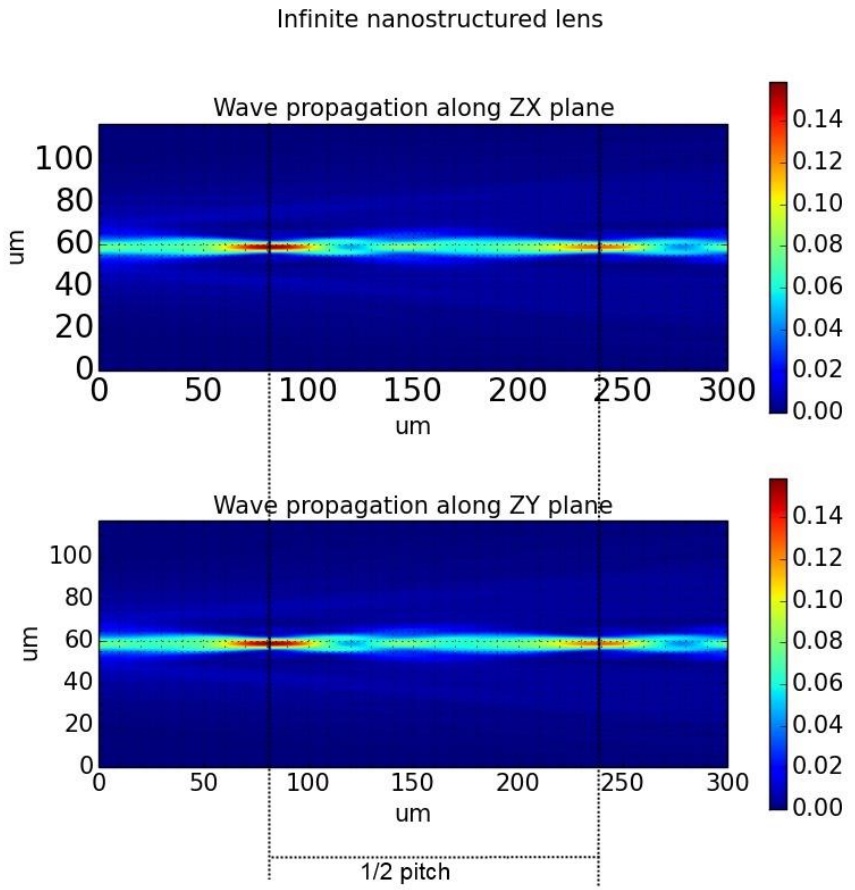

Figure 5.8 - Light propagation through infinite structured lens. Two closest focal planes are shown. Lens is directly attached to the fibre. Blue vertical lines show positions of the highest amplitudes for both points. Second focal plane is visibly weaker than in an ideal lens.

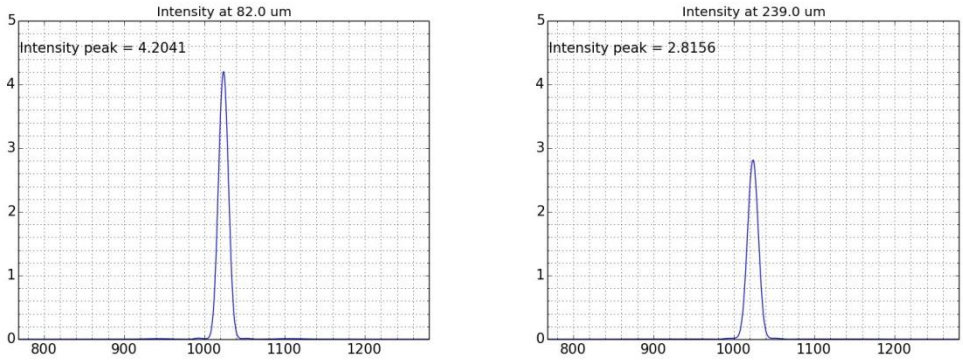

(a) (b)

Figure 5.9 - First (a) and second (b) focal plane along the light propagation through the infinite ideal lens. Both peaks show intensity as fractions of the intensity at end plane of the fibre. Intensity of the second focal equals to 66% of the first.

It is clear that the half pitch for these lenses is longer then for the ideal lenses, equal to 157μm. This shows that during the conversion from ideal to nanostructured lens the refractive index profile in the lens changed. This is further backed up by the fact that the cost function of the SA algorithm was minimised at 2.788 for this lens. By comparing the field peak in the fig 5.9 one can see that maximum field amplitude in the second focal plane is lower for the nanostructured lens, 66% of the first focal plane, compared to 80% for the ideal lens. This again suggests that the nanostructured lens has a lower efficiency than the ideal lens. Since lenses fabricated for this thesis are supposed to have a length no larger than the half pitch, which is the length between those focal planes, this should not pose a problem.

The same comparison of nanostructured and ideal element was done for axicons. The distance between two closest points of maximum intensity along optical axis equals to 145μm for ideal axicon (Fig. 5.10, 5.11).

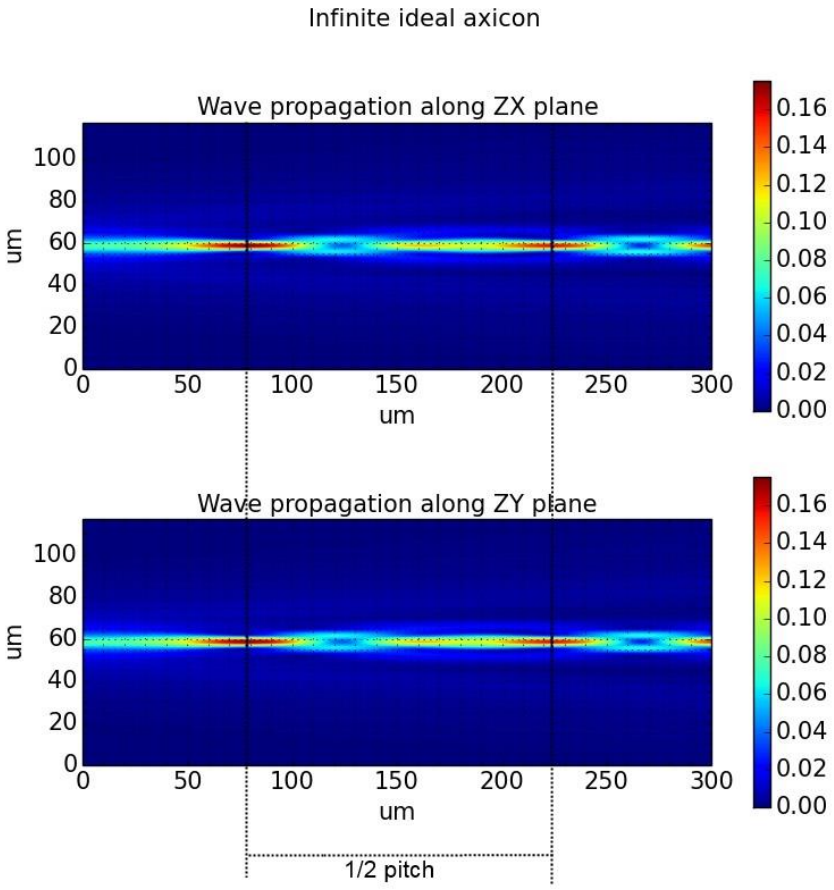

Figure 5.10 - Light propagation through infinite ideal axicon. Two closest focal planes are shown. Axicon is directly attached to the fibre. Blue vertical lines show positions of the highest amplitudes for both planes.

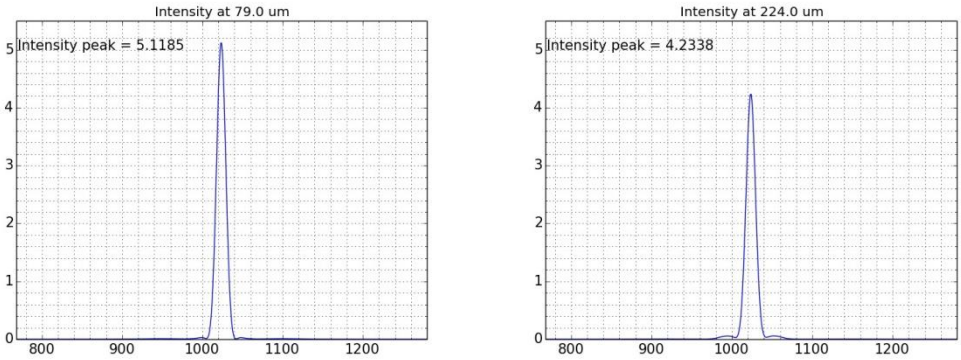

(a) (b)

Figure 5.11 - First (a) and second (b) focal plane along the light propagation through the infinite ideal axicon. Both peaks show intensity as fractions of the intensity at end plane of the fibre. Intensity of the second focal plane equals to 82% of the first.

Fig 5.13 shows the focal planes for the nanostructured axicon. The structure of the axicon in this simulation is shown in Fig. 5.12. As for the nanostructured lens, the axicon has 100 rods on the diagonal of the hexagon. This means that for the given diameter of 20μm each rod has diameter equal to 200nm. For the λ_0 = 1550 nm incident wavelength each rod is equal to $\frac{\lambda 0}{7.75}$. The cost function for this lens was minimised at H(S) = 3.03881.

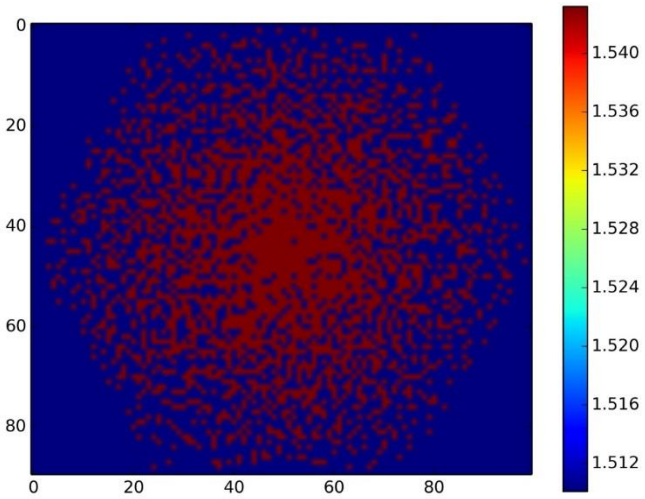

Figure 5.12 - Structure of the nanostructured axicon. The cost function of this structure was minimised at 3.03881. Each red dot represents glass rod with higher refractive index, while blue represents rods with lower refractive index.

Both ZX and ZY planes of the simulation are shown. This shows that despite not being ideally circular the refractive index distribution of the nanostructured axicon performs in the same way for both propagation planes.

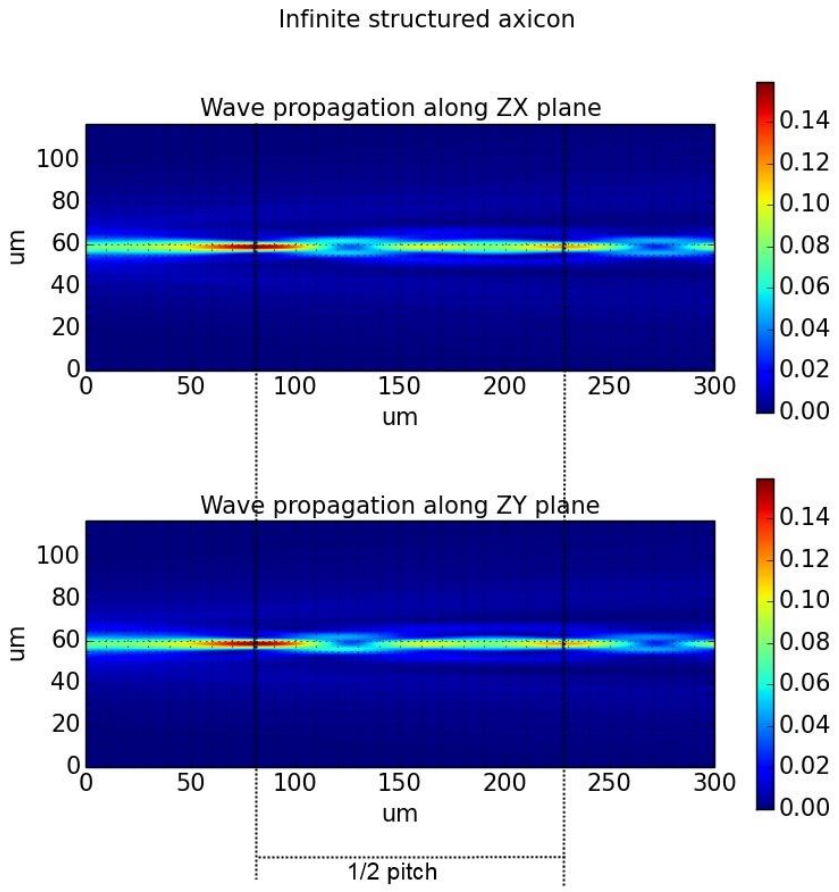

Figure 5.13 - Light propagation through infinite structured axicon. Two closest focal planes are shown. Axicon is directly attached to the fibre. Blue vertical lines show positions of the highest amplitudes for both points. Second focal plane is visibly weaker than in an ideal lens.

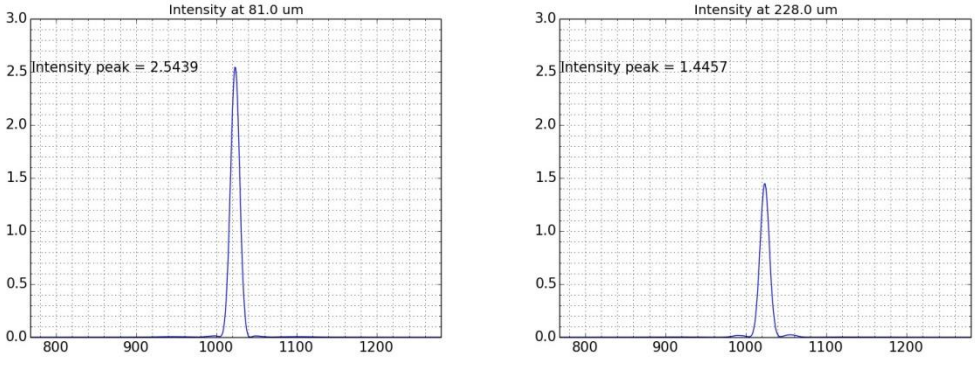

(a) (b)

Figure 5.14 - First (a) and second (b) focal plane along the light propagation through the infinite ideal axicon. Both peaks show intensity as fractions of the intensity at end plane of the fibre. Intensity of the second focal equals to the 56% of the first.

The distance between two closest points of maximum intensity along optical axis equals to 147μm for nanostructured axicon. This again shows that during the conversion from ideal to nanostructured axicon the refractive index profile in the lens changed, which is confirmed by the cost function of the SA algorithm minimised at 3.03881. By comparing the field peak in the Fig 5.14 one can see that maximum field amplitude in the second focal plane is lower for the nanostructured lens, 56% of the first focal plane, compared to 82% for the ideal lens. This again suggests that nanostructured axicon has a lower efficiency then the ideal axicon. This may be the result of the fact that at the centre of the ideal axicon the refractive index profile has a sharp point. Such a shape cannot be completely reproduced by the distribution of nanorods, each 200nm in diameter.

5.5. Conclusions

It has been shown that in the case of nanostructured GRIN microstructures (fabricated with the stack-and-draw technique) a simple formula may be used for calculation of the effective refractive index. According to [5.2] this can be done when the diameter of the single structural element of the nanostructure is equal to or smaller than $\lambda/2\pi$. Tests conducted by J. Nowosielski [5.5] have shown that, for structures continuous along the optical axis of the setup, the diameter of the single element (nanorod) of the nanostructure can be equal to or smaller than $\frac{\lambda_0}{7.75}$. The difference between the refractive indices of the used materials may be not larger than approximately 0.04, the beam must propagate close to parallel to the nanostructure in the direction of the Z axis, with the refractive index constant in that direction.

Computer simulations show that the SA algorithm produces nanostructured lenses with a half pitch longer by 3.9% (table 5.1) from the ideal lens for the cost function of the SA algorithm minimised at 2.788.

	Geometrical optics results	Ideal lens with Gaussian source	Ideal lens with fibre source	Nanostructured lens with fibre source
Quarter pitch length	75.84μm	76μm	75.5μm	78.5μm

Table 5.1 - Comparison of theoretical and simulation lens parameters.

Further minimisation of the cost function is not advisable as it is very resource and time consuming. It can be seen that the efficiency of the lens is lower and that the refractive

index distribution profile changes slightly from the ideal situation. In the ideal lens the field amplitude in the second focal plane along the propagation path is equal to 80% in the first focal plane. For the nanostructured lens, the amplitude in the second focal plane is equal to 66% of the first focal plane. This is the result of the differences between ideal and effective refractive index distribution. In the nanostructured lenses those differences introduce additional light scattering, lowering the efficiency of the lens. In this thesis we are discussing only elements that are no longer than a ½ pitch, which are not affected by losses over longer distances. This includes lenses and axicons used as focusing elements for fibres.

For the axicons, the length of the distance between two closest points of maximum intensity along the optical axis equals to 147μm for the nanostructured axicon and 145μm for the ideal axicon. The nanostructured axicon has visibly lower efficiency than the ideal one, with the second intensity peak being only 56% of the first, compared to 82% for the ideal axicon.

5.6. References

[5.1] A. K. Hartmann, H. Rieger, *Optimization Algorithms in Physics*, ISBN 3-527-40307-8, Berlin: Wiley-VCH (2002)

[5.2] A. Sihvola, *Electromagnetic Mixing Formulas and Applications*, ISBN 0-85206-772-1, London: The Institution of Electrical Engineers (1999)

[5.3] L. D. Landau, E.M. Lifshitz, *Electrodynamics of Continuous Media*, ISBN: 978-0-08-030275-1, Course Theor. Phys 8, Oxford: Pergamon Press (1960)

[5.4] N. Metropolis, A. Rosenbluth, M. Rosenbluth, A. Teller E. Teller, *Equation of state calculations by fast computing machines*, Journal of Chemical Physics, 21(6), 1087-1092 (1953)

[5.5] J. M. Nowosielski, *Nanostructured Birefringent and Gradient-Index Micro-Optical Elements*, Thesis collection, Heriot Watt University (2014)

[5.6] F. Hudelist, R. Buczynski, A.J. Waddie, M. R. Taghizadeh, *Design and fabrication of nano-structured gradient index micro-elements*, Optics Express, 17(5) (2009)

[5.7] J. M. Nowosielski, R. Buczynski, F. Hudelist, A.J. Waddie, M. R. Taghizadeh, *Nanostructured GRIN micro-elements for Gaussian beam focusing*, Optics Express, 17, 3255-3263 (2009)

6. MATERIALS USED IN GRIN ELEMENTS FABRICATION

The choice of materials for nanostructured fabrication is of critical importance to the final fabricated elements. The materials used define the refractive index difference in the nanostructured elements. Depending on the thermal compatibility of the materials severe stresses can be introduced into the structure. This chapter outlines the various glasses available and describes the criteria for the final selection of glasses.

In the section 6.1 we describe various glasses that were available to us and describe criteria that the glasses need to fulfil. The section 6.2 of this chapter deals with proof of concept for the future use of polymers in nanostructure fabrication. The polymers were chosen as a cheaper alternative to glass for future optical elements fabrication. In addition, polymers do not produce sharp shards when fractured, like glass, making them ideal for in-vivo applications. Section 6.2.1 describes in detail free radical polymerisation method utilised in this thesis. Our goal was to obtain two PMMA based polymers with similar thermal and mechanical parameters but different refractive indices. Section 6.2.2 describes polymerisation of the clear PMMA material, while section 6.2.3 describes changes introduced to the polymerisation process in order to obtain doped PMMA. In section 6.3 two tests performed on the PMMA materials are described. In the first test we used only clear PMMA to fabricate a photonic structure, in the second test we used clear and doped PMMA to fabricate an optical fibre. In both tests fibre was constructed using stack and draw method which was tested and proven for the glasses. Both of those test show possibility of using two distinct polymer materials for creating various micro structured components utilising stack and draw method.

6.1. Optical Glasses

The main structures fabricated for this thesis were made from a variety of soft glasses in order to exploit the pre-existing knowledge of using various glasses in the stack and draw method derived from previous work [6.1-6.4] as well as allowing better matched materials to be utilised together. Two pairs of glasses, F2/NC21 [6.2, 6.5], used in previous research, and NC21/NC34, a previously unreported pair of glasses are considered. The characterisation of the second pair, which is explained in section 6.1.2, shows that it should be possible to thermally process both glasses together. The NC glasses were fabricated at the Institute for Electronic Materials Technology by Jaroslaw Cimek and Ryszard Stępień and F2 glass was bought from Schott.

6.1.1. Chemical composition and fabrication of various glasses

In the stack and draw method, used for the fabrication of nanostructured optical elements, reduction of diameter of the structure is achieved by repeated thermal processes. In order to match a pair of glasses for joint thermal processing, their chemical composition has to be adjusted (Table 6.1). In order to maintain a stable drawing process for the all-solid photonic structure development, both glasses used should have the same viscosity at the same temperature. In reality this case is rarely obtainable. The previous work with optical glasses used in stack and draw method shows that a stable process can be achieved at the temperature difference of ~50°C. The viscosity should be in range between the curvature temperature $\boldsymbol{T_c}$ of the sample and the sphere creation temperature $\boldsymbol{T_{kph}}$, measured using a Leitz heat microscope. Both of those temperatures are defined as a temperature at which the glass viscosity reaches certain point. For the $\boldsymbol{T_c}$, the glass viscosity is equal to $log\,\eta=9.0logP$, while for the $\boldsymbol{T_{kph}}$ $log\,\eta=6.0logP$. P, or Poise is the unit of dynamic viscosity in the centimetre gram second system of units, equal to $1g\times cm^{-1}\times s^{-1}$. The difference of the thermal expansion coefficient for the glasses used should not exceed $\Delta\alpha < 8\ (\pm 2)\times 10^{-7}\cdot K^{-1}$, otherwise the build-up of stress during cooling will crack and warp the fabricated structures.

Glass composition [% mol]	NC-21A	NC-32	NC-34	F2 (commercial)
SiO_2	56.83	54	54	70.72
PbO	-	-	-	18.95
K_2O	3.63	3	2.5	4.94
Na_2O	9.52	8.5	8	5.25
Li_2O	6.23	5	5	-
B_2O_3	23.19	21	21	-
Al_2O_3	0.61	0.5	0.5	-
BaO	-	5	9	-
CdO	-	3	-	-
As_2O_3	-	-	-	0.14

Table 6.1 - Composition of various glasses used in stack and draw component fabrication.

The raw materials used in the glass fabrication had to have minimum purity of 99.8%. Manufactures usually provide raw materials with several levels of purity. 99.8% is the lowest level of purity that is usable for the purpose of glass fabrication for optical applications. Impurities in the raw materials with lower purity level would react with other materials during melting resulting in differences in glass parameter (both mechanical and optical) between batches produced. Proper weight composition was mixed to obtain a homogenous powder and then melted in a furnace (Fig.6.1).

(a) (b)

Figure. 6.1 - (a) Glass melting furnace, (b) Crucible with melted glass removed from the furnace.

For the first samples of the glasses, weights of substrates were adjusted to obtain 100 g glass from each melt. Those samples were used for testing the optical and thermal parameters of those glasses. Preliminary batches were melted in corundum crucibles at a temperature range of 1100 – 1270°C. The melts were poured into preheated graphite forms and annealed from glass transition temperature to room temperature at a cooling rate of 0.5 °/min (Fig. 6.2)

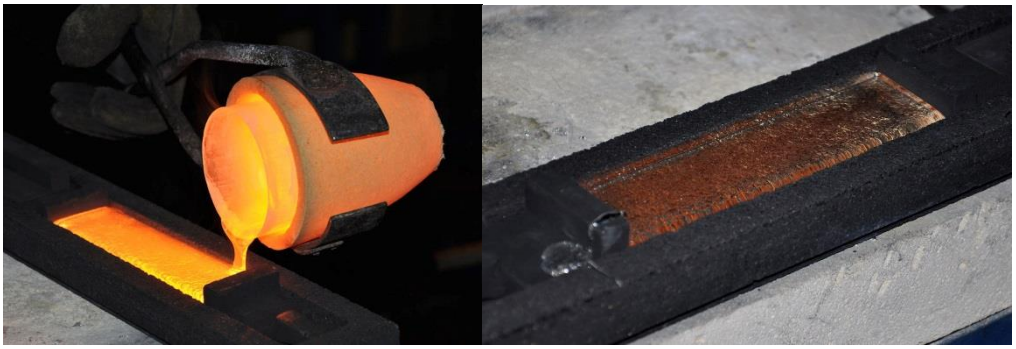

(a) (b)

Figure. 6.2 - (a) Pouring melted glass into graphite form, (b) Cooled glass bar.

After annealing, the glass bars were cut and polished to obtain proper samples for characterization measurements.

6.1.2. Characterization of synthesised glass

After annealing all the synthesized glasses had to be measured to check whether the optical and thermal properties were within acceptable limits. The thermal expansion coefficient, transformation temperature and dilatometric softening point were measured on a BAHR Thermoanalyse GmbH DIL801 dilatometer. The specific temperatures for characteristic viscosities were measured on a Leitz Heat Microscope. The glass susceptibility to crystal formation was checked using the isothermal heating method. Lastly a difference in linear thermal coefficient in the chosen pair of glasses was checked using a “sandwich” test.

In the dilatometer a monochromatic light source, illuminates the glass sample. Some of the light is reflected by the sample and interferes with the incoming light, creating optical interference fringes. As the glass sample contracts or expands, there is a proportional movement of the interference fringes, which can be measured using a camera system. This allows calculation of glass thermal expansion and indicates transformation and softening temperatures. The results of those tests are in Table 6.2

In the Leitz heat microscope, glass samples are slowly heated while observation of the sample is performed under the microscope. At certain temperatures (curvature, sphere, hemisphere and spreading temperature) the glass sample changes shape indicating that a certain viscosity of the sample is reached. Those temperatures are then noted. The results of those tests are in Table 6.2.

Parameter	NC-21A	NC-32	NC-34	F2
Refractive index $\mathbf{n_d}$	1.5273	1.5538	1.5581	1.620
Thermal expansion coefficient for the range 20–300°C α [$10^{-7}\cdot K^{-1}$]	86.6	86.9	87.0	91.9
Transition temperature Tg [°C] for logη=13.4[logP]	504.7	512.7	529.8	431
Dilatometric softening point SP [°C] for logη=11.0[logP]	540	547	562	480
Characteristic temperatures in Leitz heating microscope T [°C] temperature of:				
curvature $\mathbf{T_c}$ for logη=9.0 [logP]	620	640	670	520
sphere $\mathbf{T_{kph}}$ for logη=6.0[logP]	725	720	760	690
hemisphere $\mathbf{T_{hs}}$ for logη=4.0[logP]	775	780	810	820
spreading $\mathbf{T_{spr}}$ for logη=2.0[logP]	860	860	910	1130

Table 6.2 - Optical and thermal parameters of glasses used in this thesis.

The NC21/NC34 pair of glasses have an expansion coefficient difference $\Delta\alpha=0.4\times10^{-7}\cdot K^{-1}$ which is a very good result, far better than previously used F2/NC21 pair which has expansion coefficient difference $\Delta\alpha=5.3\times10^{-7}\cdot K^{-1}$. During the drawing in the drawing tower the glasses are kept at a temperature between the curvature and sphere points measured by the heating microscope. For NC21/NC34 the difference in curvature temperature is $\Delta T_c=50^oC$ and difference in sphere temperature is $\Delta T_{kph}=35^oC$. Those differences are smaller than for the F2/NC21 glasses, for which $\Delta T_c=100^oC$ and $\Delta T_{kph}=35^oC$.

Crystallization susceptibility can be investigated by three methods: differential scanning calorimetry (DSC), diffractive X-ray measurements (XRD) and by isothermal heating

method. The simplest and easiest one to perform is the isothermal heating method. It is also the least accurate one, not as well suited as the other two methods for the characterization of the observed crystals. However, as the aim of the glass synthesis was to avoid crystallization altogether, this method was deemed to be sufficient. Firstly, the sphere creation temperature was determined by the Leitz heat microscope. Then the glass sample with a polished surface was heated for 2 hours up to sphere creation temperature and then slowly cooled down. The sample surface was then inspected for signs of crystallisation using a microscope with attached polariscope. The distribution and sizes of any grown crystals can be compared with the composition changes during the development of the glass series. This allows design corrections in the chemical composition (Table 6.1) of further glass samples to be made, leading in the end to the design of a thermally stable glass. The examples of crystals grown on the glass surface that may appear after the isothermal heating test are shown in Fig. 6.3. Such pictures are observed only for glasses with a clear tendency to crystallization. In thermally stable glasses, the crystals are absent and the glass appears to be uniform.

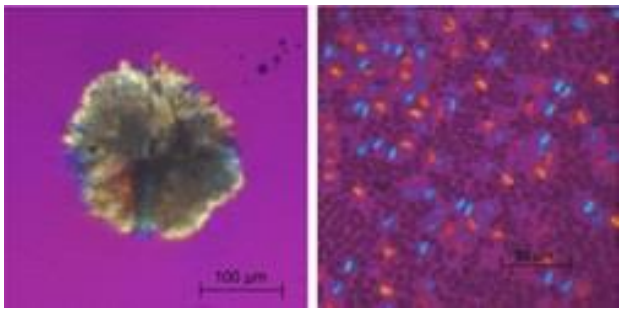

Figure 6.3 - Examples of the crystallization on the surface of the glass sample (polariscope image).

In order to fabricate a stable optical structure comprising two jointly thermal-processed glasses, the difference in linear thermal coefficient has to be minimized, and viscosity of each of the glasses has to be matched (Table 6.1). Excessive difference in linear thermal coefficient introduces stress at the interface of the two materials and results in cracking during cooling, which is especially evident in larger components. A “sandwich” test was performed to check the viability of using the selected pairs of glasses. In this test one polished glass plate is placed between two plates made from different types of glass and, as before, heated to the sphere creation temperature and slowly cooled. After cooling, this “sandwich” structure is cut and polished. The structure is then inspected under a microscope with an attached polariscope. Polariscope consist of two polarisers illuminated by white light. The glass sample positioned between them will rotate the

polarization of light passing through the polariscope. The amount of polarization rotation depends on the amount of stress induced by the difference in the thermal expansion during cooling in the glass sample. This shows as a colour difference when viewed in the polariscope. Images of prepared "sandwich" samples are shown in Fig. 6.4. Again in matched pairs of glasses the discoloration is absent and the glass appears to be uniform.

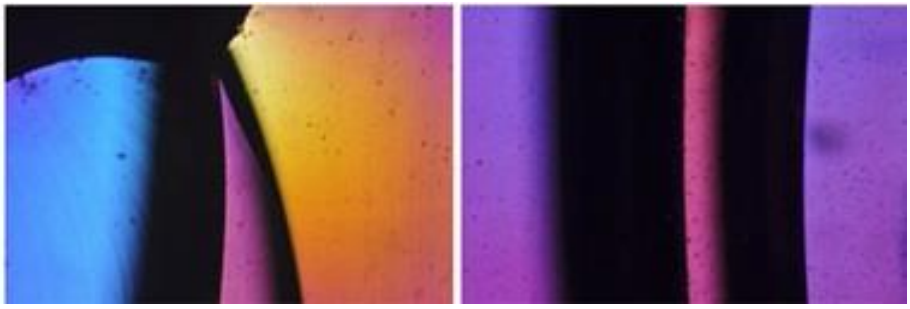

Figure 6.4 - Example of the stresses induced by thermal expansion difference (polariscope image).

6.1.3. Characterization of optical parameters of glasses

Reduction of the refractive index difference between the glasses was necessary in order to achieve the desired optical element length. Initial tests showed that any manipulation of the optical element (such as grinding or polishing) decreases yield of the fabricated nanostructured elements with the decrease of the element length. At length $l < 40\mu m$ the optical elements broke easily resulting in almost 10% yield of fabricated elements. For an optical element length $l > 80\mu m$ the yield during initial fabrication runs were greater than 50%. This was mainly due to the contact area between the optical elements and the base plate during cutting and polishing. For the shorter optical elements contact area was small and the optical elements were removed from the base plate due to friction of cutting and polishing. GRIN lenses quarter pitch length L_{QP}, as is explained in detail in Chapter 2, is related to the lens diameter and refractive index difference in the lens. In the case of the elements used in this thesis for a given diameter of $20\mu m$, and refractive index difference of $\Delta n \sim 0.1$, the quarter pitch would be $L_{QP} \sim 47.12\mu m$. For the same diameter and refractive index difference $\Delta n \sim 0.02$ the quarter pitch length of the GRIN lens would equal to $L_{QP} \sim 105.37\mu m$.

The refractive indices of the selected glasses were measured in a Michelson interferometer. The interferometer used was constructed at the Institute for Electromagnetic Materials Technology for measurements of various fabricated glasses.

The results for the F2, NC21 and NC34 glasses are shown in Figures 6.3, 6.4 and 6.5 respectively.

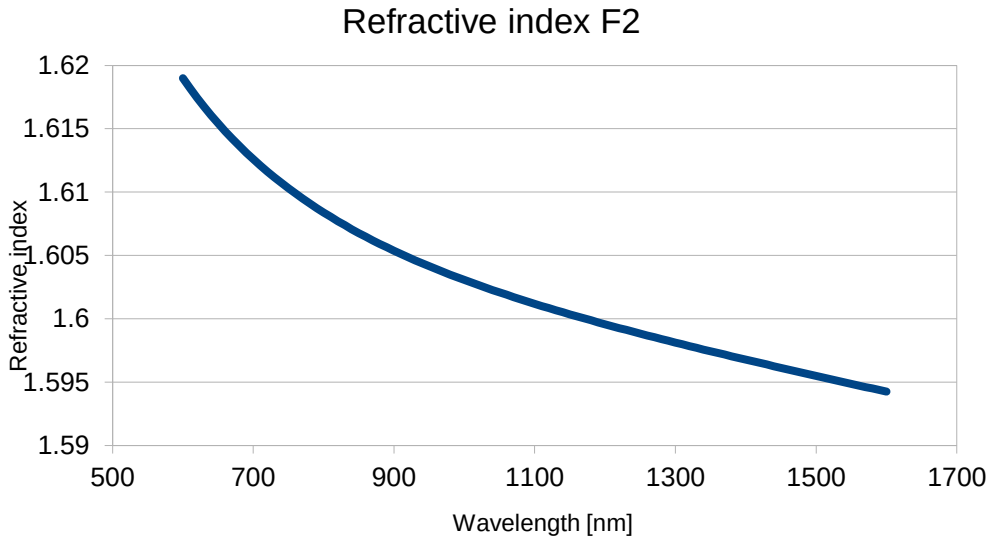

Figure 6.3 - Refractive index of Schott F2 glass as a function of incident light wavelength.

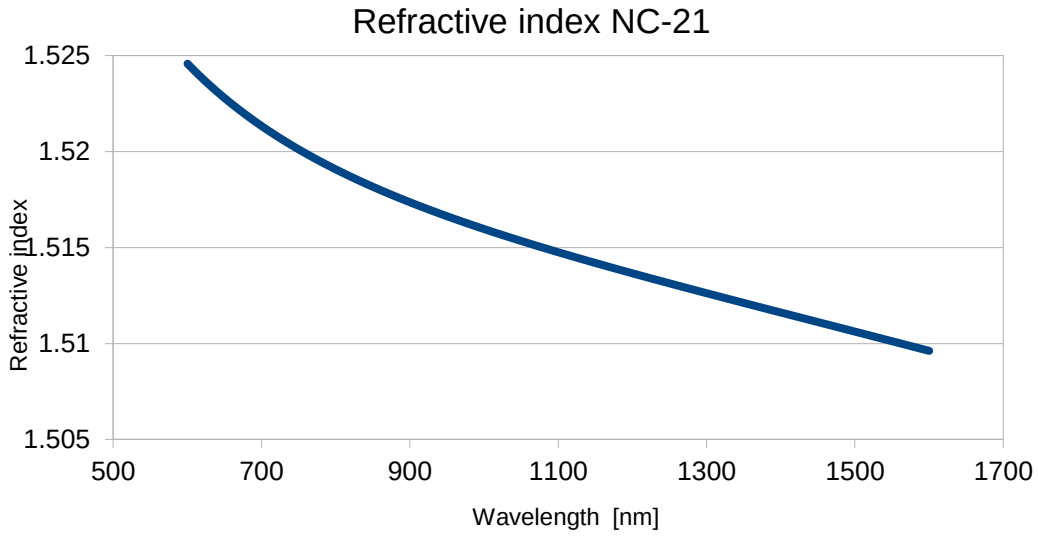

Figure 6.4 - Refractive index of ITME NC21 glass as a function of incident light wavelength.

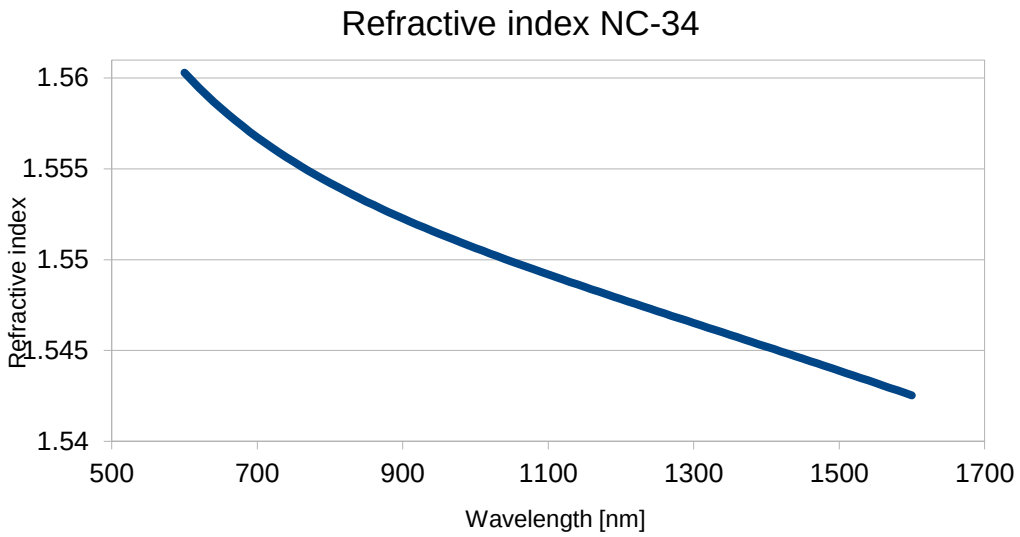

Figure 6.5 - Refractive index of ITME NC34 glass as a function of incident light wavelength.

As can be seen in Figures 6.6 and 6.7 the refractive index difference is smaller for the NC21/NC34 glass pair, which means that the fabricated optical elements have a longer quarter pitch length. For incident light of wavelength 1550nm, a 20μm diameter GRIN lens fabricated from F2/NC21 pair of glasses would have quarter pitch length L_{QP} = 48.18μm. For the same parameters, a lens fabricated using the NC21/NC34 pair would have L_{QP} = 75.84μm. As previously the refractive index difference decreases with wavelength.

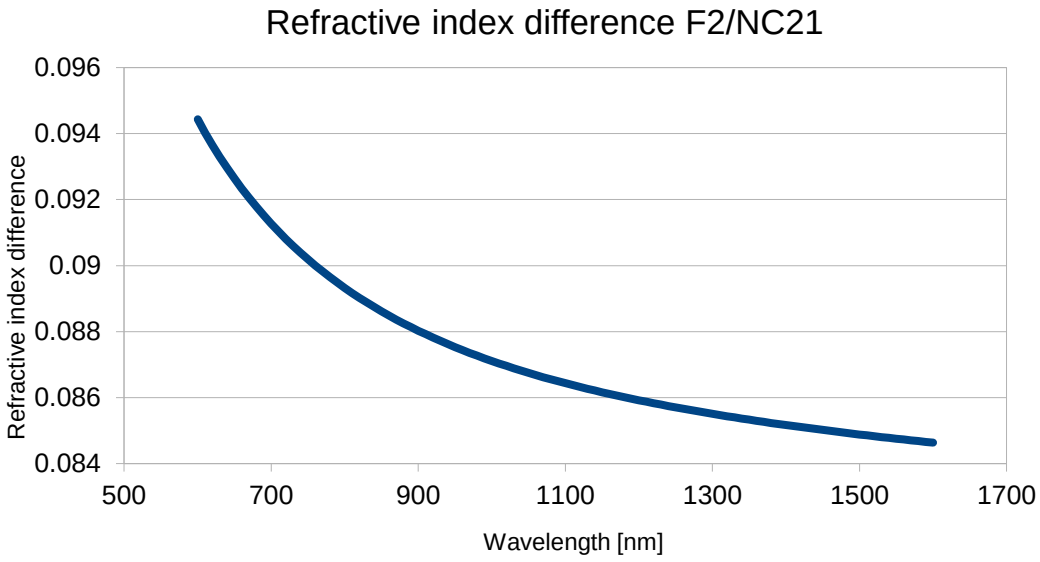

Figure 6.6 - Refractive indexes difference of the F2/NC21 pair of glasses.

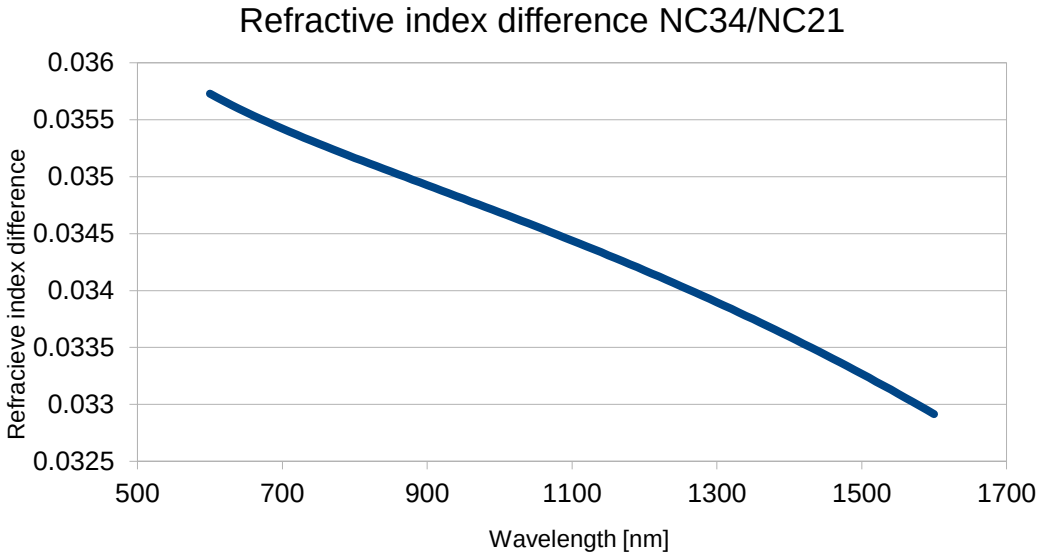

Figure 6.7 - Refractive indexes difference of the NC21/NC34 pair of glasses.

Table 6.3 shows refractive index differences for the wavelength at which experiments and computer simulations were performed.

F2	NC-21	Difference	Wavelength [nm]
1.594	1.510	0.084	1550

NC-34	NC-21	Difference	Wavelength [nm]
1.543	1.510	0.033	1550

Table 6.3 - Refractive index difference for the chosen glass pairs for 1550nm incident wavelength.

6.2. Poly methyl methacrylate (PMMA)

This section describes in detail the polymerisation process of poly methyl methacrylate (PMMA). PMMA polymerisation is a well-known process, but because polymers are a commercially available product the specifics are treated as trade secrets. Since for the joint thermal processing of two distinct PMMA based materials the polymers have to have very specific parameters, both optically and mechanically, it was decided to polymerise both materials in-house. This way the exact chemical composition of the PMMA and its impact on the optical and mechanical properties of the material was

known. Any changes in the chemical composition of the PMMA can dramatically influence optical and mechanical properties such as refractive index, viscosity and melting temperature. The goal in this part of the research work was to create two poly methyl methacrylate (PMMA) based polymers that could be processed together in a drawing tower. This would allow us to design low cost photonic structures with a low refractive index difference. The polymerisation process is a modification (different process time, temperatures at various stages of the process and gas removal method) of the algorithm developed by A. Maniquet, a master student at the Heriot-Watt University.

The fibre-grade PMMA was chosen as a basis material because it has been marketed for the past 25 years as a low cost polymer fibre. In the present day it is the most commonly used polymer for making plastic optical fibres [6.6]. Generally, it is lighter, with higher flexibility even at large core sizes. Its elastic limit is an order of magnitude higher in comparison to silica and can be strained more than 30% without breaking. The measure of its stiffness expressed by the Young's modulus is in the range of 2.5-3.3 GPa for PMMA, while for silica it is around 72 GPa [6.7,6.8]. PMMA is stable up to 85°C in normal conditions, with a glass transition temperature around 100°C. Further increase of the processing temperature can lead to rapid degradation, and at the temperatures exceeding 215°C, the polymer decomposes back into monomer [6.8]. Fibre-grade PMMA does not produce dangerous shards, and organic materials can be incorporated during fabrication without decomposition due to the low processing temperatures. The low glass transition temperature of PMMA means that fibre drawing can be done at temperatures between 170 °C and 200 °C [6.7].

6.2.1. Free radical polymerization

The simple procedure of radical polymerization of methyl methacrylate is used for preparing a high quality poly methyl methacrylate preform [6.9]. The resulting PMMA needs to be free of various imperfections and air bubbles. Those could cause undesirable light scattering and make the drawing process impossible. Additionally, the molecular weight of the polymer needs to be kept within a certain range. It has to be high enough that the optical elements are not brittle, but not too high to prevent the polymer to be drawn into a fibre. This weight has to be achieved by the addition of a chain transfer agent during the polymerization, which in case of this thesis was butanethiol [6.9]. PMMA is made of methyl methacrylate (MMA), the monomer molecular unit of MMA is shown in Fig. 6.8.

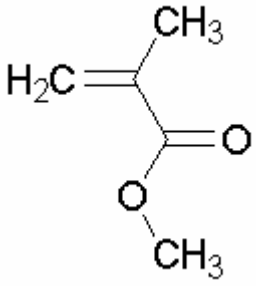

Figure. 6.8 - Schematic drawing of the MMA.

The method of polymerization of the MMA used during this thesis is free radical polymerization [6.9], which is a type of chain-growth polymerization. In this reaction the whole process is initiated by a radical in which a large number of monomer units are added rapidly until the termination of the reaction. This allows the formation of a polymer with a high molecular weight rapidly. The main stages of the chain growth polymerization are initiation, propagation and termination [6.9].

The first stage in this process is the formation of a radical from a initiator. In this thesis, in the free radical polymerization, the initiator is an unstable organic molecule that decomposes into free radicals when subjected to heat. Other possibilities are decomposition due to radiation or redox reaction [6.9]. Heat decomposition was chosen as it was the safest and easiest to control in our laboratory environment. The chosen initiator was benzoyl peroxide (BPO) [6.9], with decomposition temperature, around 70°C (Fig.6.9).

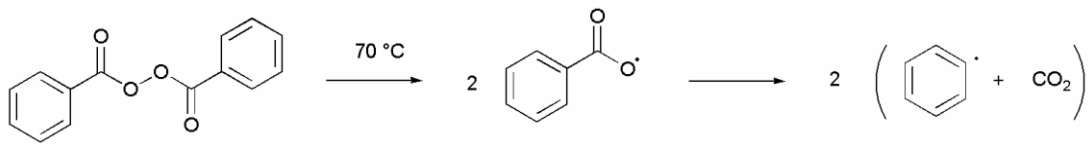

Figure. 6.9 - Mechanism of the decomposition of the benzoyl peroxide.

During the second part of the initiation process, the radical (made by decomposition of benzoyl peroxide) reacts with one of the monomer molecules [6.9]. In this process an activated monomer (or chain carrier) is created, which can rapidly react with other monomer molecules in the test tube (Fig. 6.10).

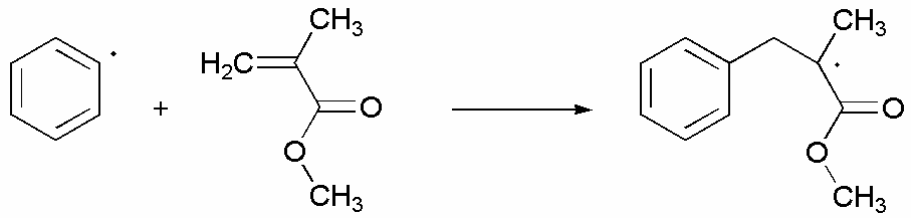

Figure. 6.10 - Mechanism of the initiation step between BPO and MMA.

At this point the second stage of the polymerisation reaction called the propagation starts. By reacting with further monomer units a polymer chain is formed [6.9]. During the reaction, the active centre propagates along the polymer chain at a rate of up to several thousand additions within a few seconds (Fig. 6.11).

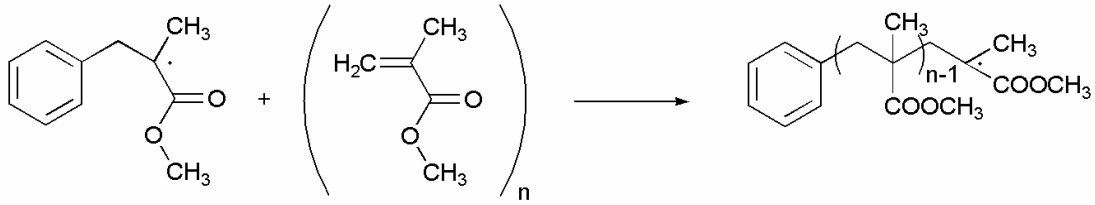

Figure. 6.11 - Mechanism of the propagation step.

The last stage of the polymer growth is the termination stage. There are two method of termination of the chain polymerization [6.9]. First of those is achieved by combination, where two radicals species react with each other forming a single polymer molecule, giving two saturated polymer chains. This termination method is common in the polymerizations carried out in the presence of the chain transfer agent (CTA) (Fig. 6.12).

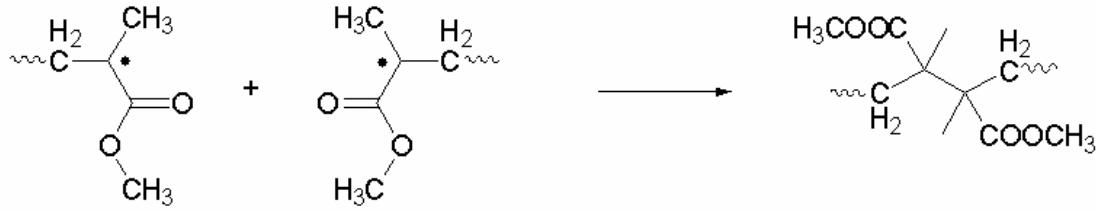

Figure.6.12 - Mechanism of the termination step by combination.

The second method of termination, consist of two radicals meeting, but instead of coupling, they exchange a hydrogen atom, this results in two terminated chains, one with a terminal double bond and another which is saturated [6.9]. This method is more common in the polymerizations carried out without CTA and the unsaturated polymer chain has greater tendency to depolymerise, which is detrimental to the further drawing processes (Fig. 6.13).

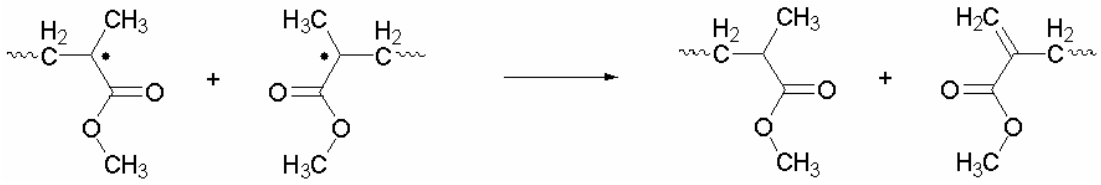

Figure 6.13 - Mechanism of the termination step by disproportionation.

6.2.2. Development of fibre-grade poly methyl methacrylate

In order to develop fibre-grade PMMA utilizing free radical polymerisation, the three reactants placed in the test tubes were: the monomer (MMA), a chain transfer agent (butanethiol) and an initiator (benzoyl peroxide) (Fig. 6.14) [6.9].

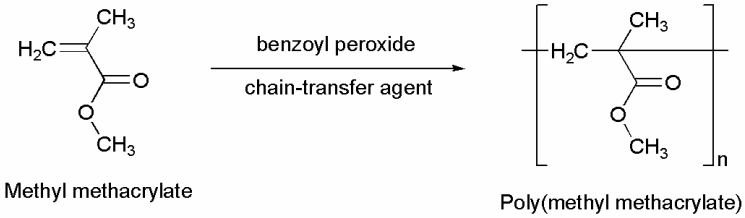

Figure 6.14 - Procedure for making PMMA.

Before any polymerization could occur MMA, which was supplied with an inhibitor (10-100 ppm monomethyl ether hydroquinone) had to be cleaned. To remove the inhibitor, the stabilized MMA was washed with an aqueous NaOH solution (2 M, 50 vol%) and water (50 vol%). The inhibitor free monomer was then dried by using MgSO4, filtered and degassed with the help of a vacuum pump. After preparing MMA for further use it was mixed with the rest of the reactants.

In order to ensure that there was no oxygen left in test tube before each polymerization, nitrogen gas was passed through the solution and the test tube was sealed with a septum cap. It was then placed in an oil bath. The specific temperature and amount of time used were determined by the ratios of the chemical compounds used in the process. Depending on the experiment the whole process took between 72 hours to 7 days of heating the solution to complete. In order to facilitate the fastest possible heat exchange between the polymer sample and the oil bath, polymerizations were carried out in test tubes with the best possible ratio of surface area to internal volume. This was done because the polymerization process is highly exothermic and the possibility of exceeding boiling point of monomer (100°C) was a real concern during this whole series of experiments (Fig. 6.15).

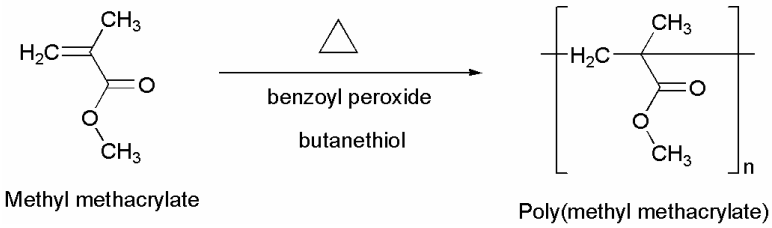

Figure 6.15 - Equation of the reaction.

Initially, small samples were made, with the aim of establishing the control parameters of the process and to get the best result before moving to large scale samples. Large scale samples were needed to test their optical properties and to draw them into an optical fibre. The aim of this part of the thesis was to develop a procedure for preparing high quality optical PMMA. The optimization of the samples was performed step by step: starting from the transparency, then the amount of monomer left and the uniformity of the preform. The resultant polymer sample should be a clear solid (Fig. 6.16).

Figure 6.16 - Clear polymer sample.

The challenge with PMMA polymerization lies in balancing the concentrations of initiator, chain transfer agent and process temperature. The amount of the initiator used is directly related to the amount of MMA. Too low a concentration will result in monomer remaining in the finished product. This has disastrous effects on the polymer during fibre drawing. The temperature of the drawing process varies from 180 to 195°C, this is below the temperature at which PMMA starts to depolymerise (this process starts at 215°C) [6.9]. The temperature at which monomer starts to boil is 100°C, which means that if there is any monomer left in the drawn sample, it will boil and produce gas bubbles disrupting the drawing process. If the concentration of the initiator is too high, some of the initiator will be left in the polymer sample (Fig.6.17), which will result in a non-uniform composition of the sample. This results in instabilities in the fibre diameter during the drawing process and increases the probability of breaks in the drawn fibre.

The amount of chain transfer agent governs the length of the polymer chains of the produced PMMA.

Figure 6.17 - Excess initiator in the air bubble.

The temperature during the whole polymerization process cannot exceed 100°C, as it is boiling temperature for the monomer. The polymerization process is highly exothermic, which can easily lead to temperatures in excess of this limit [6.9]. The amount of CTA used can mitigate the temperature increase during polymerization, allowing for longer and less energetic polymerization. This also allows gasses remaining in the test tube to escape before sample solidification. If the polymerization in the initial stage (while the sample is still liquid) is too fast, the remaining gases are trapped inside forming large air bubbles, which means that either the initiator decomposed too quickly (for processes without CTA this can occur even at low temperatures such as 60 °C), or there was too much air left in the solution (Fig. 6.18).

Figure 6.18 - Result of the too fast and too exothermic polymerization.

The first successful polymerization, which produced solid clear PMMA sample, was a 3-day process with constant temperature at 80°C. The sample consisted of 10mL of

monomer, 0.03 mol of initiator (benzoyl peroxide) and 0.06 mol of CTA (butanethiol). Before the heating started nitrogen was passed through the solution for 20 minutes. The resulting polymer was a clear solid (fig 6.19).

Figure 6.19 - First solid and clear PMMA sample. High amount of gas bubbles is visible.

During the optimization process the foremost challenge lay in removing all the gas bubbles from the sample and ensuring that no new gas bubbles were formed during drawing process. This can be minimised in the initial step of the polymerisation by matching the amounts of chain transfer agent and initiator introduced to the MMA (Table 6.4)

MMA (ml)	CTA (%)	Initiator (%)	
5	3,50	19,36	sample is clear, but brittle, shattered with test tube
5	4,30	19,36	sample is clear, but brittle, shattered with test tube
5	3,82	19,36	sample is clear, but brittle, shattered with test tube
5	6,46	24,22	initiator didn't completely mix with MMA, remains as white residue at the bottom of the test tube
5	8,62	24,22	initiator didn't completely mix with MMA, remains as white residue at the bottom of the test tube
5	3,50	9,68	sample is clear, but brittle, shattered with test tube
5	1,74	9,68	sample is clear, but brittle, didn't shatter with test tube
5	1,74	14,52	initiator didn't completely mix with MMA, a little remains as white residue at the bottom of the test tube
5	0,88	12,10	sample is clear, initiator didn't completely mix with MMA, remains as white residue at the bottom of the test tube
5	0,88	10,88	sample is clear, subsequent large scale (15 ml) processes with this amount of CTA and initiator not successful
15	0,44	10,88	sample boiled during first 24h (55 degrees), initiator didn't completely mix with MMA, remains as white residue at the bottom of the test tube
20	0,80	6,00	No initiator concentration, but sample less clear, one clean break during test tube removal
20	0,85	5,00	No initiator concentration, some brakes at the end of the sample
20	0,85	4,00	No initiator concentration, one clean break during test tube removal
20	0,88	3,50	No initiator concentration, one clean break during test tube removal, Tg 83.7, 86.9
20	0,88	3,00	No initiator concentration, clean breaks during test tube removal, Tg 58.5, 61.7

Table 6.4 - MMA, initiator and CTA concentrations and their influence on the final PMMA material. Each of the polymerisation processes was conducted over 5 days.

Table 6.4 shows how concentrations of initiator, MMA and CTA influence the final result of the polymerisation. Clear, bubble free PMMA was achieved for CTA concentration of 0.88% and for initiator concentration of 3% and 3.5%. ^{1}H-NMR spectral analysis has been made in order to check the amount of monomer left in the polymer samples. The theory behind NMR is based on the measurement of the spin of a nucleus. ^{1}H nuclei measured in ^{1}H-NMR have the sum of protons and neutrons equal to an odd number, which corresponds to half-integer spin. When the external magnetic field is applied, the spins of the nuclei orient themselves with or against the applied field. The spin state that is parallel (α) to the applied field and has lower energy than the spin state that is antiparallel (β) to the applied field. The energy difference (ΔE) between the α and β-spin states increases with the increase of the external field. The emitted energy produces an NMR signal. The position on the horizontal frequency scale at which the equivalent proton signals occur (ΔE – the position of the peak at the scale) is called a chemical shift, which is measured in ppm [6.10]. The ^{1}H-NMR spectral analysis was performed by Adrien Maniquet at the Heriot-Watt University.

In fig 6.20 and 6.21 one can see two examples of the results of this analysis. In 6.20, one of the initial samples with a high monomer concentration and in 6.21, a sample with a low amount of monomer left in the polymer.

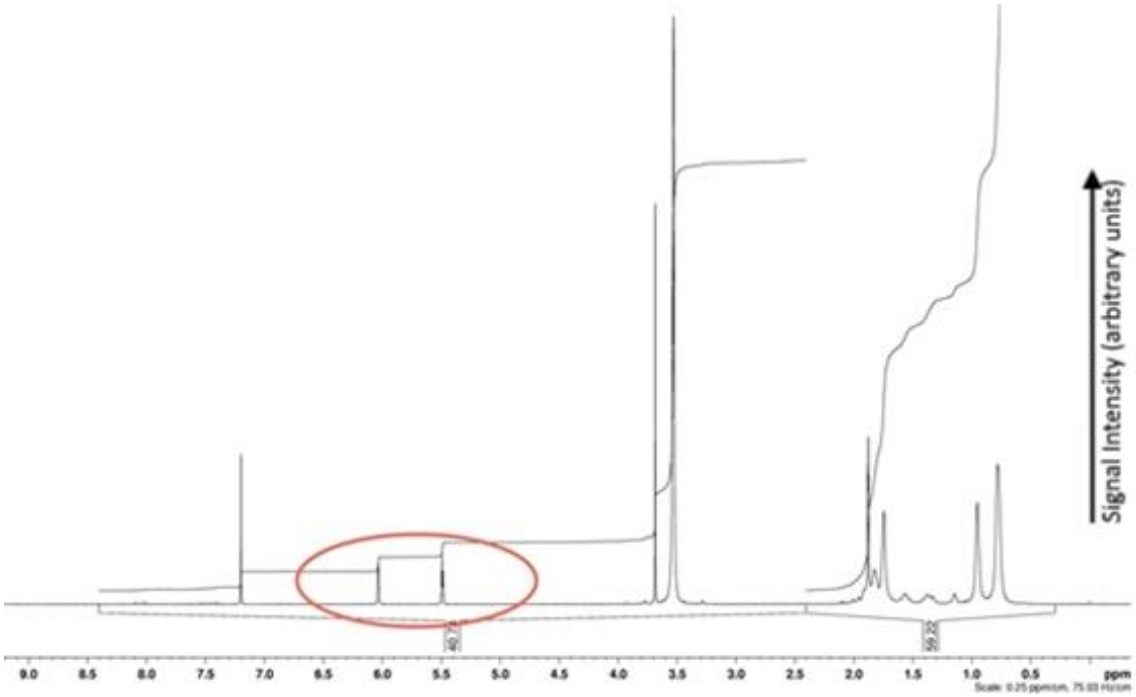

Figure. 6.20 - Polymer spectrum with a high amount of monomer.

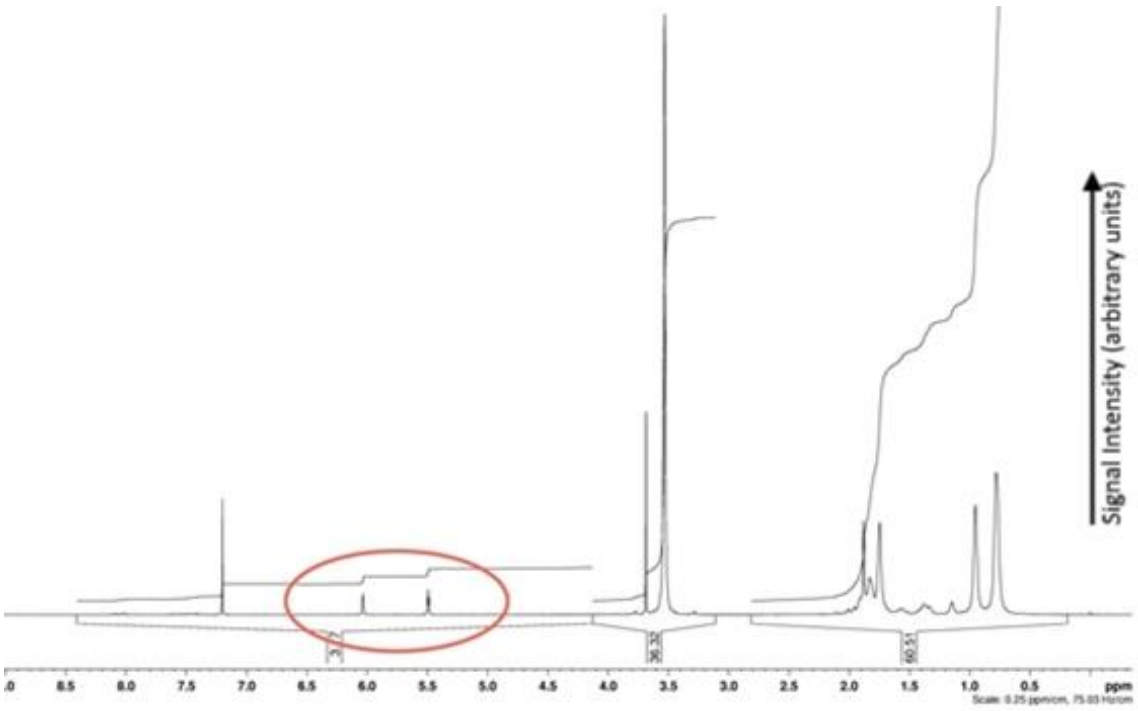

Figure. 6.21 - Polymer spectrum with a low amount of monomer.

The MMA molecule has an H_2C group attached to the molecule by the double bond. On the MMA spectra (fig. 6.22) it can be seen at 6 and 5.5 ppm. In the PMMA chain this double bond is transformed into two single bonds holding next and previous MMA molecule in the polymer chain. Lack of this double bond is the distinguishing feature between MMA and PMMA, as the rest of the hydrogen nuclei does not change their position in the molecule. In the fig. 6.21 the peaks marked by red circle are smaller, indicating less double bonds in the tested sample – meaning less MMA molecules.

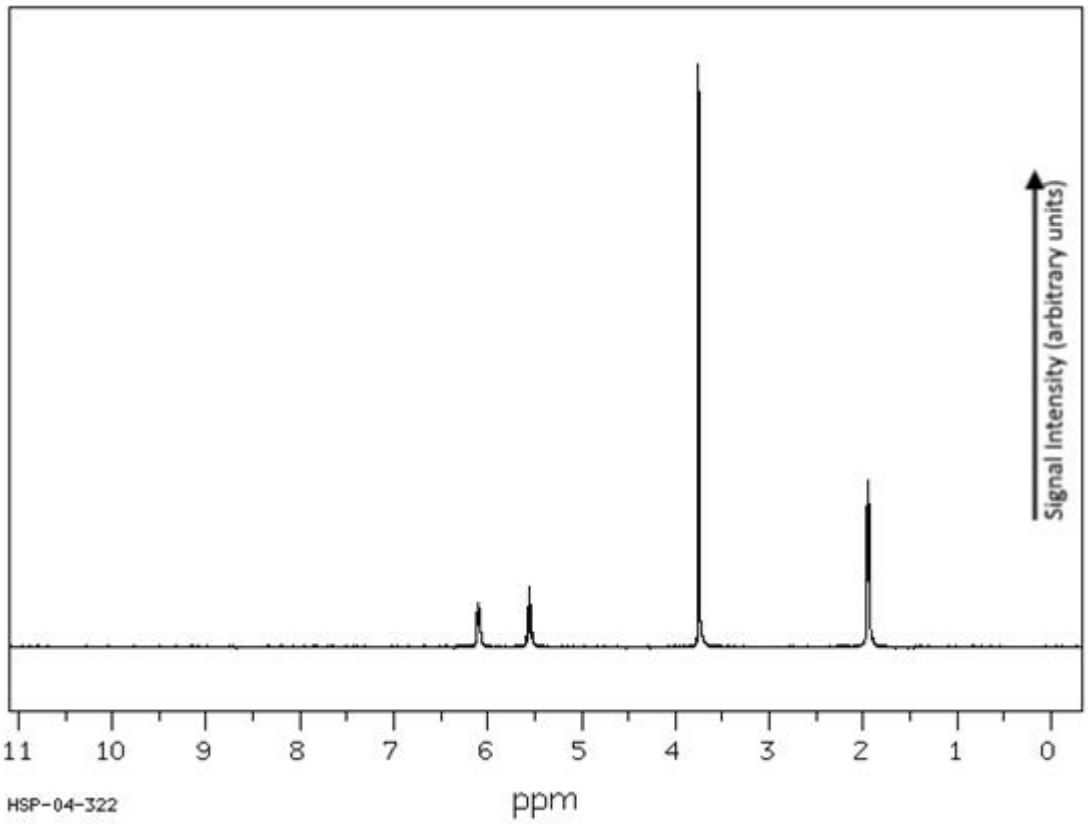

Figure. 6.22 – Clean MMA molecule spectrum [6.11].

The glass transition temperatures of the polymers (T_g) were analysed using Differential Scanning Calorimetry. The initial sample had the temperature T_g=64°C. The literature value of T_g for pure PMMA is given as 100°C. The amount of the impurities left in the polymer can explain the difference of those temperatures. This is further substantiated by the fact that the most recent samples of the manufactured PMMA, the sample with 3.5% of initiator and 0.88% of chain transfer agent, had the highest transition temperature T_g,=86.9°C. This is a significant decrease in the monomer concentration over the initial samples. This temperature was also closest to the commercially available samples. The resultant sample was than drawn in the fibre drawing tower. This test showed that new gas bubbles were still forming in the polymer during drawing and disrupting the process.

The solution to that was modification of the polymerization setup, ensuring better vacuum and thus greater gas removal during polymerisation process. To ensure that gasses produced during first stages of polymerization could escape the mixture the whole polymerisation process was slowed down and temperature was incrementally increased during polymerization over several days. This way gasses from the inside of the sample could escape before the PMMA solidified. Polymerization is also highly exothermic with

the highest temperature increase at the beginning of the process, so a low initial temperature helps to avoid exceeding the MMA boil temperature.

In the initial polymerisations, butanethiol, benzoyl peroxide and monomer were mixed for 5 minutes. Next for half an hour while the liquid was constantly mixed nitrogen was passed through it. This was done to ensure that there was as little oxygen left as possible and that the liquid was uniform. After that the liquid was poured into test tubes. As pouring liquid into test tubes introduces a lot of gas into it, it was done at the earliest possible stage of the polymerization process. After that the test tubes were placed in a vacuum cupboard for 15 minutes. After that time, when most of the oxygen left the liquid, nitrogen was again introduced to the liquid in order to displace any remaining oxygen. This process was repeated for 2 hours. After that the test tubes were placed in an oil bath at a temperature of 40°C. Every 12 hours the temperature of the oil bath was increased, at first by 5°C until it reached 50°C, then by 10°C until it reached 70°C. After reaching this temperature the oil bath was held at a constant temperature for 48 hours. The samples obtained using this method were clear (Fig.6.16) and could be drawn in the fibre drawing tower. Each drawing would increase detrimental effects of any impurities left in the PMMA sample.

The optical transmission of the best polymer samples was checked. For the second (1310 nm) window, the transmission equals 90%, and for the third window (1530 nm), the transmission equals 88% (Fig. 6.23).

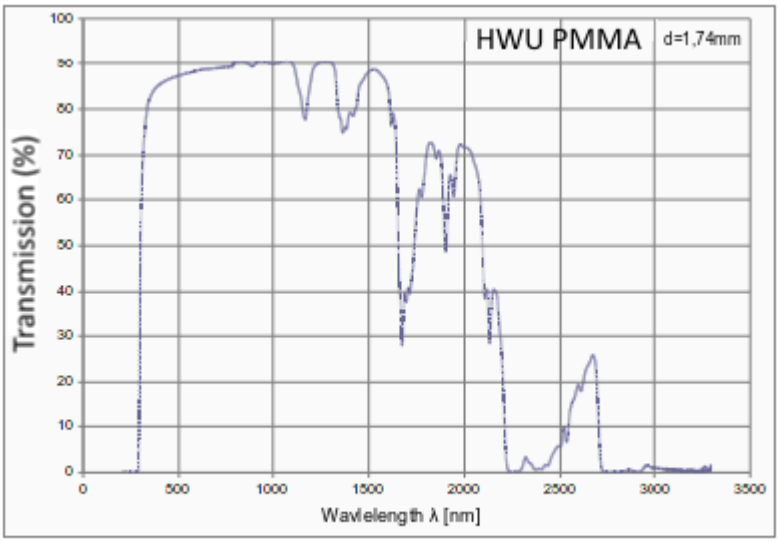

Figure 6.23 - Transmission spectrum of one of the polymer samples.

This is comparable with commercially available PMMA materials, which have transmission around 90% (depending on the manufacturer) for 500 to 1100 nm wavelengths [6.12, 6.13] (fig. 6.24)

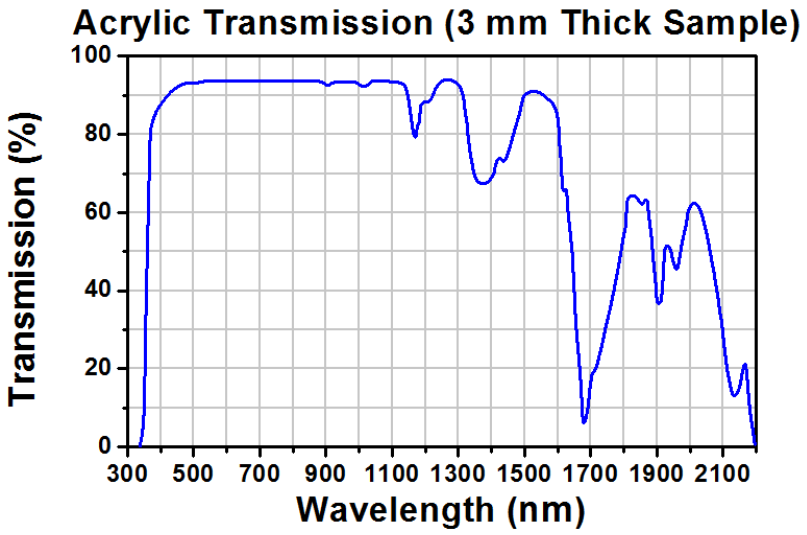

Figure 6.24. PMMA transmission for Thorlabs plastic lenses [6.13].

6.2.3. Development of doped PMMA

In order to create dual polymer structures a second polymer with different refractive index is needed. To ensure similar thermal and mechanical properties to the clear PMMA, needed for thermal processing in stack and draw method of structure fabrication, the polymerisation process described in section 6.2.1 was used as starting point for further tests. The process was modified by adding a number of different chemical compounds, thus creating doped PMMA. First tests performed with clear PMMA doped with methyl red and methylene blue showed that changes in refractive index are tied very strongly to the chemical composition. Adding 0.01% of methylene blue changes the refractive index by an amount lower than sensitivity of available equipment. At the same time, it changes transition temperature by 20°C, making it unsuitable for thermal processing with clear PMMA. Based on developments reported in [6.14, 6.15] tests were performed using benzyl benzoate (BEN). Increasing the concentration of BEN in PMMA would increase the refractive index of the doped PMMA and at the same time change transition temperature. The largest concentration of BEN that allowed joint thermal processing of clear and doped PMMA is 5%. The resultant doped PMMA was used to fabricate the dual polymer fibre described in section 6.3.2.

6.3. Polymer optical fibre

In the course of the research, preliminary tests of polymer based photonic structures were performed. The first series of these tests was to evaluate the stack & draw method for drawing polymer structures. Those test were performed simultaneously with in-house polymer development and commercially available PMMA was used. The test structure was a simple air-polymer photonic fibre.

The second test series was performed with the two in-house developed polymers. The structure was fabricated using two separate polymer materials, clear PMMA and BEN doped PMMA. The goal of these tests was to ascertain the viability of using the stack and draw method for two polymer structures. The test structure was a simple optical fibre.

6.3.1. PCF PMMA fibre

For fabrication of the photonic crystal fibre, commercially available PMMA was used because of the lack of in-house produced PMMA. The capillaries and rods were drawn in a fibre tower at a temperature of 180-200^{o}C from the capillaries with a diameter of 1.95 mm. The capillaries are ordered in a hexagonal lattice with 7 elements on the diagonal. By replacing a single PMMA tube with a rod in the centre of the lattice the core is created. The replacement rod has similar diameter as the capillaries, equal to 1.95 mm. The entire structure was placed inside a single PMMA tube with a diameter of 20 mm.

The standard method for fabrication of polymer crystal fibre is drawing of a preform with drilled holes [6.16,6.17]. In this thesis we utilised the much more versatile stack-and-draw technique [6.18,6.19], which is further explained in Chapter 6, for the PMMA fibre development. A fibre drawing facility optimised for soft glass fibre fabrication was used. Polymer tubes with a 20mm external diameter were scaled down to 1.5 - 2.5mm diameter capillaries. Drawing temperature was set to 180^{o}C. Those were then placed according to the structure schematic inside a 20mm polymer tube. Drawing temperature was set to 190^{o}C. During those test it became apparent that there are differences between drawing polymer and glass fibres. First and foremost is the difference in drawing temperatures. While most soft glass structures are drawn at temperatures exceeding 600^{o}C, polymers are drawn at temperatures below 200^{o}C. This means that the temperature range in which both materials of the structure can be drawn is significantly smaller for polymers. Because of that, PMMA based materials must be closer matched to each other than standard glasses. Secondly during first drawing all of the polymer chains in the structure are tangled together, thus polymer internal structure is closer to amorphous solid, like

glass. During drawing all of the chains are straightened resulting in an overall directionality along the drawing axis. This means that in second (and subsequent) drawings the polymer behaves differently. The third and most important difference is the fact that all of the impurities left from polymerisation start to disrupt the drawing process. Remaining monomer starts to boil in temperature above 100 $^{\circ}C$, which is below drawing temperature, introducing gas bubbles to the structure. This means that with each drawing the overall quality of the polymer degrades. In our initial test only two subsequent drawings of the same PMMA sample were possible (Fig. 6.24). During the third drawing the PMMA sample started to break before it could be drawn.

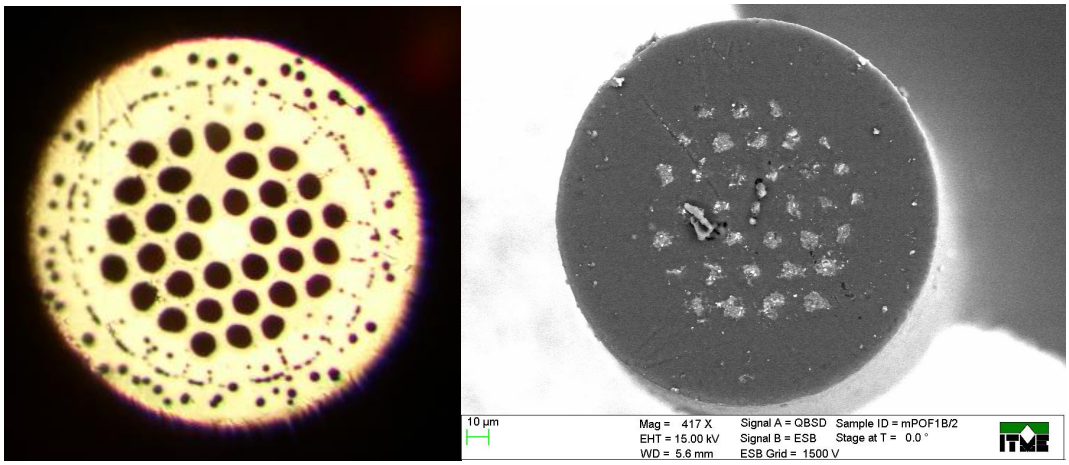

(a) (b)

Figure 6.24 - Optical microscope (a) and SEM (b) photos of developed PMMA based structured polymer optical fibre. An air holes in SEM sample are contaminated with polishing powder.

The measurements of the fibre show that the average diameter of the air holes is about 22µm, while the pitch is 38µm. The circular core of the fibre has a diameter of 52µm, while the total diameter of the fibre is 450µm. One of the capillaries collapsed during drawing which resulted in the deformity of the hexagonal lattice of the photonic cladding. Computer modelling of the optical properties of the structured fibre, using a finite difference method, based on the SEM pictures show that, the fibre is effectively a single mode fibre. According to simulation the considered fibre structure has a single mode, which is 1351µm^2, for an effective refractive index of 1.490 and attenuation of 1.89×10^{-4} dB/m for a wavelength of 650nm, when material losses not considered. Although two higher modes are also guided in the structure their attenuation is 4 orders of magnitude higher.

6.3.2. All-solid polymer optical fibre

The second series of tests was conducted using the in-house fabricated clear and doped PMMA described in sections 4.2.2 and 4.2.3 respectively. The test structure is a fibre consisting of clear PMMA core and doped PMMA cladding. The diameter of the whole fibre is approximately 2mm, while the cladding has approximately 1.2mm (Fig. 6.25)

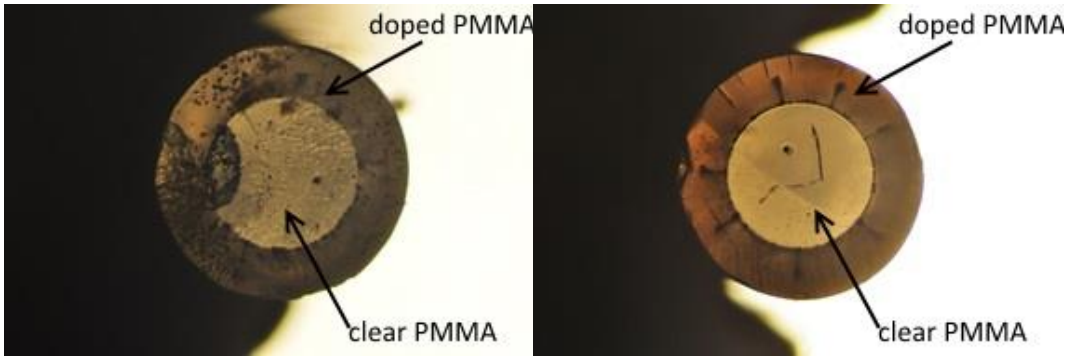

(a) (b)

Figure 6.25 - Optical microscope pictures of the fabricated fibres. (a) – fibre diameter 2mm, core diameter 1.2mm, (b) – fibre diameter 1.95mm, core diameter 1.2mm.

The test drawing was successful, both polymer integrated with each other and formed a single dual polymer structure. In Figure 6.26 one can see imperfections on the border between the two polymers. Those are a result not of the faults during drawing, but air pockets trapped between polymers. Those are introduced by the faults of the polishing of the inside of the outer polymer tube. This results in a very high attenuation of this fibre. The attenuation for the 1.95mm fibre is 27dB/m, while attenuation for the 2mm fibre equals to 30 dB/m at 658nm. The losses in those fibres are significant, especially when compared to the commercially available PMMA fibres, which have losses in range of 1dB/m at 658nm [6.20], or even 22-40 dB/km at 850-1300nm for fibre made from CYTOP [6.21]. This is not a problem as optical elements that would be fabricated using these materials are no longer then 200 – 300μm.

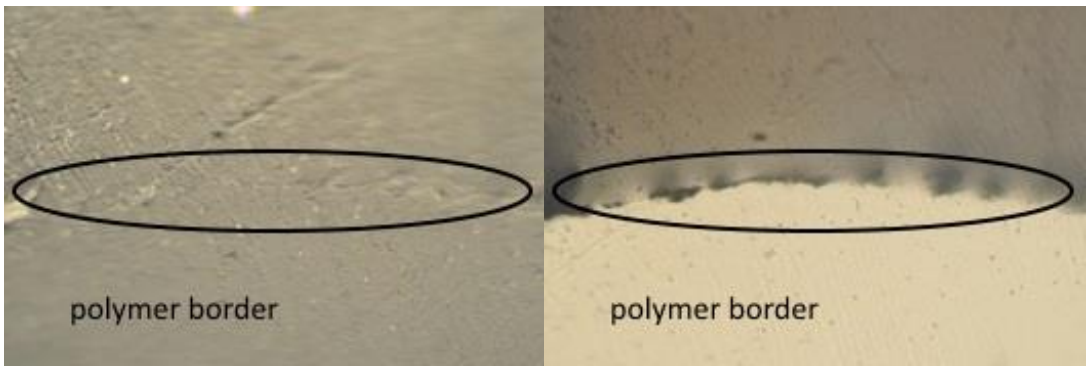

(a) (b)

Figure 6.26 - Optical microscope pictures of the border area between two polymers used. (a) border area in the reflected light (b) the same area in the propagating light.

6.4. Conclusions

Two pairs of glasses were analysed for suitability for nanostructured fabrication Both the F2/NC21 and NC21/NC34 glass pairs provided a small enough refractive index difference, 0.85 and 0.333 respectively. Both glass pairs have similar transition temperatures and expansion coefficients that allow them to be processed together in the drawing tower using the stack and draw method. The NC21/NC34 pair of glasses have an expansion coefficient difference $\Delta\alpha=0.4\times10^{-7}$ K^{-1} while the F2/NC21 pair which has expansion coefficient difference $\Delta\alpha=5.3\times10^{-7}$ K^{-1}. For NC21/NC34 the difference in the curvature temperature is $\Delta T_c=50^oC$ and difference in the sphere temperature is $\Delta T_{kpb}=35^oC$. The F2/NC21 pair of glasses has $\Delta T_c=100^oC$ and $\Delta T_{kpb}=35^oC$. Those parameters allow both glass pairs to be safely jointly processed in the drawing tower.

An in-house synthesis process for the production of optical grade PMMA has been developed. While the basics of MMA polymerisation are well known, the exact process of obtaining optical grade PMMA that can be used after multiple thermal processes is kept a secret by manufacturing companies. By the end of the work on PMMA in this thesis the developed material was clear with transmission reaching 90%. Our knowledge of the exact chemical composition of the polymer allowed the creation of doped PMMA with similar thermal and mechanical properties. Samples of BEN doped PMMA with a refractive index different from the clear PMMA were fabricated.

Initial tests showed the feasibility of using PMMA in the stack and draw method, during which PMMA can be subjected to multiple thermal processes. Further tests show that it is possible to jointly process thermally two separate polymers using the available

equipment. Both of these tests show the possibility of using two distinct PMMA materials with customised refractive indices for creating various photonic and micro structures utilising the stack and draw method. Some initial results can be found in the literature using commercially available polymers (Zanex and clear PMMA) and a simplified version of stack and draw method. The method outlined in this chapter, because of the utilisation of the full stack and draw method, allows the use of longer preforms and the in-house fabrication of polymers allows greater control of their optical and thermal parameters. After achieving this milestone, it was decided to switch from PMMA materials to glasses for further development of the optical structures. The decision was dictated by the fact that optimisation of a matching pair of polymer that could be used in the stack and draw method and fabrication of optical elements out of it would exceed the time allotted for the PhD work.

6.5. References

[6.1] I. Kujawa, A. Filipkowski, D. Pysz, F. Hudelist, A. Waddie, R. Stepien, R. Buczynski, M. Taghizadeh, *Photonic glass: novel method for fabrication of volume 2D photonic crystals*, Optical Fibers and Their Applications, 7120 (2008)

[6.2] R. Buczynski, J. Pniewski, D. Pysz, R. Stepien, R. Kasztelanic, I. Kujawa, A. Filipkowski, A. J. Waddie, M. R. Taghizadeh, *Dispersion management in soft glass all-solid photonic crystal fibres*, Opto-Electronics Review, 20(3), 207-215 (2012)

[6.3] R .Buczynski, I. Kujawa, A. Filipkowski, D. Pysz, F. Hudelist, A. Waddie, R. Stepien, M. Taghizadeh, *Novel method for fabrication of volume 2D photonic crystals*, Photonic Crystal Materials and Devices VIII, 6989 (2008)

[6.4] D. Pysz, I. Kujawa, R. Stępień, M. Klimczak, A. Filipkowski, M. Franczyk, L. Kociszewski, J. Buźniak, K. Haraśny, R.Buczyński, *Stack and draw fabrication of soft glass microstructured fiber optics*, Bulletin of the Polish Academy of Sciences Technical Sciences, 62(4), 667–682 (2014)

[6.5] A. Filipkowski, R. Buczyński, A. J. Waddie, I. Kujawa, D. Pysz, M. R. Taghizadeh, R. Stępień, *Superprism effect in all-glass volumetric photonic crystals*, Opto-Electronics Review, 20(3), 267-274 (2012)

[6.6] W. Daum, J. Krauser, P.E. Zamzow, O. Ziemann, *POF - Polymer Optical Fibers for Data Communication*, ISBN: 978-3-662-04863-4, New York: Springer-Verlag (2002)

[6.7] M.C.J. Large, A. Argyros, *Impact of polymer material properties on microstructured optical fibers*, Frontiers of Optoelectronics in China, 3(1), 99-102 (2010)

[6.8] P. G. Lye, M. Boerkamp, A. Ernest, D. W. Lamb, *Investigating the sensitivity of PMMA optical fibres for use as an evanescent field absorption sensor in aqueous solutions*, Journal of Physics: Conference Series, 15, 262-269 (2005)

[6.9] A. Maniquet, *Optical fibre-grade poly(methyl methacrylate)*, Thesis collection, Heriot Watt University (2011)

[6.10] T. L. James, *Fundamentals of NMR*, Textbook, Department of Pharmaceutical Chemistry University of California (1998)

[6.11] Spectral Database for Organic Compounds, http://sdbs.db.aist.go.jp/, Research Institute for Material and Chemical Measurement National Institute of Advanced Industrial Science and Technology (AIST), Japan (2016)

[6.12] Plastic moulded lens, https://www.thorlabs.de/newgrouppage9.cfm?objectgroup_id=16, Thorlabs Inc, Newton, New Jersey, USA (2016)

[6.13] *Plexiglas by Arkema Optical & Transmission Characteristics,* http://www.plexiglas.com/export/sites/plexiglas/.content/medias/downloads/sheet-docs/plexiglas-optical-and-transmission-characteristics.pdf, Altuglas International, Bristol, Pennsylvania, USA (2016)

[6.14] T. Ishigure, M. Satoh, O. Takanashi, E. Nihei, T. Nyu, *Formation of the Refractive Index Profile in the Graded Index Polymer Optical Fiber for Gigabit Data Transmission*, Journal of Lightwave Technology, 15(11) (1997)

[6.15] M. Sato, T. Ishigure, Y. Koike, *Thermally Stable High-Bandwidth Graded-Index Polymer Optical Fiber*, Journal of Lightwave Technology, 18(7) (2000)

[6.16] C. Ponseca, R. Pobre, E. Estacio, N. Sarukura, A. Argyros, M. Large, M. v. Eijkelenborg, *Transmission of terahertz radiation using a microstructured polymer optical fiber*, Optics Letters, 33(9), 902-904 (2008)

[6.17] K. Nielsen, H. Rasmussen, A.L. Adam, P.M. Planken, O. Bang, P. Jepsen, *Bendable, low-loss Topas fibers for the terahertz frequency range*, Optics Express, 17(10), 8592 (2009)

[6.18] M. R. Taghizadeh, A. J. Waddie, R. Buczynski, J. Nowosielski, A. Filipkowski, D. Pysz, *Nanostructured micro-optics based on a modified stack-and-draw fabrication technique,* Adv. Opt. Techn., 1(3), 171-180 (2012)

[6.19] J. M. Nowosielski, A. Filipkowski, A. J. Waddie, I. Kujawa, R. Stepien, *Diffractive optics development with stack-and-draw technique*, Proceedings of SPIE, 8428(1) (2012)

[6.20] *The FOA Reference For Fiber Optics - Optical Fiber*, http://www.thefoa.org/tech/ref/basic/fiber.html, The Fiber Optic Association, Inc., non-profit professional society of fiber optics (2016)

[6.21] *Present State-of-the-art of Plastic Optical Fiber*, Plastic Optical Fibre Trade Organization (2004)

7. FABRICATION OF GRIN OPTICAL ELEMENTS

In this Chapter the fabrication process of the various nanostructured elements used in this thesis is described. The assembly process of such preforms and the limitations of this technology are outlined (section 7.1.1) followed by a description of the drawing process and the drawing tower which is an essential piece of equipment in the fabrication process (section 7.1.2). The drawing process consists of repeated drawings of the optical structure in the drawing tower. Depending on the initial size of the preform and number of drawings in the process different sizes of the final optical element can be obtained. In the two stage drawing process, elements with final structure sizes of about 20μm diameter can be fabricated as explained in section 7.1.3. When the drawing process consists of three stages, larger structures can be obtained, e.g. the elliptical lens with an external size of 125×75μm as described in section 7.1.4. The fabricated elements can be successfully cut, ground and polished in order to create optical elements with previously designed external dimensions. The two step process described in sections 7.2.1 and 7.2.2 allows the preparation simultaneously of up to 30 elements for further integration with the fibre. Each element has a similar diameter to standard optical fibre – 125μm, and length in the range from 10μm to 200μm. Finally, the active integration process which allows attaching optical elements to the optical fibres with the ± 2μm precision is described in section 7.2.4.

7.1. Stack and draw fabrication method

GRIN elements can be made using semiconductor fabrication technologies, as these techniques allow the creation of features with dimensions ranging up from a few tens of nanometres. This scale of features is needed in order to produce effective medium materials with subwavelength feature sizes. An example of such a method is direct write electron-beam lithography combined with dry reactive-ion plasma etching [7.1 - 7.3]. For the work outlined in this thesis, the stack-and draw method [7.4,7.5] for the nGRIN micro-element fabrication was employed. The standard stack-and-draw technique is widely used for the fabrication of photonic crystal fibres (PCFs) [7.6]. The nanostructured GRIN micro-elements presented in this thesis are all-solid elements [7.7 - 7.9]. The same principle is a basis for the fabrication of the nanostructured GRIN micro-elements as for fabrication of the PCFs, however there are differences between the methods for PCF fabrication and nanostructure fabrication which increase the overall difficulty. In the fabrication process of the nanostructured elements, the final feature size of the structure is much smaller compared to a typical PCF. Another difference is the need for a relatively

small refractive index contrast between the utilised materials, as was explained in Chapter 2. Optical micro-element fabrication requires a greater number of rods (up to 10 thousand) to be stacked together in order to form an initial preform, which increases the difficulty of getting a distortion free structure considerably.

7.1.1. Preform assembly

Stacking the initial preform is the most labour intensive stage of the fabrication. These preforms are essential structures that consist of a few thousand rods, which are arranged parallel to each other. The structures for this thesis are based on a hexagonal pattern on the rods. This pattern is self-maintaining for the rods, and is most commonly used for the photonic fibre fabrication. The pattern of the structure is calculated according to the effective medium theory as explained in Chapter 3 (Fig. 7.1 and 7.2a). The rods compromising the structure are made from two distinct glasses, which have to be chosen according to the requirements explained in Chapter 5. The rods have a diameter of 0.5-1mm. Smaller diameters would be impossible to stack down, as the rods would not be rigid enough. Larger diameters rods would significantly reduce the final size of the structure, as the size of the stacked preform structure is limited by the size of the furnace in the drawing tower. Assembly of the preform, especially the initial preform, is a critical stage in the fabrication of the nanostructured GRIN micro-elements.

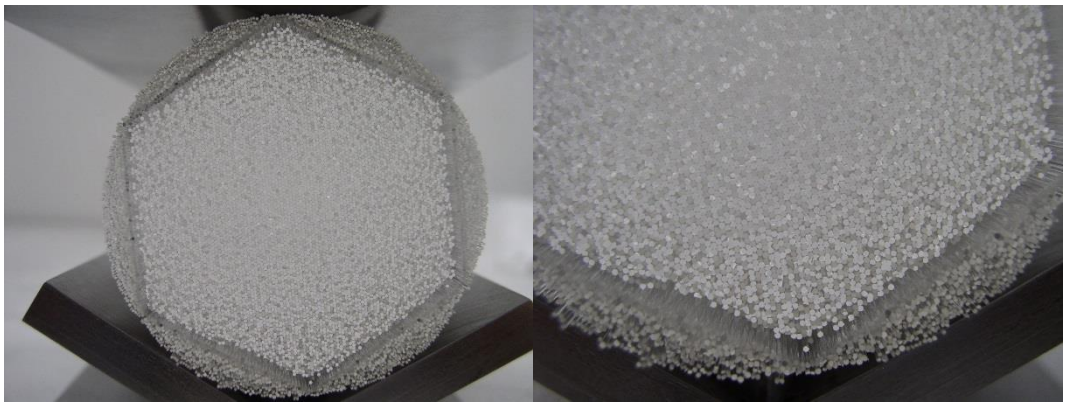

Figure 7.1 - Sample stacked preform. This preform has 100 rods on a diagonal. Different types of glasses used can be differentiated by different shade on the photograph.

One of the main challenges faced during assembly of the preform is to build a regular structure out of glass rods despite the fact that in practice these rods are not perfectly uniform and identical in terms of their diameter. It is quite common to have differences of up to 10% of the diameter between individual rods. Initial selection of the rods is utilised to remove those rods that have diameter radically different from the rest, but as usual there is a trade-off between accuracy and material waste. This is an issue during

preform assembly, as it can introduce irregularities into the structure. It does not impact the shape of the final structure. Because the structure is hexagonal all the rods remain in place during drawing, and heated glass is soft enough during to fill in the gaps. The second challenge lies in binding together and ensuring that the stacked rods do not move in relation to each other. It is possible to use a fire-proof adhesive but only at the end of the preform which is above the furnace during the drawing process. This constraint is related to the fact that there is an upward motion of heated air inside the shaft of the furnace. This could carry adhesive particles and gasses released by adhesive heating upwards inside the structure. The other end of the preform has to be bound without the use of any adhesive. Usually a metal clamp is used for this purpose. The clamp has to be well fitting in order to provide a rigid assembly.

7.1.2. Drawing process

The draw tower is an essential piece of equipment for the fabrication of the nanostructured GRIN micro-elements. A photograph of the draw tower is shown in Fig 7.2. The main part of the tower is the furnace (Fig. 7.3b) where the diameter of the drawn preform is reduced at high temperature. The preform is placed in the vertical hollow shaft inside the furnace, which can be heated up to 1000^{o}C with the furnace temperature being measured by the thermocouple. The draw tower has to provide very accurate control over the preform feed rate (Fig. 7.3a) and also the speed of the output rod pulling by the tractor assembly (Fig. 7.3c). These are the three main parameters of the drawing process. These parameters have to be carefully set in order to obtain the desired diameter of the output rod. The diameter is measured in real time by a laser micrometer (Fig. 7.3b).

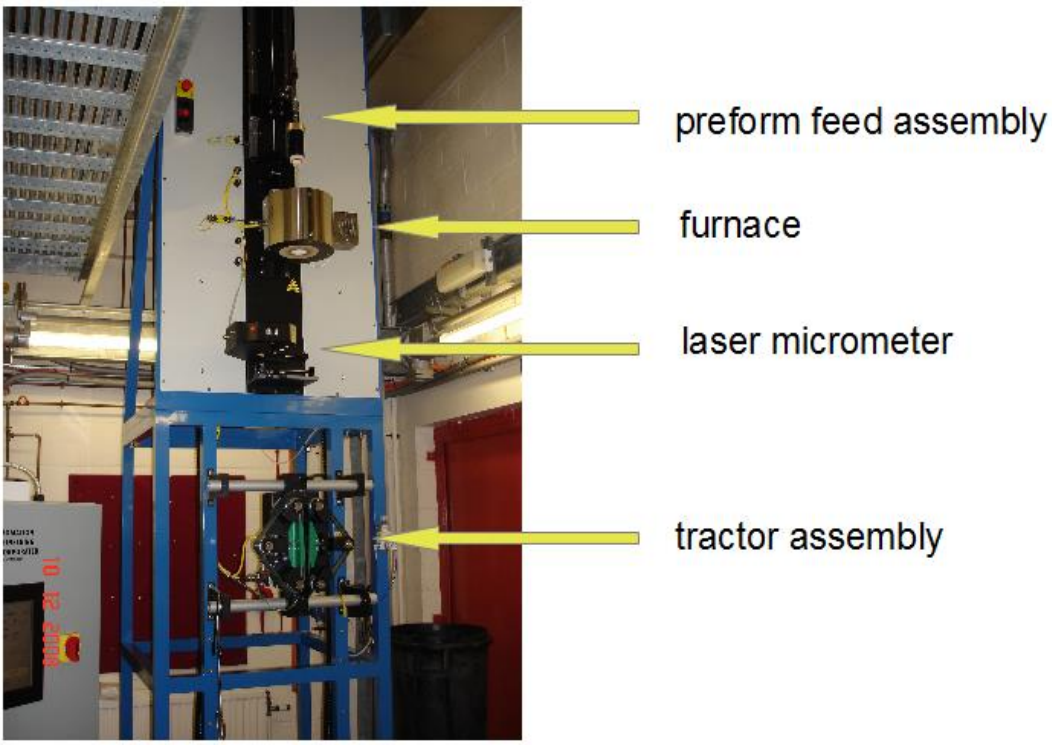

Figure 7.2 - Photograph of the draw tower at Heriot-Watt University.

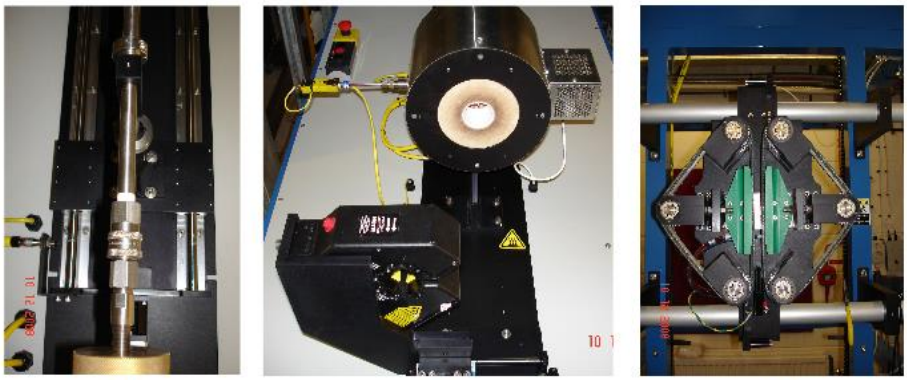

Figure 7.3 - Main parts of the draw tower. Preform feed assembly (a), furnace and laser micrometer (b) and tractor assembly (c).

The appropriate choice of the pair of glasses is a necessary condition for successful fabrication. The assembled preform (7.4a) is then drawn-down at a relatively high temperature (600^{o}C -700^{o}C) (Fig. 7.4b). Depending upon the speed of feeding and pulling of the glass the appropriate temperature is between the curvature and sphere

temperature of the glass (see Chapter 5). At those temperatures, the glass viscosity is high enough to enable drawing without breaking the glass fibre because of the speed difference of feeding and pulling. At the same time, it is low enough to preserve the pattern of the structure without significant distortions. With the temperature increase, the different glasses gradually soften to a different degree.

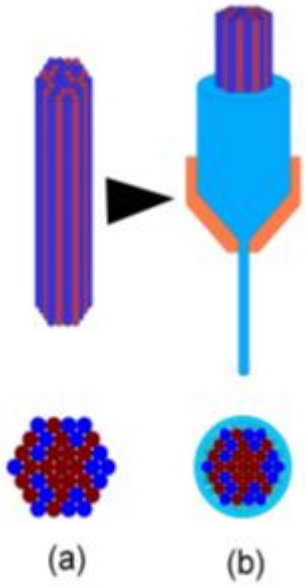

Figure 7.4 - Schematic of the procedure allowing the fabrication of nanostructured fibre.

In order for the glasses to be processed in the same distortion free structure, their viscosities have to be similar at the temperature that for both glasses falls in the range mentioned above. Proper adjustment of the furnace temperature which provides optimal viscosity in terms of sustaining a drawing process and preservation of the glass structure is a critical task during the nGRIN micro-element drawing process. As the drawing biggest drawing tower used for this thesis is 6m tall, the drawing process requires two people. For the fabrication work in this thesis, Dariusz Pysz from ITME assisted in this task.

7.1.3. Development of small optical elements

As mentioned in the section 7.1.1, the drawn structure has an outer diameter limit imposed by the furnace diameter and a minimal rod diameter that can be stacked. For the equipment used in this thesis the maximum diameter of the preform structure is 5cm, which limits the preform to 100 rods on the diagonal each with diameter of 0.5mm, resulting in almost 4000 rods in the whole structure. Each individual structure is then drawn in the drawing tower in order to reduce its diameter to about 2-3mm. Such

intermediate preforms are then packed into an external glass tube and drawn to the final diameter of the structure. This external rod provides an enclosure so that the air can be pumped out of the structure, ensuring proper bonding of the glass rods. The two glasses described in Chapter 5 were used in the fabricated structure. The higher index glass was NC34 with index n_1=1.55. The low index glass used in the structure was NC21 with the index n_2=1.5101 for the 1550nm incident light wavelength [7.10]. The drawing process, described in section 7.1.3 was used for making optical elements with an external diameter of 125μm. The precision of the diameter of the drawn entire optical elements was ± 4μm. The diameter of the structure equals to 16% of the diameter of the entire fibre, so the precision of the fabrication of the structure was ±0.64μm. The final fabricated structure of the fabricated lens and axicon was verified with a scanning electron microscope (Fig. 7.5 and Fig. 7.6).

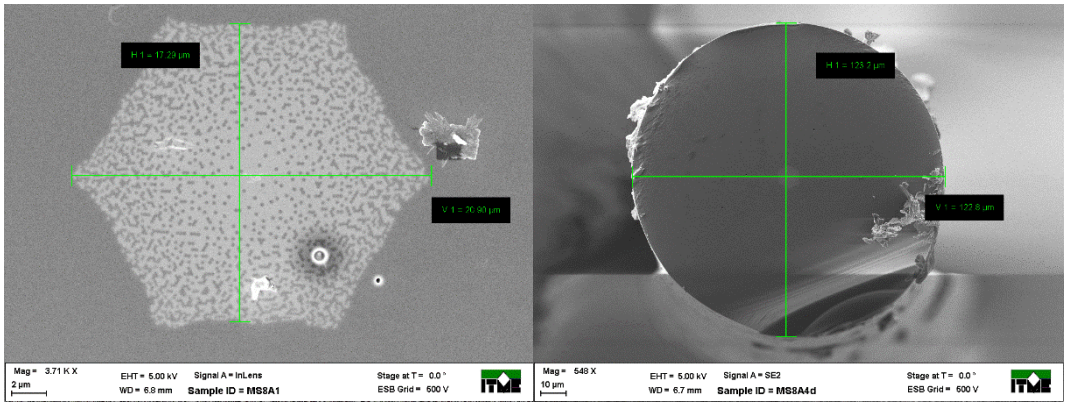

(a) (b)

Figure 7.5 - SEM pictures of fabricated nanostructured axicon. (a) Close-up of the structure, (b) cross-section of the entire element.

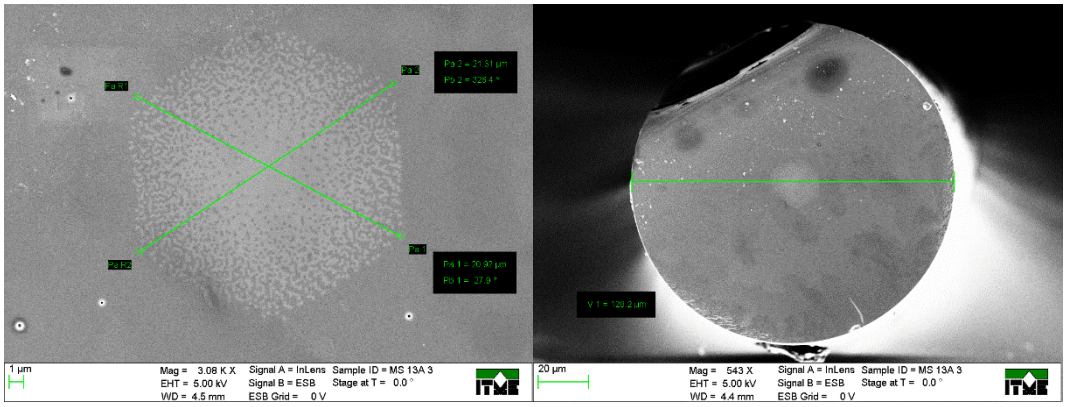

Figure 7.6 - SEM pictures of fabricated nanostructured lens. (a) Close-up of the structure, (b) cross-section of the entire element.

A clear image of the individual glass rods can be seen in both instances. The diameter of the fabricated lens is around 21μm while the whole diameter of the optical element is 128μm. For the axicon the size of the structure was also around 21μm with the diameter of the whole element being 123μm.

7.1.4. Development of large elliptical lens

As explained in previous section there is a limit on the number of rods that can be used in a single stacked structure. This current technological limit can be overcome using a hybrid approach where the nanostructured concept is combined with discrete step lens development. With this method, a parabolic spherical lens with a diameter of 100μm was fabricated [7.10]. For this thesis a similar approach was used to develop large-diameter elliptical GRIN lenses.

The fabricated lenses had seven distinct refractive index steps. Finding seven different glasses with various refractive indexes that can be processed together in fibre drawing tower is difficult, therefore five types of 'metarod' composed of different combinations of the two basic glasses (NC21 and F2) were made. Five of the seven rods were fabricated using the two fundamental glasses NC21 and F2 according to a pre-calculated pattern to ensure a uniform effective refractive index within every nanostructured rod (Fig.7.7), while two metarods were made out of rods made from single type of glass. The effective refractive indices of the five metarods create intermediate steps between the pure NC21 and F2 rods. For λ=1550 nm the effective refractive indexes are as follows: n_2 = 1.5242, n_3 = 1.5384, n_4 =1.5525, n_5 =1.5666 and n_6 =1.5807. Both the NC21 and F2 glasses are thermally matched to allow a joint thermal transformation at the optical fibre drawing tower. The assembly of the final structure was similar to one described in previous section, with the difference of using seven different types of rods, instead of two [7.10].

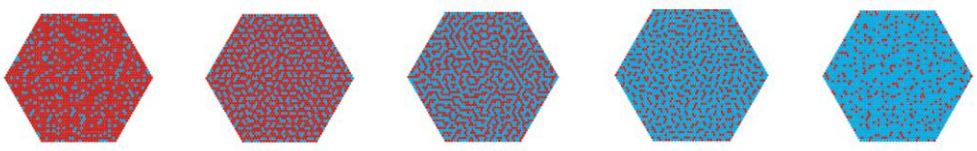

Figure 7.7 - Structures of five metarods composed of two fundamental glasses NC21 and NC25 according to calculated pattern to ensure uniform effective refractive index within every of 5 nanostructured rod: n_2 = 1.5242. n_3 = 1.5384, n_4 =1.5525, n_5 =1.5666. n_6 =1.5807.

As the lens was required to be elliptical instead of spherical [7.10] the final preform for the elliptical lens was assembled with the centrally placed subpreform and two large air

capillaries placed symmetrically with respect to the subpreform. The rest of the final preform area was filled with microrods made of NC21 low index glass. During the final drawing process, a vacuum was applied to air-holes. As a result, the air holes collapsed and modified the geometry of the final structure, breaking the rotational symmetry of the nanostructured subpreform and an elliptical gradient index lens was obtained (Fig. 7.8). Utilizing this method one can produce structures with various major and minor axis lengths by changing the temperature and pressure during the drawing process.

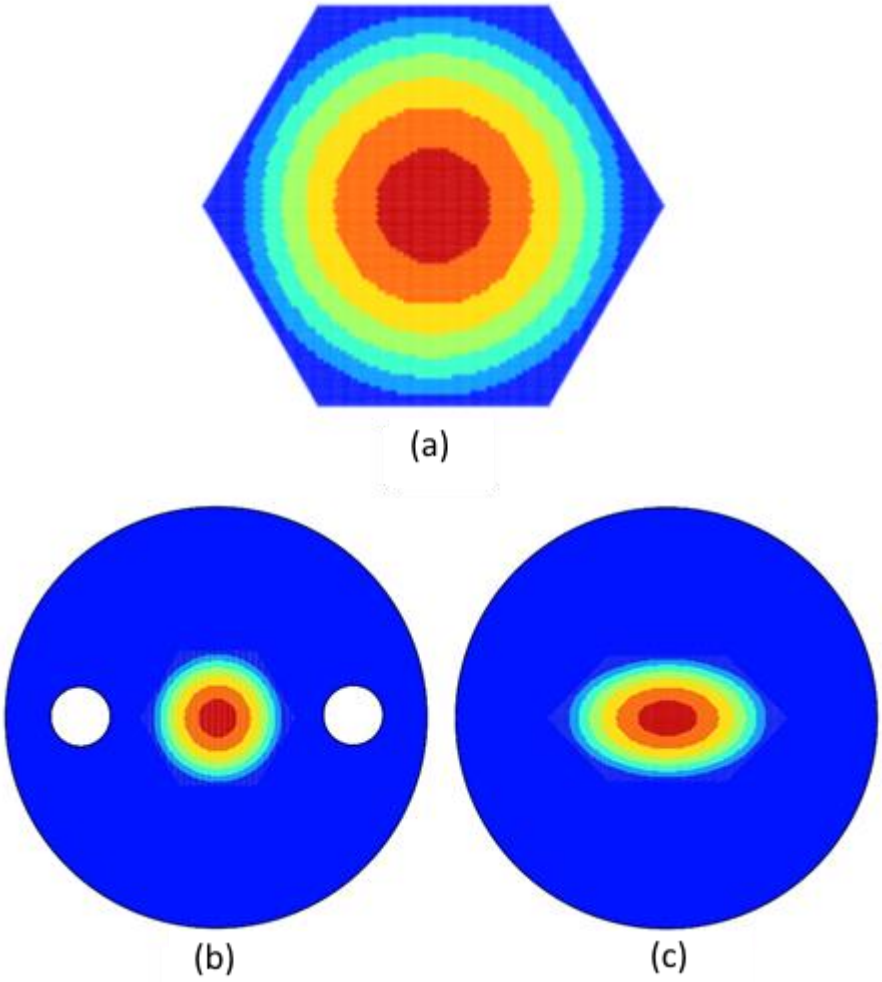

Figure 7.8 - A scheme of fabrication of nanostructured lenses. (a) Schematic of the original structure, (b) Final preform with two air holes on both sides of the structure, (c) structure after collapsing the air holes.

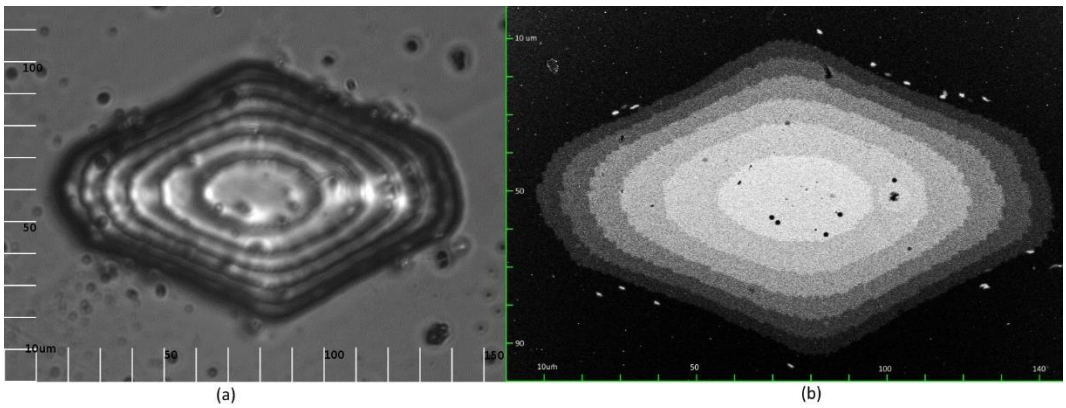

(a) (b)

Figure 7.9 - Elliptical multilevel graded index lens composed of two glasses silicate glass NC21 and lead oxide glass F2 seen under an optical (a) and scanning electron (b) microscope.

The final fabricated lens structure was verified with a scanning electron microscope (Fig 7.9b). A clear image of the elliptical-like ring structure that corresponds to the various effective indices was obtained. The size of the fabricated lens was 125μm × 75μm, with the feature size of the internal nanostructure of each metarod around 110nm.

7.2. Integration of GRIN optical elements with optical fibres

In the next step, the fabricated nanostructured elements are integrated into optical fibres. The difference in the melting temperatures of soft glasses (~600^{o}C) used for nanostructured element fabrication and silica glasses used in standard optical fibre (~1400^{o}C) meant that using industry-standard fusion splicers would deform the nanostructure before attaching it to silica fibre. All tests performed using this method resulted in nanostructured element melting in temperatures too low for the fused silica fibre to attach to it. There are integration methods that combine soft and silica glasses [7.11] but we were unable to utilise them. This meant that optical cement has to be used, instead of the usual methods.

7.2.1. Initial fibre-element integration tests

First attempts at integration were performed using a glass plate with a v-groove cut in it. As a passive method, that does not utilize any specialized equipment it is the easiest one to implement. The idea behind this method is to cut a v-groove with the external dimensions slightly exceeding the diameter of the nanostructured fibre in a glass plate. The optical fibre and nanostructured element fibre are then placed inside the cut and attached to each other. Connection between optical element fibre and optical fibre is made by UV hardening optical cement (Fig.7.10).

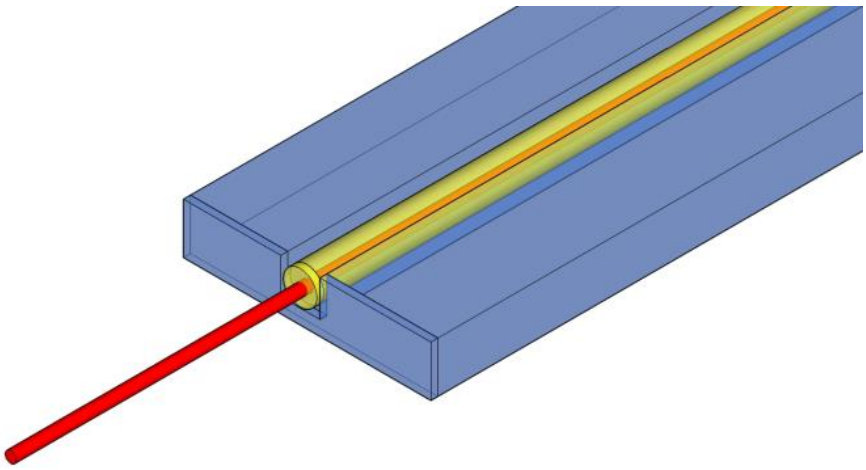

Figure 7.10 - Optical fibre with the nanostructured element attached inside glass holder.

The challenge in this method arose from precision machining. In order to have coupling the core of the optical fibre and centre of the nanostructured element fibre should be aligned with ±2μm precision. The grooves in the glass are cut by dicing saw with a circular blade. Blades of those saws are made with various precisions, the ones utilised in this thesis were machined with ±2μm precision. During cutting the blade warps slightly increasing this error. This meant that the cut groove has changing width and is not perfectly straight. In addition, typical optical fibre has a core positioned within ±1μm precision from the fibre centre, and the optical elements fabricated in-house were positioned within ±5μm from the centre line. The compound errors from all these factors meant that good passive positioning using v-groove was impossible with the equipment available. The use of the commercial v-grooves was considered at the beginning of the work. Unfortunately, initial optical element fibres had varied diameter (ranging between 115-140μm) which meant that commercial v-grooves were either to narrow, or too wide for the fibre.

As an active positioning method would be more complicated it was decided to try passive positioning using fibre fusion splicers only as an alignment method while still using optical cement to attach both elements. This would eliminate the challenges stemming from the errors in precision machining. Because fusion splicers are made to work with optical fibres the nanostructured element fibre had to be at least 1cm in length for the holder to securely grip it. Initial tests proved that after aligning and hardening the optical cement the 1cm nanostructured element fibre was too heavy and would fall off after removing it from the fusion splicer. This meant that with available equipment passive positioning methods would not work.

In the first attempts, it was assumed that the attachment of the optical fibre to the nanostructured element was the first stage of the integration process. After the connection was secured using optical cement the nanostructured element would be cut to the desired length and polished in the second stage of the integration process. Those tests proved that the optical fibre - nanostructured element connection was too fragile and broke under the stresses associated with grinding and polishing. In all subsequent tests the nanostructured elements were cut and polished in the first stage of the integration process. This meant that the integration process could be divided into three separate stages:

1) Cutting of the fibre with the optical elements
2) Grinding and polishing of the cut optical elements
3) Integration with the optical fibre

7.2.2. Cutting optical element fibre

The photonic nanostructure fabricated by using the stack and draw method described in Section 5.1 is placed in a groove cut in a glass plate. Each glass plate has a cross-section of 1×9mm, length 2cm and 130μm×130μm groove cut into the upper side (Fig. 7.11). The fibre is attached to the groove by a two-part adhesive to ensure that it will not break off during further stages of the process.

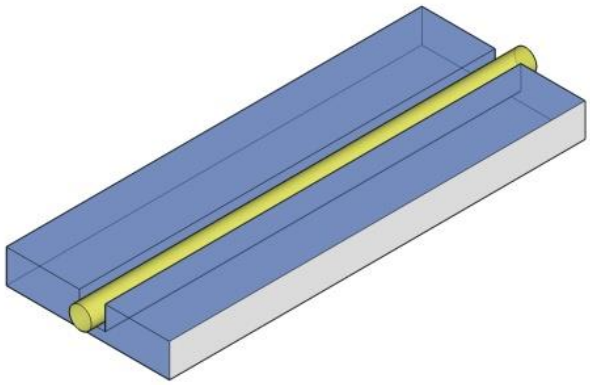

Figure 7.11 - Glass plate with lens inside the groove. The holder has a cross-section of 1×9mm and 2cm length.

The groove was made using a dicing saw with a circular blade. The saw used was an Automatic Disco Saw DAD 2H/6TM (Fig. 7.12).

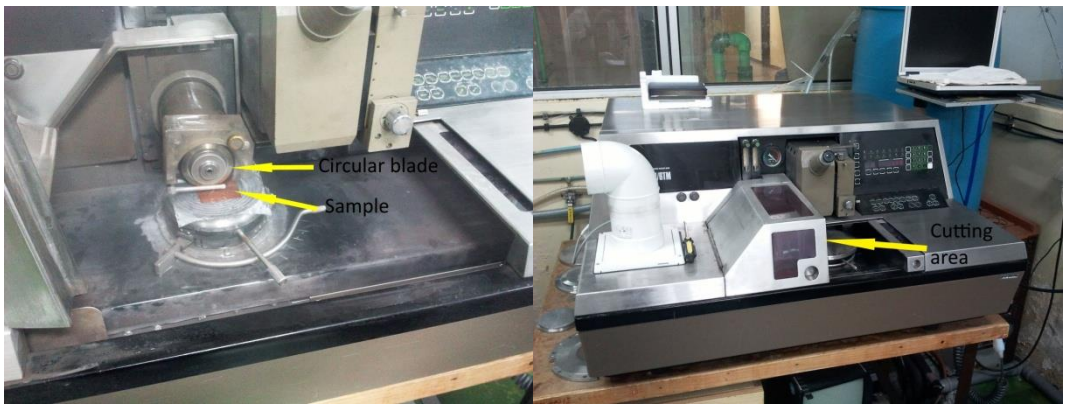

Figure 7.12 - Dicing Saw utilised in this thesis.

The glass plate with nanostructured element fibre attached was then cut into 0.4mm glass holders (Fig.7.13).

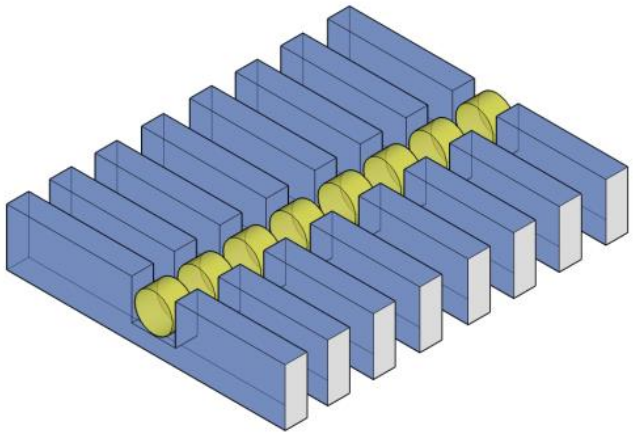

Figure 7.13 – Glass holder cut from glass plate. Each holder has a cross-section of 1×9mm and thickness of 0.4mm.

In order to obtain clear, straight cuts, the saw blades have to operate at high speeds of up to 30000 rpm. In order to reduce the heat generated during cutting the sample has to be cooled with strong jet of water. Glass holders with thickness of 0.4mm or more remained attached to the base plate during cutting. Reduction of the glass holder thickness resulted in water dislodging them during cutting. At a thickness of 0.1mm all the elements would fall off the base plate. This means that all the glass holders have to be ground down to the desired nanostructured element length after cutting.

7.2.3. Grinding and polishing optical elements

In the next stage of the integration process, the glass holders with nanostructured elements were attached using mounting wax to a base plate (Fig.7.14). The wax used in this thesis could be removed from the sample by acetone.

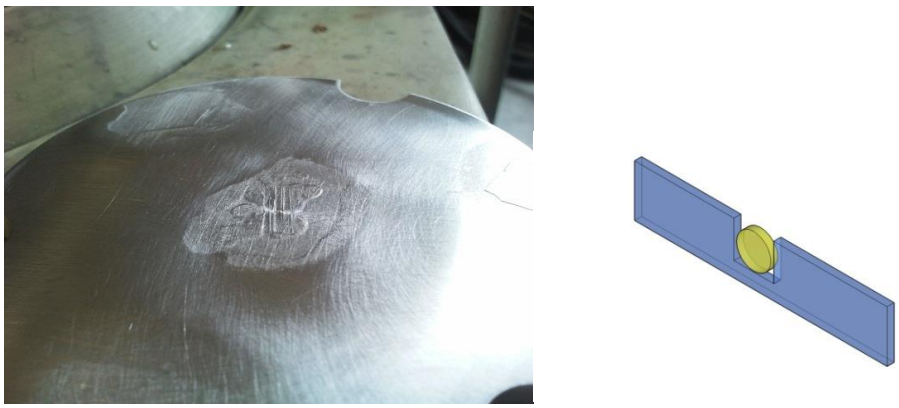

(a) (b)

Figure 7.14 - (a) Actual holder fixed to the base plate, (b) schematic of the holder with lens.

Several experiments proved that using a glass plate as the base plate is best for our purpose, as the sample can be seen through it and the quality of the polish can be easily ascertained using a microscope. Depending on the size of the base plate up to 30 glass holders could be polished at the same time. The polished glass holders are removed from the glass plate, inverted and again attached to the glass plate, so that the uneven surface is facing outward. Special care has to be taken to press down the samples to the glass plate. This is important, as the measurement of the thickness of the glass holder is performed with the base plate set as zero. This means that any mounting wax left between base plate and glass holder would increase the measured length of the glass holder. A thin film of mounting wax between the glass holder and the base plate always remained, but by using the same pressure for all samples the distance was kept stable and can be accounted for. The glass plate is attached to the grinding machine. In this thesis a G&N MPS 2R300S grinding machine was used (Fig. 7.15). The samples were then ground down to the set length. The shortest samples used in this thesis have thickness of 10μm.

Figure 7.15 - Grinding machine used in this thesis.

After removing the base plate from the grinding machine it was again transferred to the polishing table and the glass holder were polished. The nanostructured elements are then removed from the glass holders using tweezers. This step requires precision as each optical element is 125μm in diameter and 10 - 200μm in length.

7.2.4. Integration with optical fibre

As stated at the beginning of Section 7.2, the optical fibre and nanostructured element have to be aligned with ±2μm precision. In order to achieve this, both the nanostructured element and optical fibre had to be securely gripped during the integration and optical cement hardening. An inverted microscope with special fibre holder was used to achieve this (Fig. 7.17).

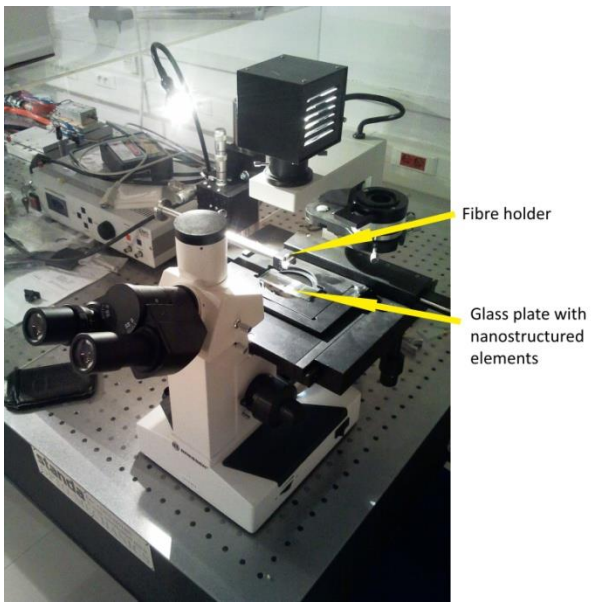

Figure 7.17 - Final setup for the optical fibre-nanostructured element integration.

The polished nanostructured elements are attached to the optical slate using water based adhesive. The optical slates are placed under the inverted microscope and the fibre is attached to the XYZ table (fibre holder in Fig. 7.17) extending above the optical slate. The optical cement is applied to the end of the optical fibre. In this work a Norland NOA65 optical adhesive was used. The adhesive has refractive index 1.524, and transmission spectrum shown in Fig. 7.18.

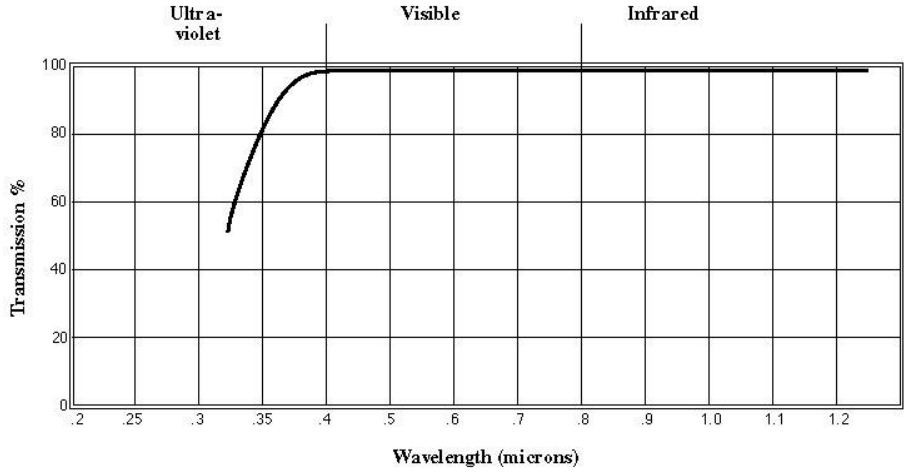

Figure 7.18 – Transmission spectrum of the NOA65 optical adhesive [7.12].

The fibre is then positioned above the nanostructured element so that core of the optical fibre and centre of the nanostructure are aligned. The fibre is then pressed down so that good contact between optical fibre and nanostructured element is achieved. The optical cement is exposed to UV light for 10 minutes. During this time the fibre is held securely

over the optical element so that no movement is possible. This is very important as without a secure grip on the optical fibre it would move more than 1μm from the centre of the nanostructured element.

After the optical cement is set, water is poured over the optical slate dissolving the water adhesive and leaving the nanostructured element firmly attached to the fibre (Fig. 7.19).

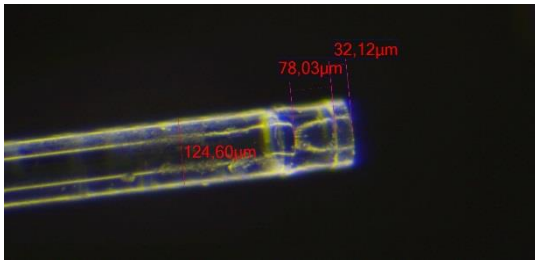

Figure 7.19 - Fibre with attached optical element.

7.3. Conclusions

The stack and draw method can be used for the fabrication of small diameter nanostructured optical elements. Due to size constraints of the fibre drawing furnaces, the external diameter of the structures is limited to around 20μm, while the diameter of the whole element is comparable to optical fibre – 125μm. Such elements can be successfully cut, ground and polished in order to create optical elements with previously designed external dimensions. A three step integration process allows the simultaneous preparation of up to 30 elements for integration. Larger numbers would be possible with an increase in the size of the grinding and polishing machines. Each optical element is actively aligned with the fibre with a ± 2μm precision and then attached using UV hardening optical cement. Using this method more than one element can be attached. Additional spacers can be placed between the nanostructured element and the optical fibre, or several nanostructured elements can be attached in line to the optical fibre.

Modifying the drawing process from two stage to three stage allows the fabrication of larger optical elements. Nanostructured metarods, composed of subwavelength scale glasses, were developed to create 5 materials with a graded change in their refractive index. A preform of a 7-level graded index lens with elliptical shape was created. Thanks to the large capillaries with vacuum applied during the drawing process, this structure has been stretched, resulting in an astigmatic step-index profile 75×125μm at the diagonals. In the standard stack and draw method any hexagonal or square structure can be fabricated. By selectively collapsing, or inflating air capillaries in the structure, additional shapes of the final structure can be obtained.

The next three chapters will show experimental verification of the fabricated elements. In chapter 7 the step-index elliptical lens is shown. Chapter 8 shows characterisation of small nanostructured lens and chapter 9 shows characterisation of small nanostructured axicon.

7.4. References

[7.1] D. W. Prather, A. Sharkawy, S. Shi, J. Murakowski, G. Schneider, *Photonic Crystals, Theory, Applications and Fabrication*, ISBN: 978-0-470-27803-1, John Wiley and Sons (2009)

[7.2] C. Tan, T. Niemi, C. Peng, M. Pessa, *Focusing effect of a graded index photonic crystal lens*, Optics Communications, 284(12), 3140-3143 (2011.)

[7.3] J. H. Schmid, P. Cheben, S. Janz, J. Lapointe, E. Post, D. Xu, *Gradient-index antireflective subwavelength structures for planar waveguide facets,* Opt Lett. , 32(13), 1794 (2007)

[7.4] M. R. Taghizadeh, A.J. Waddie, R. Buczynski, J. Nowosielski, A. Filipkowski, D. Pysz, *Nanostructured micro-optics based on a modified stack-and-draw fabrication technique,* Adv. Opt. Techn., 1(3), 171-180 (2012)

[7.5] J. M. Nowosielski, A. Filipkowski, A. J. Waddie, I. Kujawa, R. Stepien, *Diffractive optics development with stack-and-draw technique*, Proceedings of SPIE, 8428(1) (2012)

[7.6] L. Wang, D. He, L. Hu, D. Chen, *Heavily Yb-doped phosphate fiber with hexagonal inner cladding prepared by the stack-and-draw method*, Laser Physics, 25(3) (2015)

[7.7] J. Lousteau, G. Scarpignato, G. Athanasiou, E. Mura, N. Boetti, M. Olivero, T. Benson, P. Sewell, S. Abrate, D. Milanese, *Photonic bandgap confinement in an all-solid tellurite-glass photonic crystal fiber*, Optics Letters, 37(23), 4922-4924 (2012)

[7.8] J. Knight, *Photonic crystal fibres*, Nature, 424, 847-851 (2003)

[7.9] R. Buczynski, I. Kujawa, R. Kasztelanic, D. Pysz, K. Borzycki, F. Berghmans, H. Thienpont, R. Stepien, *Supercontinuum generation in all-solid photonic crystal fiber with low index core*, Laser Physics, 22(4), 784-790 (2012)

[7.10] J. M. Nowosielski, *Nanostructured Birefringent and Gradient-Index Micro-Optical Elements*, Thesis collection, Heriot Watt University (2013)

[7.11] M. Murawski, G. Stepniewski, T. Tenderenda, M. Napierała, Z. Hołdyński, L. Szostkiewicz, M. Slowikowski, M. Szymanski, L. Ostrowski, L. R. Jaroszewicz, R.

Buczyński, T. Nasiłowski, *Low loss coupling and splicing of standard single mode fibers with all-solid soft-glass microstructured fibers for supercontinuum generation,* Optical Components and Materials XI (2014)

[7.12] Norland Optical Adhesives, https://www.norlandprod.com/adhesives/noa%2065.html, Norland Products, Annaheim, California, USA (2016)

8. LARGE ELLIPTICAL GRIN LENS

In this chapter, the simulation and experimental verification of the new optical elements is considered. The initial verification of the large elliptical lens is a direct continuation of previous work done by J. Nowosielski [8.1]. As this lens is significantly larger than all of the other optical elements described in this thesis, measuring ~125x75μm, it could not be attached to the optical fibre. Section 8.1 describes the numerical simulations of the step index elliptical lens, comparing it to the lens with continuous refractive index distribution. The dimensions of the simulated lenses are similar to the fabricated lenses – 125×75μm. Computer simulations are performed for infinite lenses in order to obtain pitch lengths for both the step index and ideal lenses. The next set of simulations shows light propagation through a 140μm long lens for both the ideal and step index lenses. Section 8.2 shows the experiments performed to verify the performance of the fabricated lenses. In the first experiments the 140μm long lens was tested. In addition, a second set of experiments was performed for a lens length of 170μm. Both sets of experiments were conducted for 630nm and 1550nm wavelengths of incident light.

8.1. Numerical verification of the step index lens

The ideal elliptical lens contains a continuous change of refractive index, but such a gradient is difficult to fabricate in a flat-parallel form factor. In practice, one can substitute a continuous gradient with a step index one to obtain a converging power similar to that of the continuous case. In the case of lenses with a diameter in the order of 150μm, 7-8 levels of quantization are sufficient [8.2, 8.3].

Using the Fast Fourier Transform Beam Propagation Method (FFT BPM), as described in Chapter 3, we compared the performance of the lenses with quantized gradient index levels against an ideal GRIN lens (Fig. 8.1) with a continuous change of refractive index profile. The modelled lenses had dimensions similar to the fabricated one, with cross-sections of 125×75μm. The simulations were performed at a wavelength of 1550nm with the source being a plane wave. To identify the quarter pitch for both orthogonal axes the light was propagated through an infinite rod lens. The FFT BPM has a spatial resolution of 0.125μm in the plane of the lens and 1μm along the propagation axis, in order to ensure convergence of the algorithm.

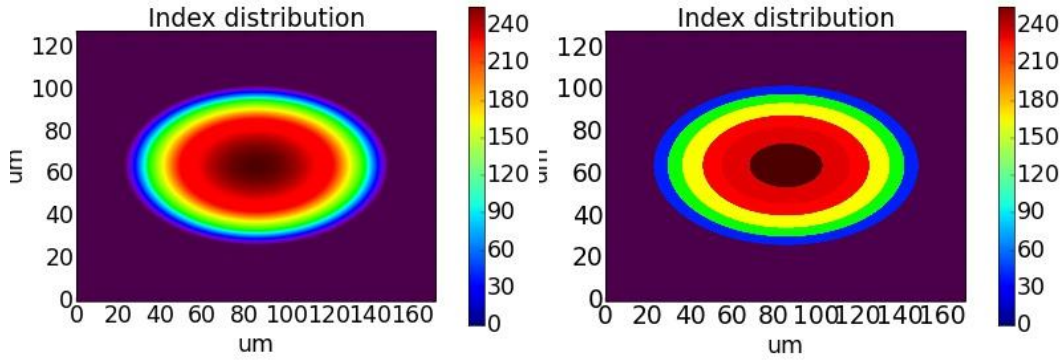

(a) (b)

Figure 8.1 - (a) Large elliptical lens with continuous refractive index distribution, (b) step index lens.

Based on the results of the simulations, we determined the quarter pitches for both the ideal and quantized GRIN lenses (Fig. 8.2 and 8.3) to be 190µm and 300µm for the orthogonal axes of the ideal GRIN elliptical lens, and 175µm and 295µm for the orthogonal axes of the quantized GRIN elliptical lens. Both simulations show good agreement and only minor differences in the effective parameters. Obviously the results obtained from the quantized lens would be closer to the ideal if the number of quantization steps was increased. However, 7 steps are a good compromise between the efficiency of the lens and the development effort.

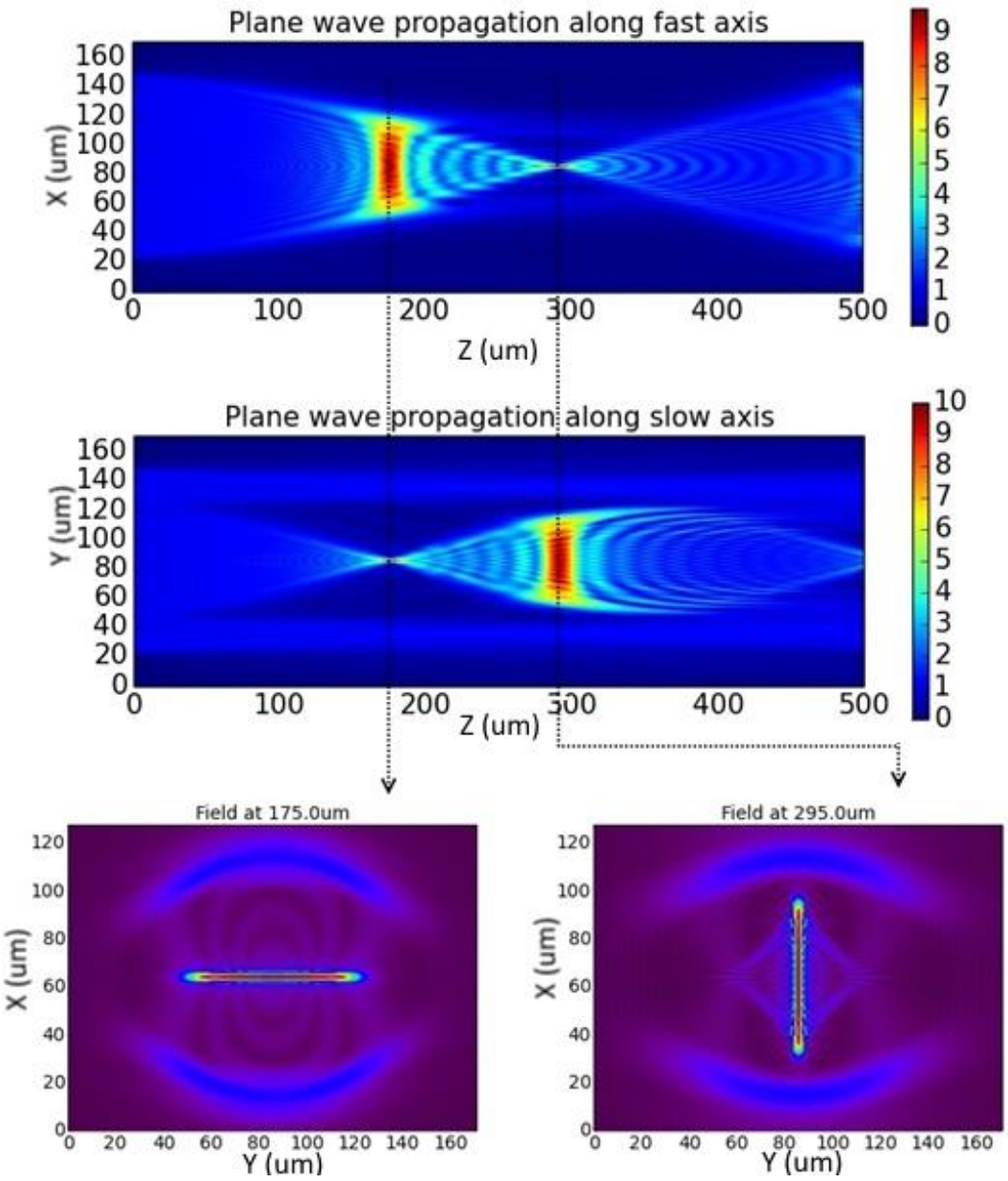

Figure 8.2 - Light propagation in continuous profile elliptical GRIN lens with the infinite length: propagation of plane wave in gradient index medium along fast axis (a), propagation of plane wave in gradient index medium along slow axis (b).

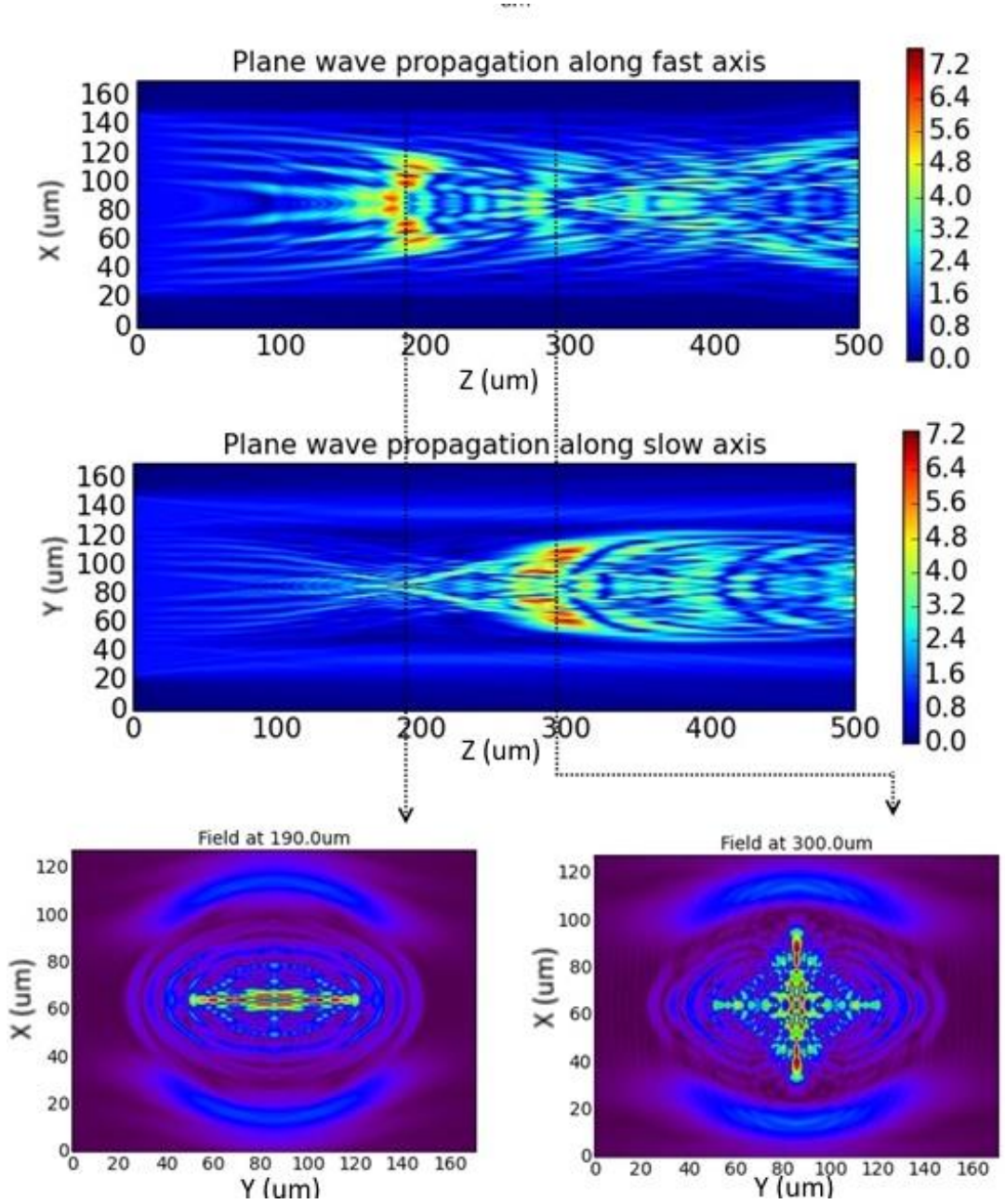

Figure 8.3 - Light propagation in step index profile elliptical GRIN lens with the infinite length: propagation of plane wave in gradient index medium along fast axis (a), propagation of plane wave in gradient index medium along slow axis (b).

For the second set of simulations, the GRIN lenses length was set to 140μm, corresponding to the length used in the experiments. This length is well below the quarter pitch length determined in the previous simulations and therefore both focal planes of the lenses will be located in free space. The simulation results for both ideal and quantized lenses of 140μm length are presented in Fig. 8.4 and 8.5.

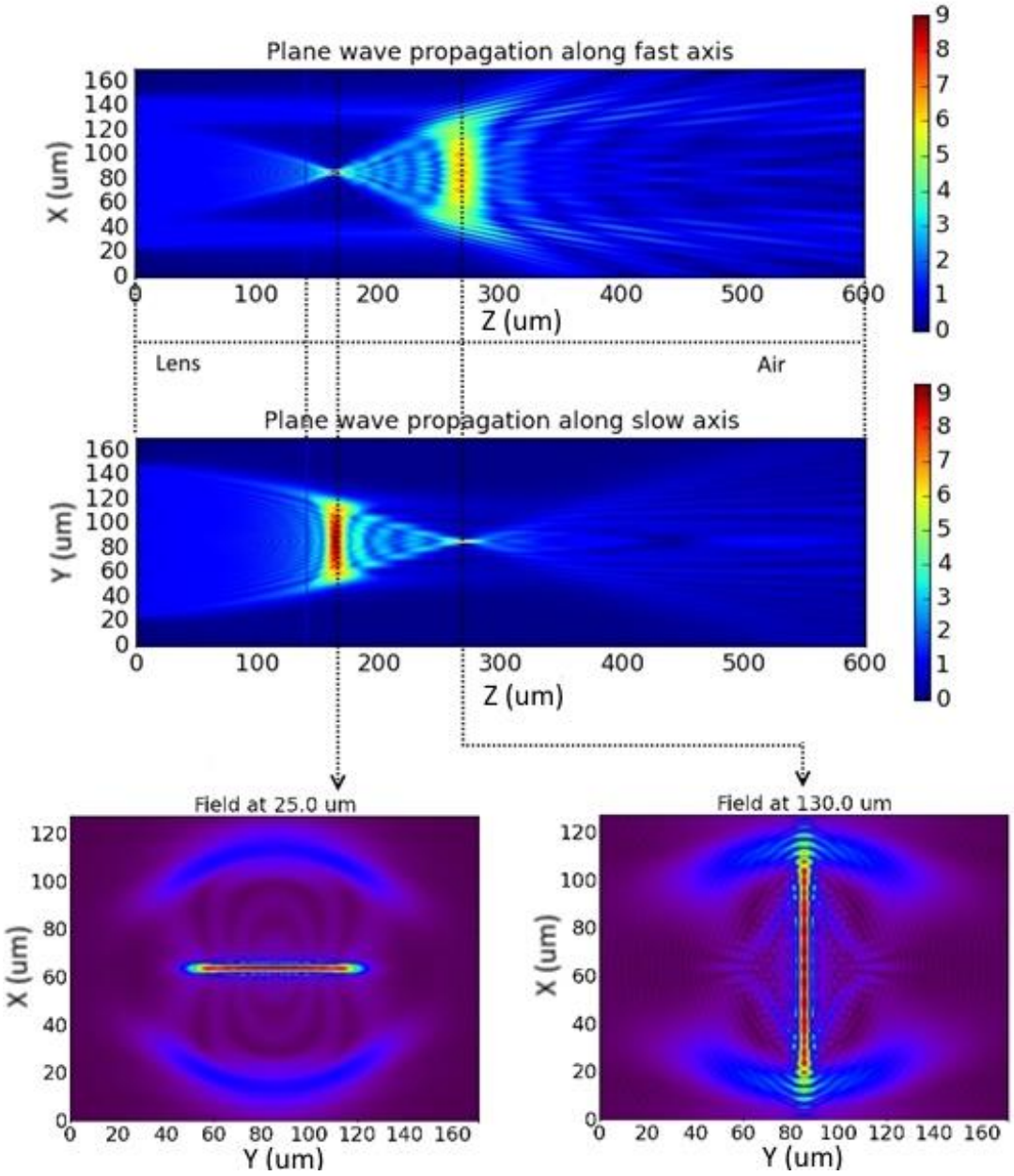

Figure 8.4 - Light propagation in ideal profile elliptical GRIN lens 140μm in length: propagation of plane wave in gradient index medium along fast axis (a), propagation of plane wave in gradient index medium along slow axis (b).

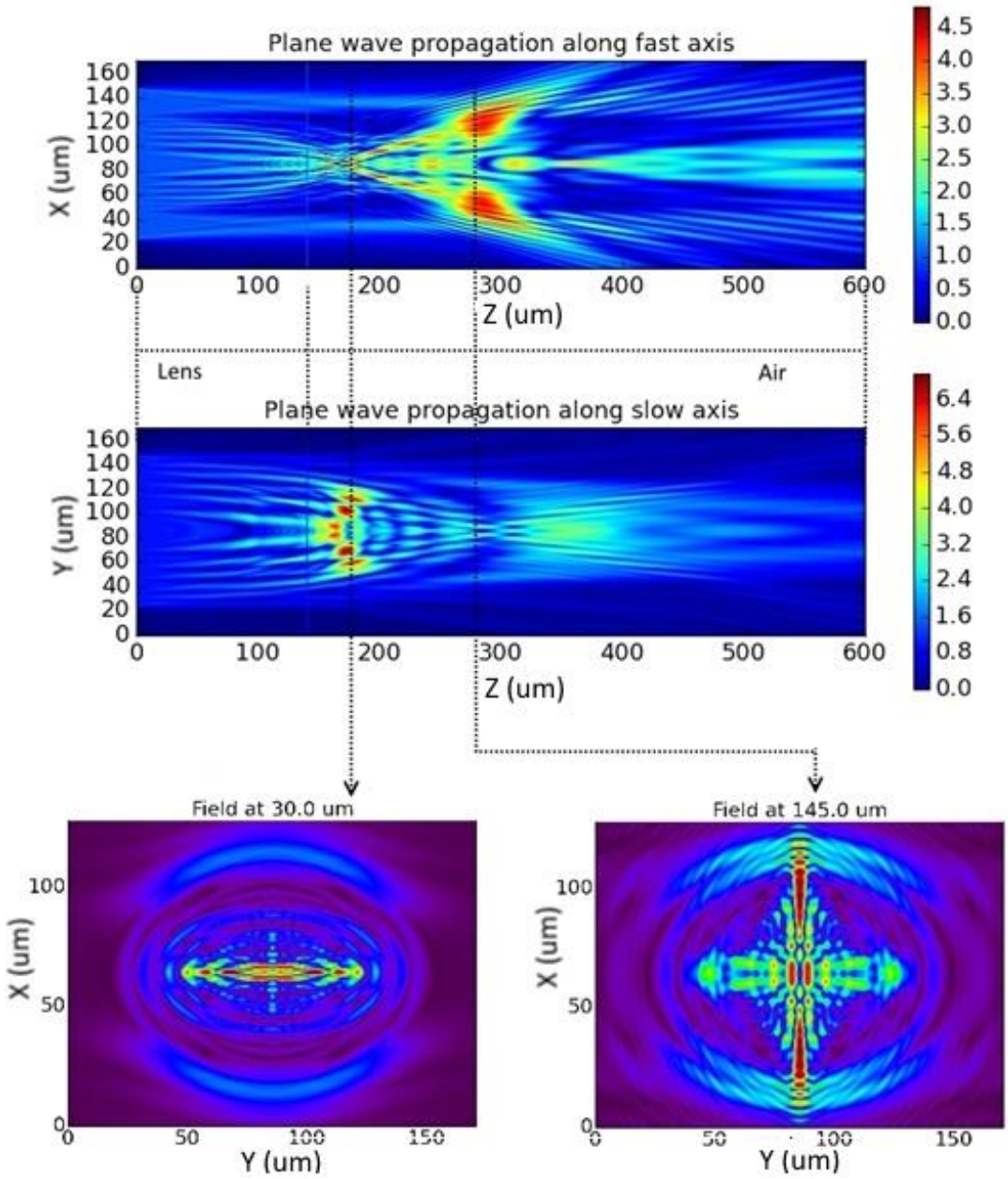

Figure 8.5 - Light propagation in step index profile elliptical GRIN lens 140μm in length: propagation of plane wave in gradient index medium along fast axis (a), propagation of plane wave in gradient index medium along slow axis (b).

The obtained results show a degradation of the expected performance of the nanostructured lenses with respect to the ideal lenses. The reason behind this is diffraction at the sharp edges between the refractive index steps of the lens, the large difference between the refractive indexes in each step and the large area of each step relative to the wavelength. In practice, the properties of the fabricated nanostructured lens should be better than that observed in the simulations, due to the glass diffusion softening the transition between the various refractive index areas of the lens.

For the ideal GRIN lens, the working distances for both the orthogonal axes are 25μm and 130μm, where working distance is defined as the distance between the focal plane and the end plane of the lens. In the case of the quantized GRIN lens the working distance for the fast axis is 30μm and working distance for the slow axis cannot be determined (Figure 8.6).

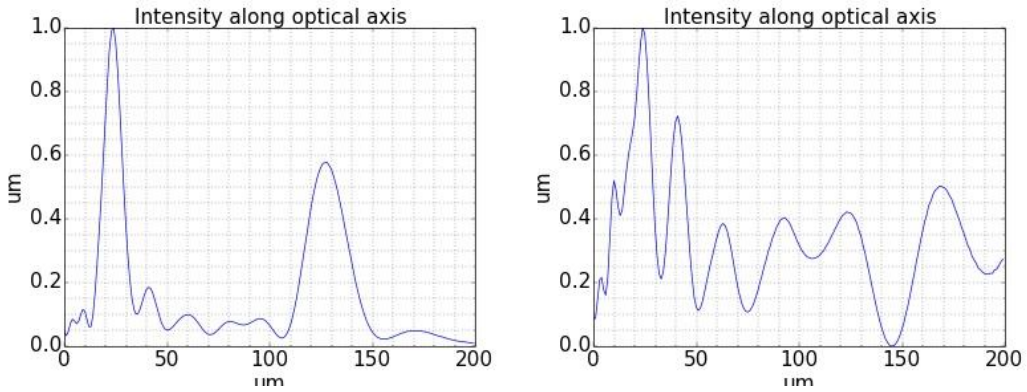

(a) (b)

Figure 8.6 - Light intensity along optical axis in lenses 140μm long: (a) in continuous profile elliptical GRIN lens, (b) in step index profile elliptical GRIN lens. In both cases the intensity is averaged over radius of 1μm from the centre of the propagation axis.

8.2. Experimental results

The fabricated elliptical GRIN microlenses were characterized to verify their effective parameters. We used two lasers emitting at 633nm and 1550 nm coupled into single mode fibre as sources, with the output beam collimated with an aspheric lens. Light after propagating through the lens was magnified by the ×20 microscope objective (NA=0.35) and then projected onto a CCD camera that works with a fixed gain in the linear regime. In the case of the 1550 nm laser, an EDMUND OPTICS analogue NIR CCD camera was used. This camera has a resolution of 720×576 pixels. The elliptical GRIN microlenses were glued to glass slides using optical cement. These slides in turn were mounted on a 3-axis translation stage (fig 8.7). Two lenses were prepared for the experiments – one 140μm long and second 170μm long. This corresponds to 0.18 and 0.22 of lens pitch length respectively. The focal plane of the lens was determined by scanning with the imaging system along the optical axis, with the translation resolution of such measurements being ±3μm.

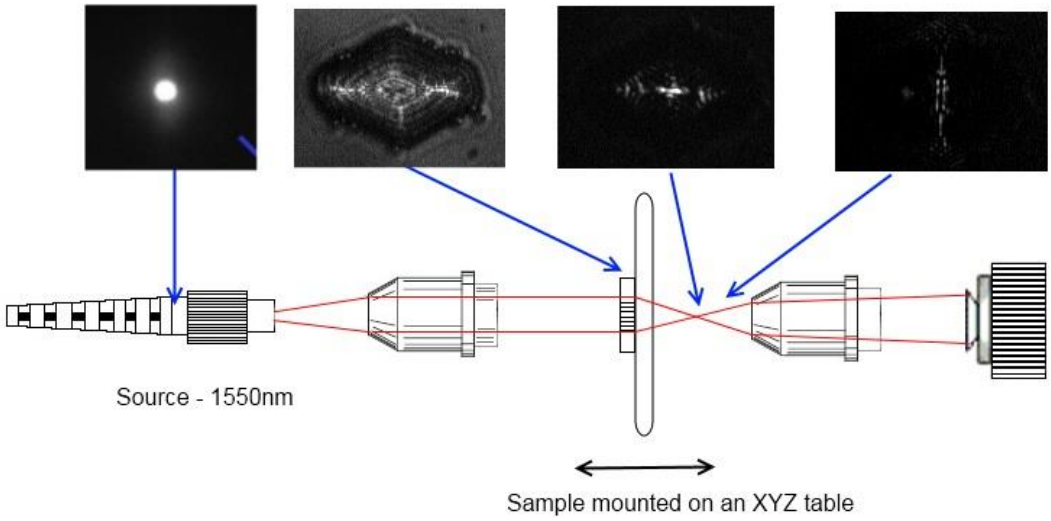

Figure 8.7 - Experimental setup for characterization of quantized elliptical GRIN microlenses.

With the 633nm laser source there was no observable focusing behaviour. This is in agreement with the results of the simulations, which predicted that the feature size of the 'metarods' used for the development of the quantized elliptical GRIN lens are too large with respect to the wavelength. This means that metarods cannot be treated as a medium with a homogeneous effective refractive index. Moreover 7 steps are not enough to obtain a quasi-continuous change of gradient index profile in a quantized elliptical GRIN lens with a size 125×75μm.

The next experiment used a 1550nm laser as the source. In this case, clear focal lines for both orthogonal axes of the elliptical lens were observed, demonstrating the proper operation of the elliptical lens as expected for this wavelength (Fig. 8.5). For the 140μm microlens the measured working distances were 90μm and 200μm, (Fig. 8.8). The size of the focus is 3.8 × 21.6μm in the first focal plane and 25.5 × 7.4μm in the second focal plane.

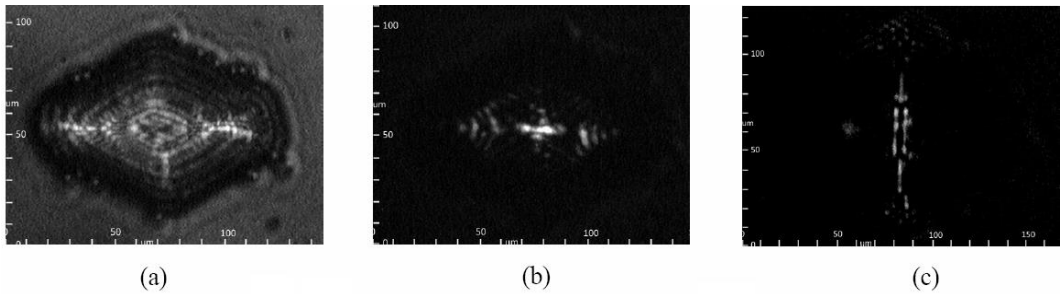

Figure 8.8 - Cross-section of propagating beam behind quantized elliptical GRIN microlens with the length of 140μm at the end faced of the lens (a) and at the both orthogonal focal planes at the working distances of 90μm (b) and 200μm (c).

Based on the simulation results, the predicted working distances were 30μm and 145μm, giving differences of 60μm and 55μm for both axes between theory and experiment. These differences in the working distances are the result of the diffusion processes between the quantized levels in the lens that occurred during the drawing process. This phenomenon was not taken into account in the simulations, but as it affects both axes in similar manner, the differences between the predicted and experimental results are similar for both axes. In order to confirm this detailed information about the diffusion region has to be introduced to the simulation. A method of characterisation of the diffused area based on heavy ion measurements exists which can be used for glasses with some lead content. In the case under consideration in this chapter, both glasses are without lead so there was no method available to us to characterise the diffused area of the optical element.

Some scattered light was also observed in the focal plane and is a result of the quantized structure of the measured lens and similar to that predicted in the simulations (Fig. 8.5).

The same experiment was conducted for the 170μm length lens, using a 1550nm laser source. For this lens the working distances for both orthogonal axes were 90μm and 180μm respectively (Fig. 8.9). The size of focus was 3.25×18.6μm in the first focal plane and 7.2×22.5μm in the second focal plane.

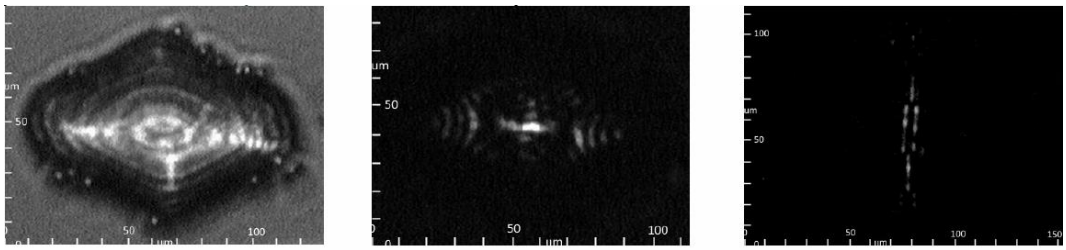

Figure 8.9 - Cross-section of propagating beam behind quantized elliptical GRIN microlens with the length of 170μm at the end faced of the lens (a) and at the both orthogonal focal planes at the working distances of 90μm (b) and 180μm (c).

8.3. Conclusions

Computer simulations performed for the 125×75μm lenses show that the quarter pitch of the elliptical lenses is 190μm and 300μm for the orthogonal axes of the ideal GRIN elliptical lens, and 175μm and 295μm for the orthogonal axes of the quantized GRIN elliptical lens. Both simulations show good agreement and minor differences in effective parameters. Experiments were performed for the 140μm and 170μm lengths of lenses,

which corresponds to 0.18 and 0.22 pitch length respectively for the incident wavelength of 1550nm. For the 140μm microlens we obtained working distances of 90μm and 200μm for both orthogonal axes, respectively. For the 170μm lens the working distances for both orthogonal axes were 90μm and 180μm, respectively (Table 8.1), which differ by 60μm and 55μm from the experiment. We believe that this can be explained by the glass diffusion of the fabricated lenses, which changes the refractive index distribution in the fabricated lens. Experiments performed with 630nm laser source show that there is no observable focusing behaviour. This is in line with the theoretical predictions, which state that the feature size of the 'metarods' used for the development of the quantized elliptical GRIN lens are too large with respect to the wavelength, and in order for the lens to work incident wavelength has to be 1550nm.

	140μm simulation	140μm experiment	170μm experiment
Fast axis focal plane	30μm	90μm	90μm
Slow axis focal plane	145μm	200μm	180μm

Table 8.1. Comparison of working distances between both fabricated lenses and simulations.

8.4. References

[8.1] J. M. Nowosielski, *Nanostructured Birefringent and Gradient-Index Micro-Optical Elements*, Thesis collection, Heriot Watt University (2014)

[8.2] J. Nowosielski, R. Buczynski, A. J. Waddie, A. Filipkowski, D. Pysz, A. McCarthy, R. Stepien, M. R. Taghizadeh, *Large diameter nanostructured gradient index lens*, Opt. Express, 20 (2012)

[8.3] F. Li, Y. Gao, *Design and analysis of quantized micro gradient index lens*, Optik - International Journal for Light and Electron Optics, 124(24), 6954–6957 (2013)

9. SMALL NANOSTRUCTURED GRIN LENS

In this Chapter, computer simulations and experimental verification of the small nanostructured lens are shown. Section 9.1 describes the simulations performed in order to find best spacer length for a 20μm diameter lens attached to the optical fibre. The second series of simulations in this section shows the light propagation after nanostructured lenses with various lengths. In section 9.3 the results of experimental verification are shown. A nanostructured lens, with a diameter of around 20μm was attached to the optical fibre. The nanostructured lens is 11.96μm long attached to a spacer 71.46μm long. Experiments were conducted for an incident wavelength of 1550nm.

9.1. Numerical verification of the nanostructured lens

Using the Fast Fourier transform Beam Propagation Method (FFT BPM) we simulated different variations of the attached optical element to the fibre. The first series of simulations were done for light propagating through the bare optical fibre (Fig.9.1). The fibre used in these simulations has a core diameter of 4.6μm and a length of 400μm. The fibre has a core refractive index of ncore= 1.452 and a cladding refractive index $n_{cladding}$= 1.446. The incident light is a 1550nm Gaussian beam with a $1/e^2$ diameter of 4.6μm wide. The FFT PBM has a spatial resolution of 0.1942μm in the plane of the lens and 1μm along the propagation axis, in order to ensure convergence of the algorithm.

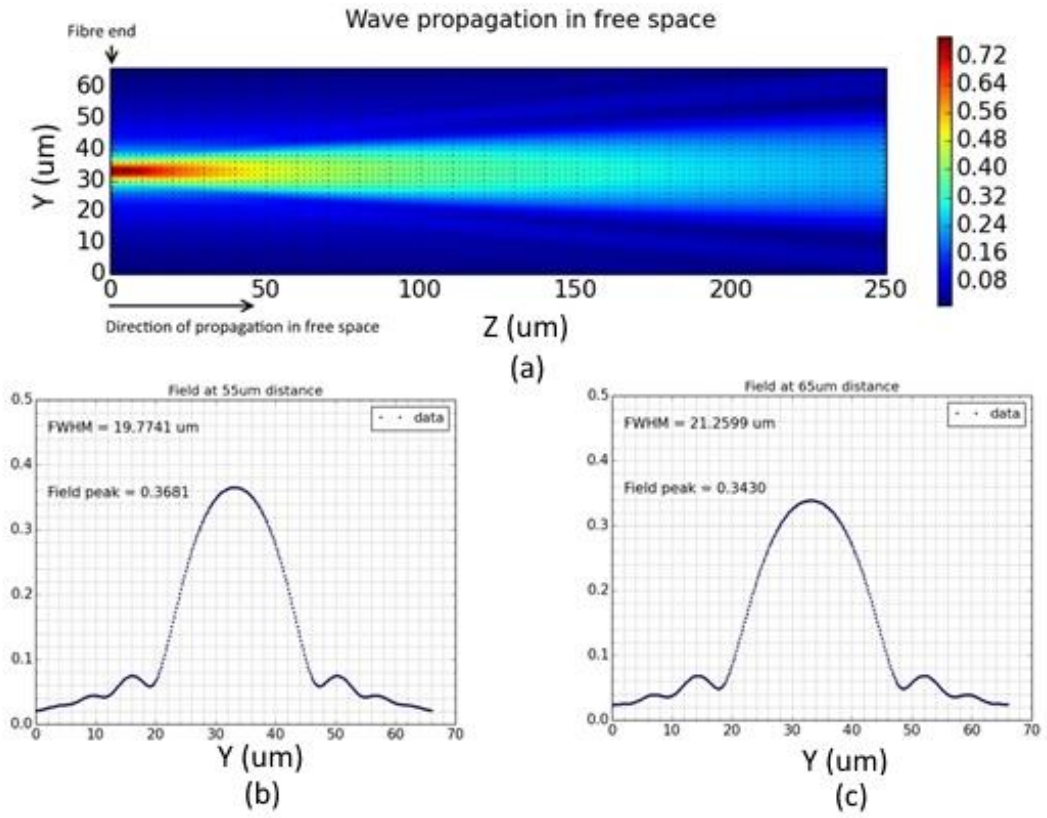

Figure 9.1 - Beam propagation after end plane of the optical fibre in air n=1. Fibre has a core diameter 4.6μm and 400μm length. The refractive index of the core is n_{core}=1.452. The cladding has a refractive index $n_{cladding}$=1.446. (a) Field amplitude, (b) FWHM measurements of the beam at working distance 55μm, (c) FWHM measurements of the beam at working distance 65μm.

As expected the waist of the beam is located at the end plane of the fibre, with the light spot widening with an increase of a distance from the fibre. As seen in Chapter 4.4 nanostructured lenses do not have an ideally uniform refractive index distribution. The largest difference between the ideal and nanostructured refractive index distributions occurs at the centre of the lens. As can be seen in Fig. 9.1 for the lens attached directly to the fibre most of the energy illuminates the centre of the lens. With the increased distance more of the surface area of the lens is illuminated. At the distance of ~60μm full width at half maximum (FWHM) is equal to ~20μm. In order to separate the lens from the fibre one has to place a spacer between the lens and fibre. The spacers used in this thesis are made from NC34 glass with refractive index n_{NC34}=1.55 for 1550nm incident light. This is the same glass that is used as the higher refractive index glass in the nanostructured optical elements. Figure 9.2 show that for an optical element with diameter around 20μm the spacer should not exceed 80μm. At lengths longer than this,

the FWHM of the beam exceeds 20µm, meaning that most of the light would escape around the optical element.

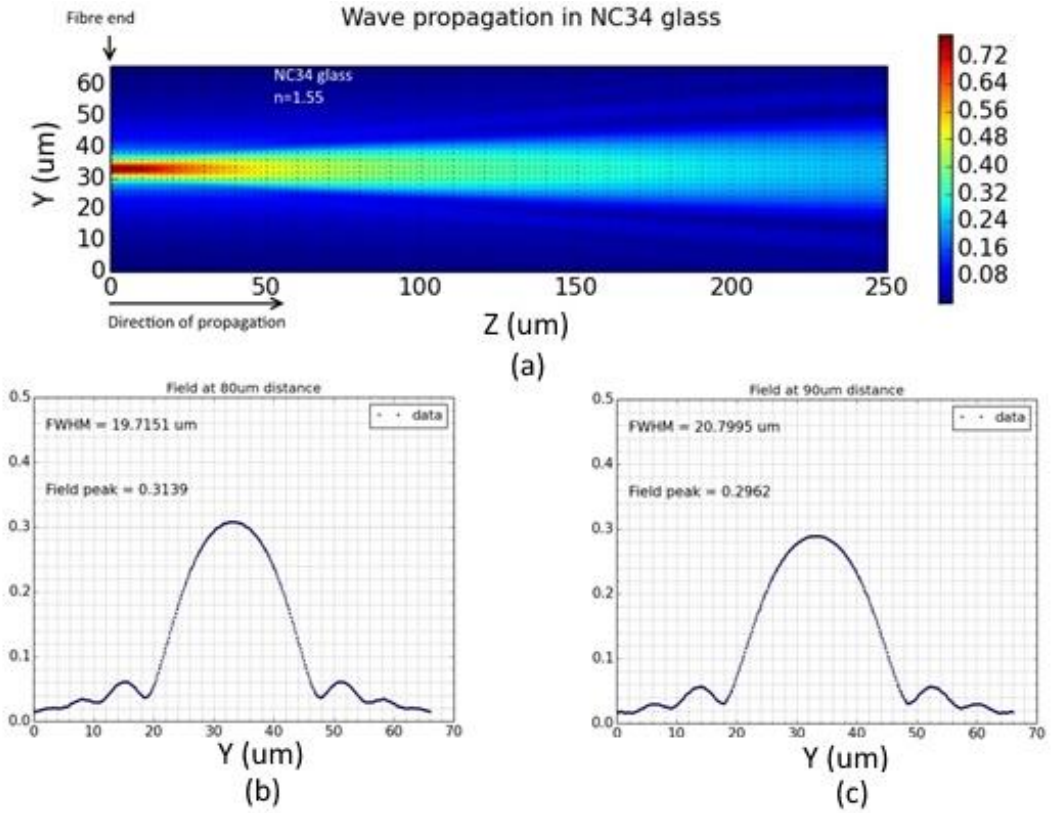

Figure 9.2 - Beam propagation after end plane of the optical fibre through NC34 glass. Fibre has a core diameter 4.6µm and 400µm length. The refractive index of the core is $_{ncore}$=1.452, of the cladding $n_{cladding}$=1.446. The NC34 glass has refractive index nNC34=1.55. (a) Field amplitude, (b) FWHM measurements of the beam at working distance 80µm, (c) FWHM measurements of the beam at working distance 90µm.

The next set of simulations was performed for an optical element attached to the fibre. The optical element used was a nanostructured lens with a diameter of 19.42µm. The glasses used in the structure of the lens have refractive indexes n_1= 1.55 and n_2=1.5101. According to the theory explained in Chapter 2.1, a lens with those dimensions and refractive indices should have a quarter pitch length of 67µm. This means that for the simulated lenses with length equal to 50µm all focal planes should be positioned behind the end plane in free space. Figure 9.3 shows beam changes in the propagation with increase of the spacer length from 0 to 130µm. As before the spacer is made from clear NC34 glass.

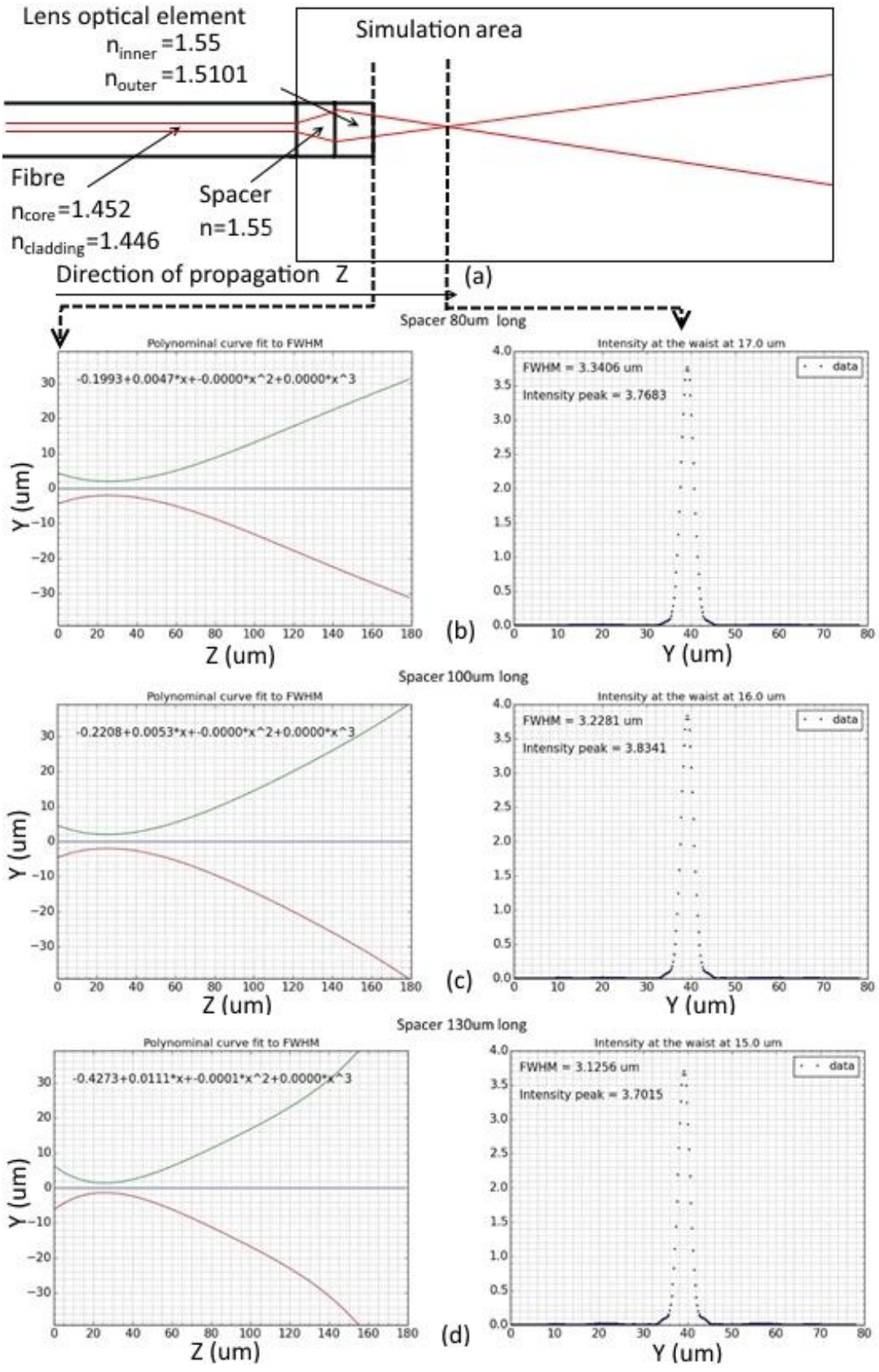

Figure 9.3 - Beam propagation after end plane of the optical element attached to the fibre with NC34 spacer positioned in-between. Fibre has a core diameter 4.6µm and 400µm length. (a) Schematic of the simulation setup (b) results for spacer 80µm in length, (c) results for spacer 100µm in length, (d) results for spacer 130µm in length. Intensity is normalised to the fibre output.

Those simulations confirm that the highest peak of the light intensity propagating after the lens is for the spacer 100μm in length. This is in line with predictions from the beginning of this chapter (Fig.9.2). For the spacer 80μm in length most of the light is focused on the centre of the lens increasing the influence of the defects of the refractive index distribution on the light propagation. For the spacer 130μm in length the FWHM of the beam is wider than the lens diameter, resulting in some of the light propagating outside the lens. The ideal length of the spacer should be 100μm – all of the lens area is illuminated and no of the light is propagating outside the lens.

The next set of simulations was performed to see how beam propagation changes with the length of the nanostructured lens. The simulations were performed for lens lengths of 20μm, 40μm and 50μm. The results are shown in Figure 9.4.

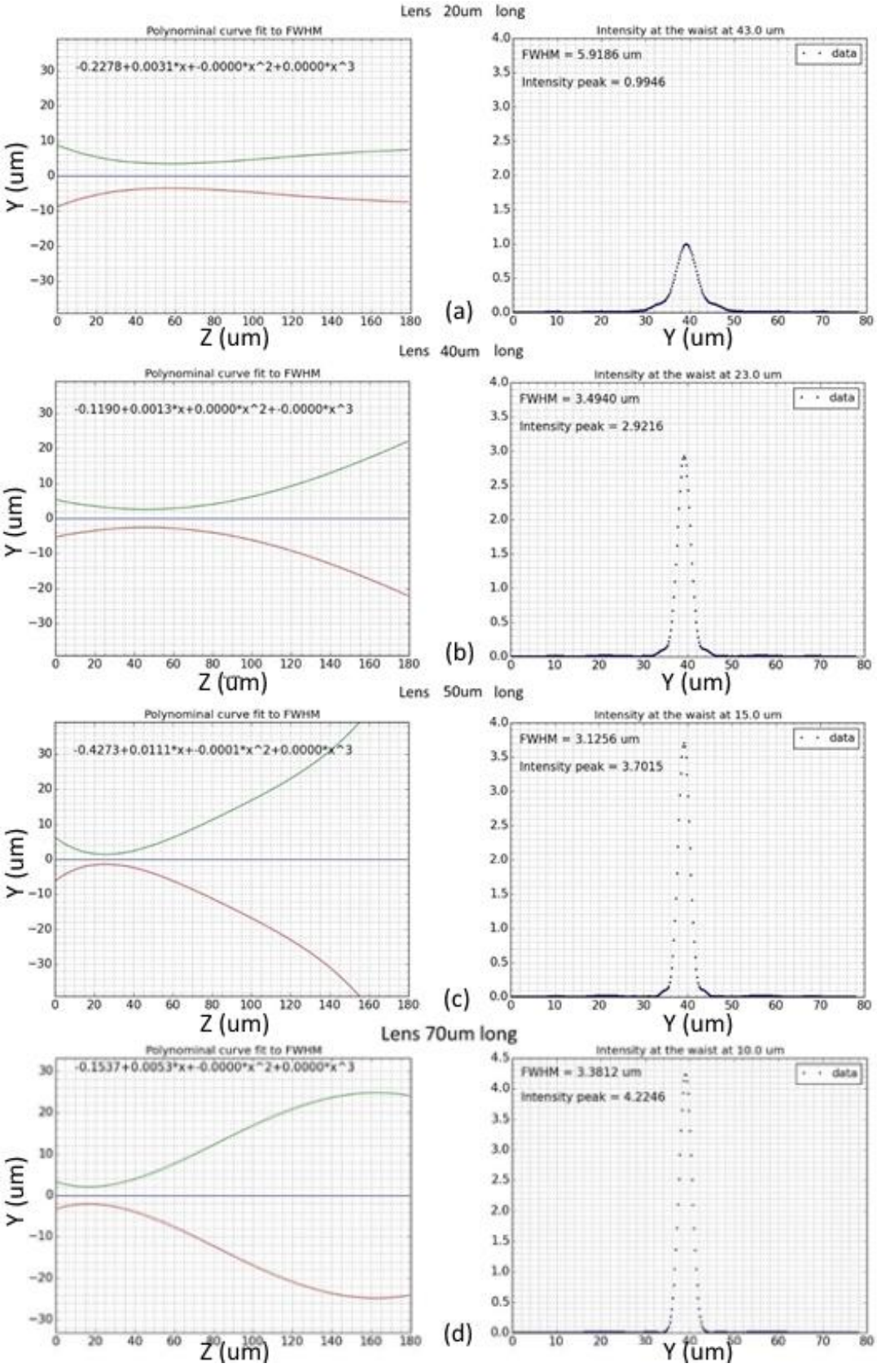

Figure 9.4 - Beam propagation after end plane of the optical element attached to the fibre with NC34 spacer positioned in-between. Fibre has a core diameter 4.6µm and 400µm length, spacer has length 100µm. (a) results for 20µm lens length, (b) results for 40µm lens length, (c) results for the 50µm lens length. (d) result for 70µm lens length. Intensity is normalised to the fibre output.

As can be expected the highest intensity peak, equal to 4.2246 of the intensity at the fibre end, can be observed for the lens closest to the quarter pitch length – 70μm. The FWHM of the beam in the focal plane is 3.3812μm, and the focal plane moves closer to the exit facet of the lens the longer the lens is.

5.1. Development of nanostructured lens

The process of nanostructured optical element fabrication and integration to the optical fibre was described in Chapter 6. For the nanostructured lens a spacer was fitted between the fibre and optical element. The spacer was attached using the same method as for the nanostructured lens, described in Chapter 6. This means that steps necessary for nanostructured lens integration to the fibre using optical cement were repeated for the spacer.

The lens was 11.9μm long, with a spacer length of 71.5μm. The diameter of the lens was around 20μm (Fig. 9.5). The length of the lens is smaller than the ideal calculated in Chapter 4. This is the result of the fabrication process. The length of the final optical element is calculated based on the amount of glass removed during grinding (section 6.4.2). This does not take into account the amount of adhesive between the base plate and optical element. In the case of this element the amount of adhesive was larger than anticipated, resulting in the optical element being slightly raised from the glass plate.

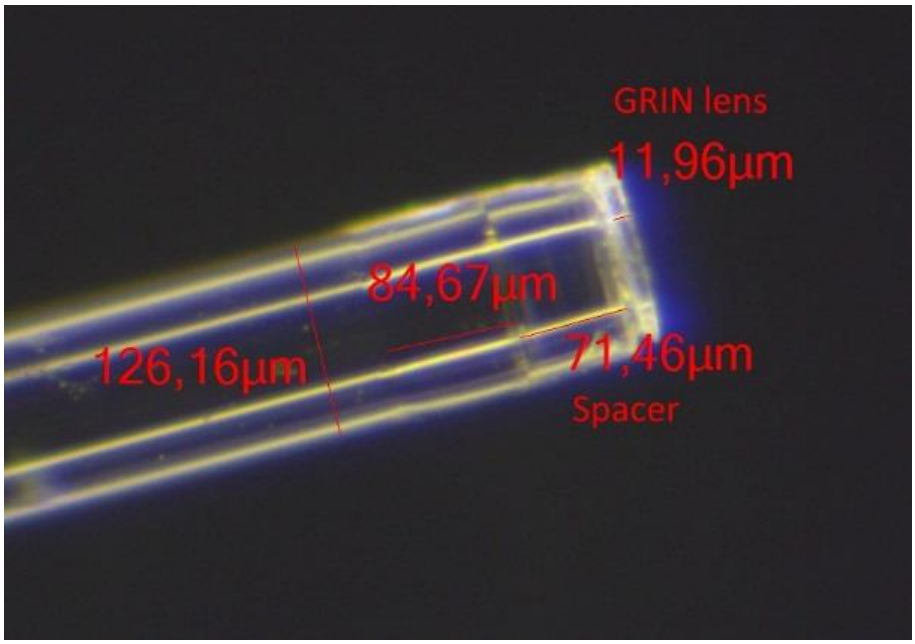

Figure 9.5 - Small nanostructured lens composed of two glasses NC21 and NC34 attached to the optical fibre.

9.2. Experimental results

The fabricated GRIN microlenses were characterized to verify their effective parameters. We used 1550 nm laser coupled into single mode fibre as source. At the other end of the fibre the spacer and nanostructured lens was attached by the optical cement (Fig.9.4). Light after propagating through the lens was magnified by the ×20 microscope objective (NA=0.35) and then projected onto a CCD camera that works with a fixed gain in the linear regime. An EDMUND OPTICS analogue NIR CCD camera was used. This camera has a resolution of 720 × 576 pixels. The focal plane of the lens was determined by scanning with the imaging system along the optical axis, with the translation resolution of such measurement ±3μm (Fig.9.6).

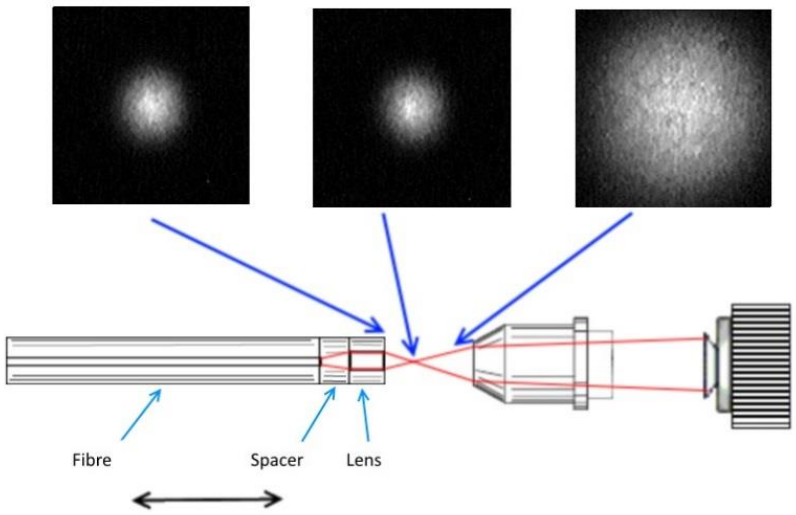

Figure 9.6 - Experimental setup for characterization of nanostructured microlenses.

The first experiment was conducted for bare fibre without any optical element attached. The results are shown in Figure 9.8.

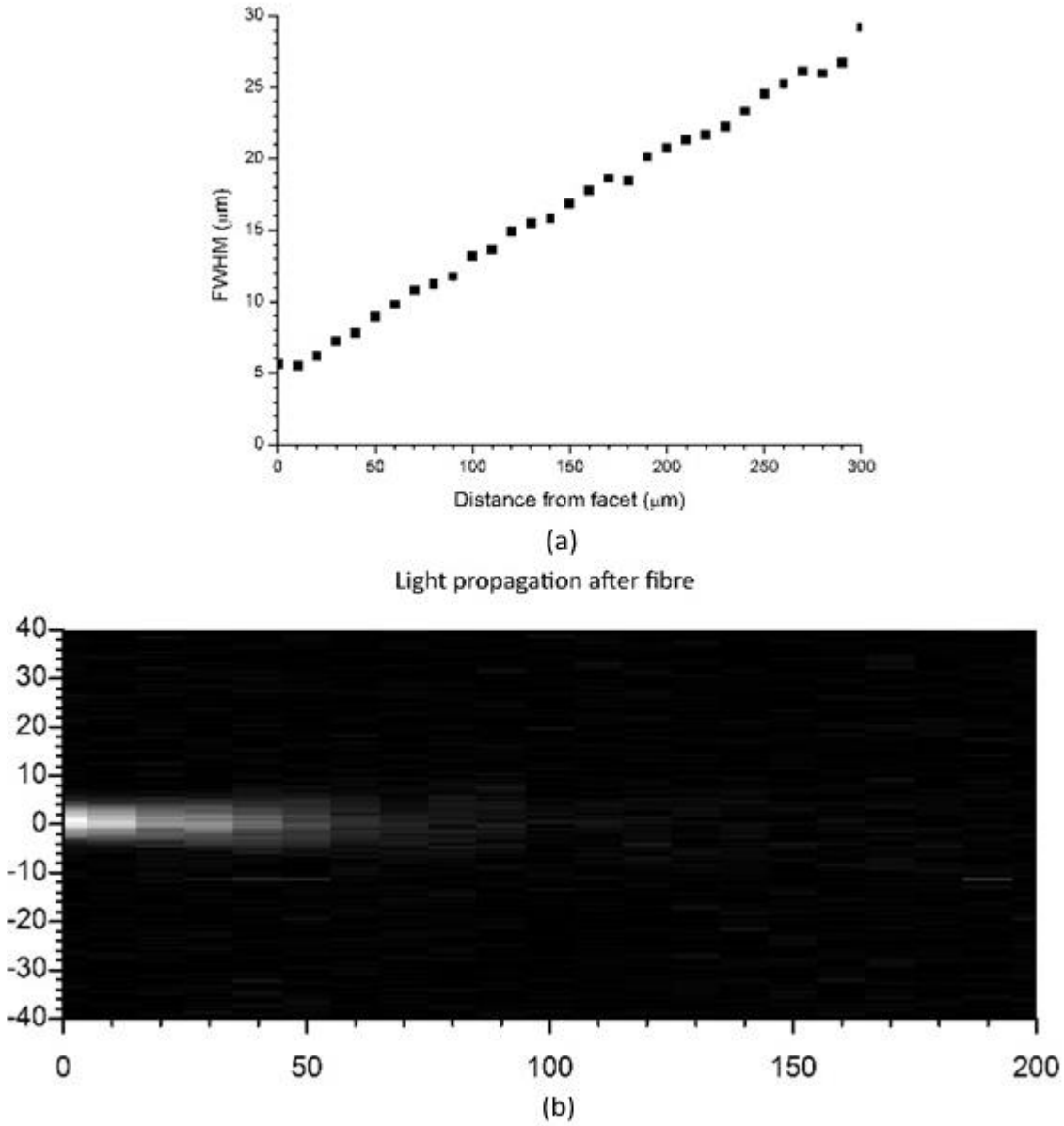

Figure 9.7 - Beam propagation after the end plane of the optical fibre used in the experiments. As can be expected there is no waist after the end plane of the fibre. FWHM measurements show a constant increase with the distance from the fibre.

The next experiment was conducted for the nanostructured micro lens (Fig. 9.8).

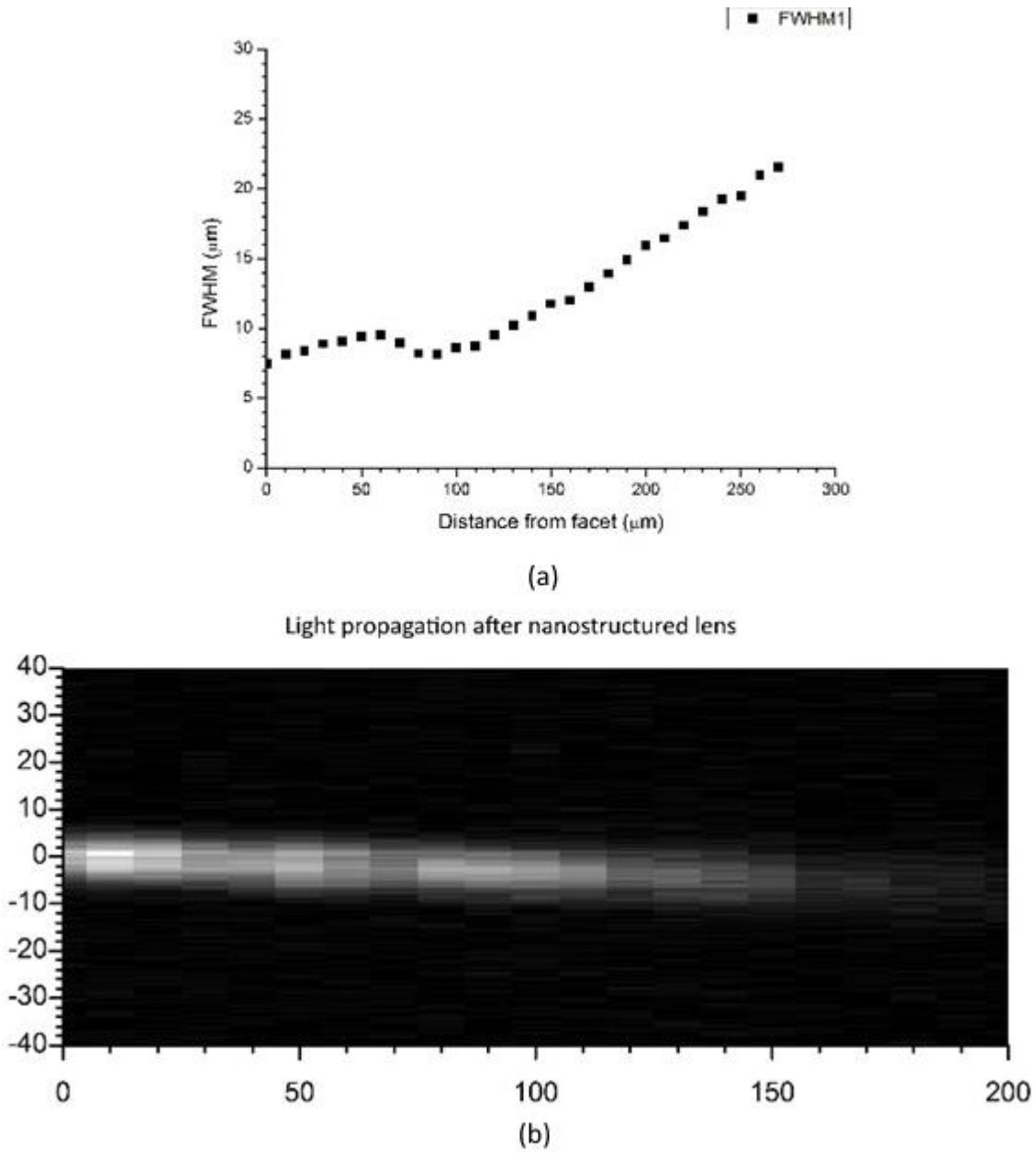

Figure 9.8 - Beam propagation after the end plane of the nanostructured lens used in the experiments. The lens is 11.9μm long, with spacer 71.5μm long. The diameter of the lens is 19.4μm. (a) FWHM measurements, (b) light intensity registered by the camera.

A well-defined beam waist at the working distance of 80μm can be seen. (Fig. 9.8).

9.3. Conclusions

The fabricated lenses were designed to approximate a continuous refractive index distribution instead of step-index one. The fabricated lens was 11.9μm long, which is well below quarter pitch length of the lens. Simulations show that for such a short lens we should expect a focal plane which is positioned away from the lens (more than 40μm depending on the diameter of the lens and the lens distance from the fibre). Experiment

shows the focal plane at a working distance of 80μm, which corresponds to the simulations. At that distance the full width half maximum (FWHM) of the focal spot is equal to 8μm. When compared to the results obtained from the bare fibre, which FWHM equals to 11μm it is an improvement.

10. SMALL NANOSTRUCTURED GRIN AXICON

In the last test of the new optical elements, simulations and experimental verification of the nanostructured axicon were performed. The experimental and computational set up was the same as described previously for the nanostructured microlenses in Chapter 9. First a series of simulations was performed to find the best axicon length and the length of the spacer used between axicon and fibre. This is described in section 10.1. In section 10.3 the results of experimental verification are shown. A nanostructured axicon, with a diameter of around 20μm was attached to the optical fibre. Experiments were performed for two axicons. The first axicon tested was 22.7μm long and with a spacer 17.6μm long. The second axicon was 32.1μm long, with an attached spacer 78.0μm long. Experiments were conducted for the 1550nm wavelength incident light.

10.1. Numerical verification of the nanostructured axicon

The next set of simulations was performed to see how beam propagation changes with the length of the nanostructured axicon. The spacer used in these simulations has a length of 100μm. The length of the axicon was changed starting from 20μm, up to 50μm. The results are shown in Figure 10.1.

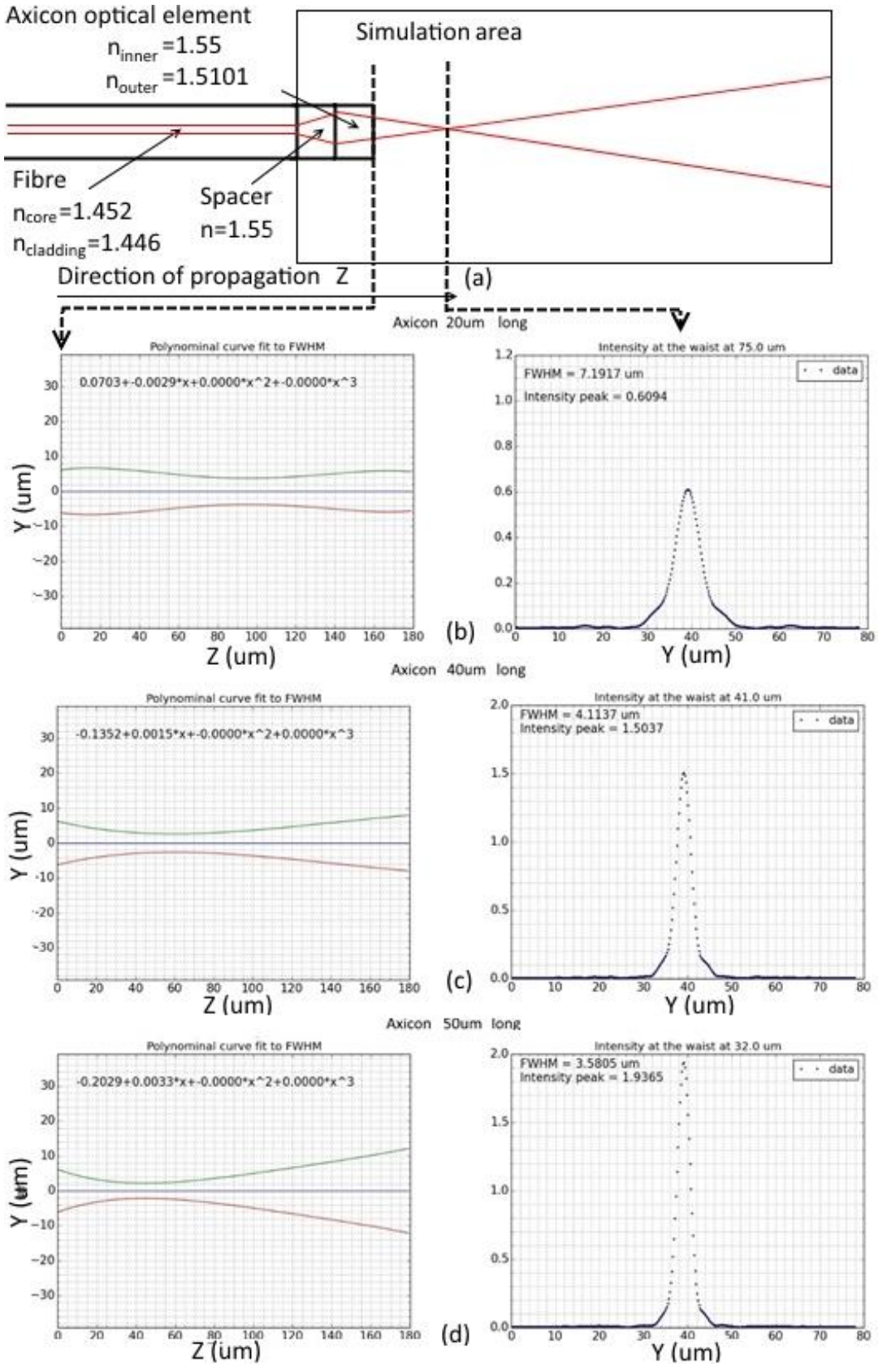

Figure 10.1 - Beam propagation after end plane of the optical element attached to the fibre with NC34 spacer positioned in-between. Fibre has a core diameter 4.6µm and 400µm length. (a) shows schematic of the simulation setup (b) results for the 20µm axicon (c) results for the 40µm axicon, (d) results for the 50µm axicon length. Intensity is normalised to the fibre output.

As can be expected the highest intensity peak, equal to 3.5805 of the intensity at the fibre end, can be observed after the axicon closest to the quarter pitch length – 50μm. The FWHM of the beam in the focal plane is 1.9365μm.

As is explained in Chapter 2.1 the reason for using axicons in this thesis was the possibility of obtaining longer depth of focus compared to the lenses. Figure 10.2 shows comparison of light intensity along optical axis for nanostructured lenses and axicons. In both cases the intensity was averaged over radius of 1μm from the centre of the propagation axis.

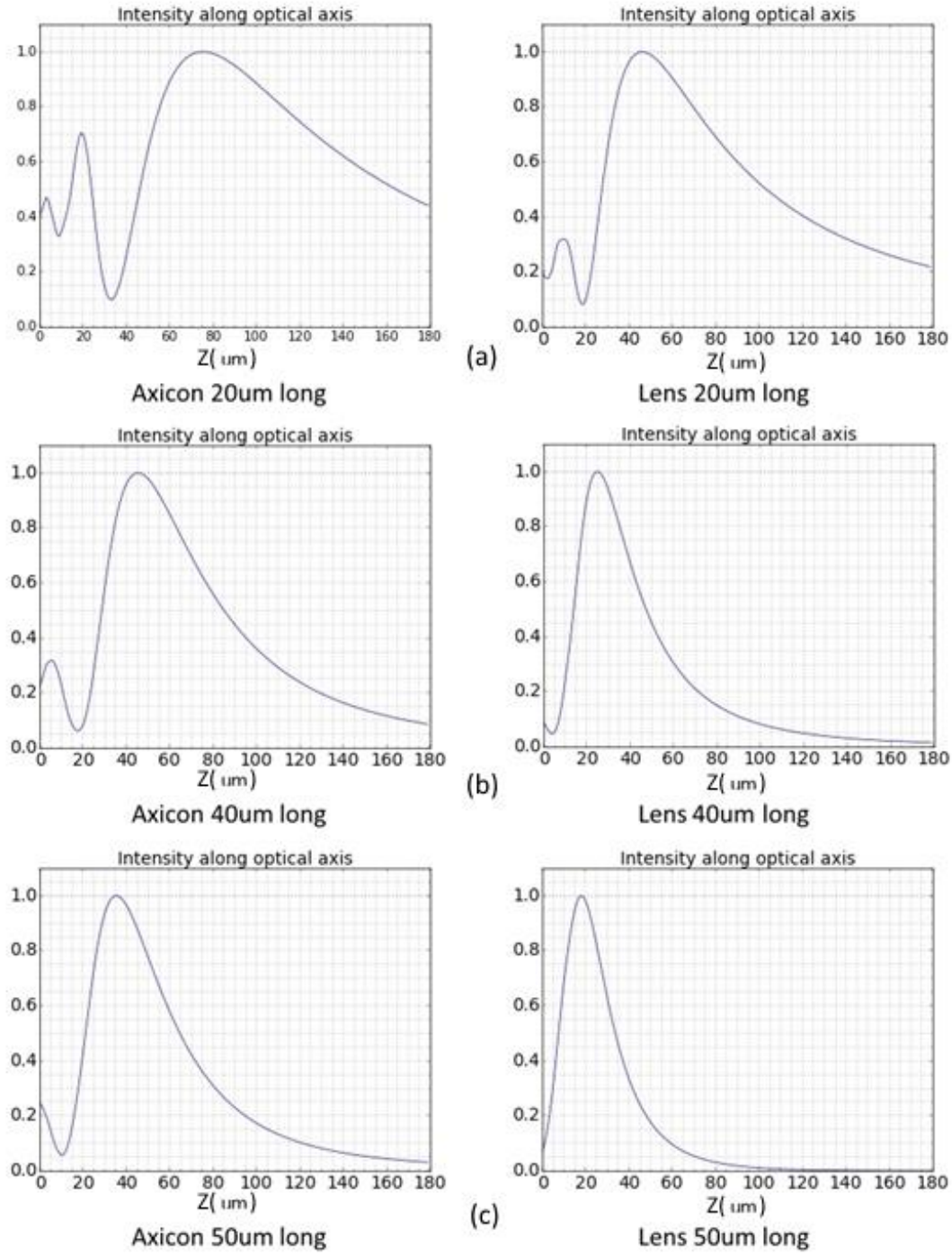

Figure 10.2 - Light intensity along optical axis for axicons and lenses: (a) results for the 20μm length, (b) results for the 40μm length, (c) results for the 50μm length. The intensity is averaged over radius of 1μm from the centre of the propagation axis.

Direct comparison shows that depth of focus, defined as the area where light intensity along the optical path is exceeding 0.7 of the maximum light intensity, is longer for the axicons (Table 10.1).

Nanostructure Length	Axicon	Lens	Difference
20μm	75μm	39μm	36μm
40μm	38μm	21μm	17μm
50μm	29μm	15μm	14μm

Table 10.1 – Comparison of depth of focus for nanostructured axicons and lenses.

The depth of focus for the axicons is between 180% and 193% of the depth of focus for the lenses with the same length.

10.2. Development of nanostructured axicon

The process of optical element fabrication and integration to the optical fibre was described in Chapter 6. For the nanostructured axicon a spacer was fitted between the fibre and the optical element using the same method as for the axicon, described in Chapter 6.

10.3. Experimental results

The fabricated nanostructured GRIN were characterized to verify their effective parameters. The experimental setup was the same as in chapter 8 (fig. 10.3).

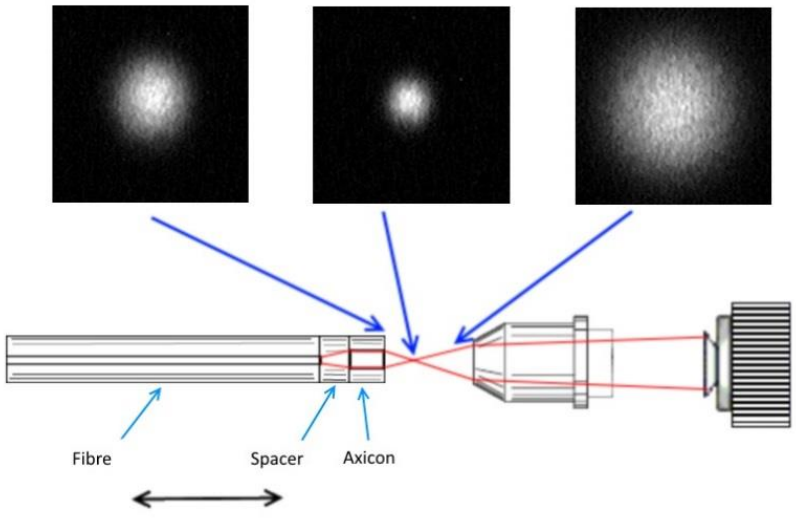

Figure 10.3 - Experimental setup for characterization small nanostructured GRIN optical elements.

First experiment was conducted for the shorter nanostructured micro axicon. The axicon is 22.7µm long, with a spacer 17.6µm long (Fig. 10.4). The diameter of the axicon is 22.9µm.

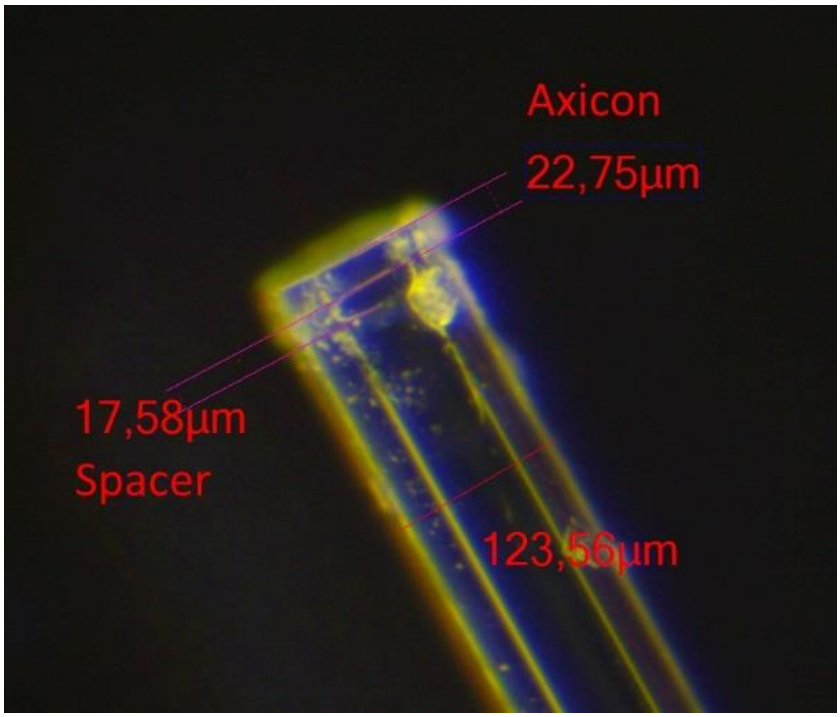

Figure 10.4 - The axicon with spacer attached to the optical fibre.

We have observed a well-defined beam waist at a distance of 20µm from end plane of the axicon. At that distance the FWHM of the beam is 5µm (Fig. 10.5).

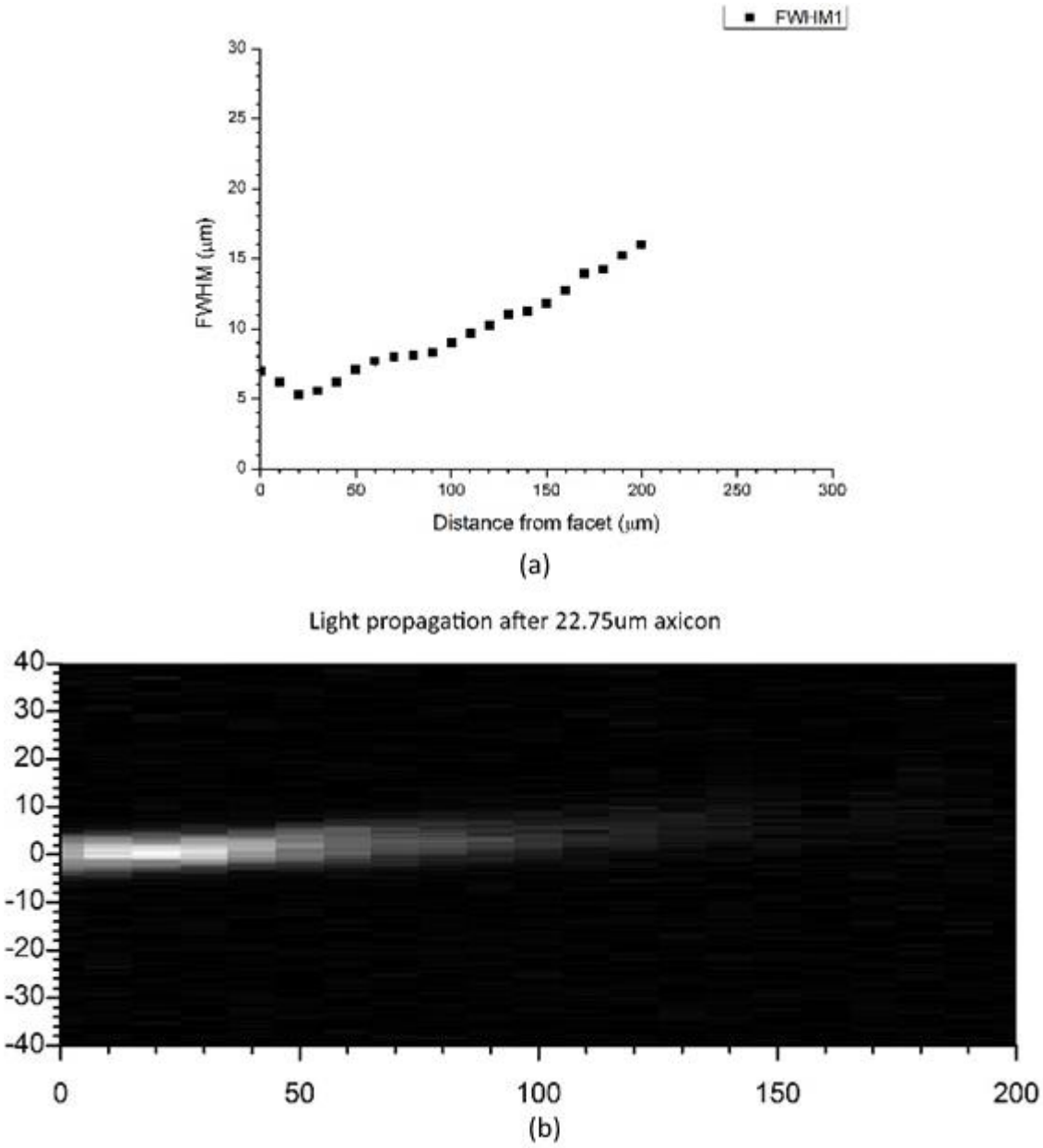

Figure 10.5 - Beam propagation after the end plane of the nanostructured axicon used in the experiments. The axicon is 22.7μm long, with spacer 17.6 long. The diameter of the lens is 22.9μm. (a) FWHM measurements, (b) light intensity registered by the camera.

A FWHM equal to 10μm can be observed at the distance of 120μm. This distance is shorter than what predicted by the simulations in section 10.1 This is the result of the short spacer, for the 20μm long spacer the FWHM of the light intensity illuminating the axicon equals 11μm which is close to half of the axicon diameter. This means that only centre part of the axicon is illuminated.

The next experiment was conducted for the axicon with a longer spacer. The axicon is 32.1μm long, with spacer 78.0μm long (Fig. 10.6). The diameter of the axicon is 22.9μm.

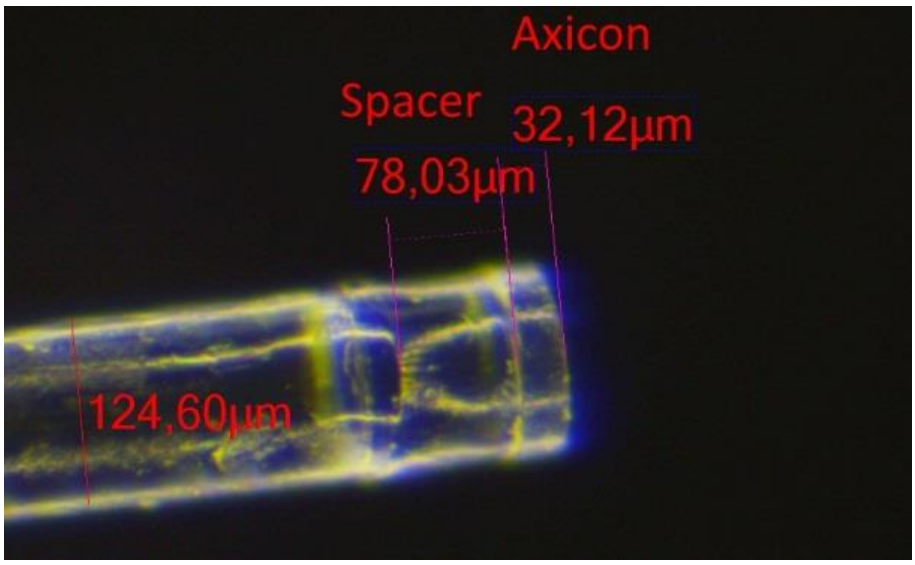

Figure 10.6 - The axicon with spacer attached to the optical fibre.

During experimental verification the beam propagation from the end plane of the axicon was at an angle, suggesting that the attached axicon was not completely parallel to the fibre core (Fig.10.7). This is most likely the result of the spacer not being polished flat-parallel. Due to this all the subsequent measurements had to be adjusted for the off axis propagation of the beam.

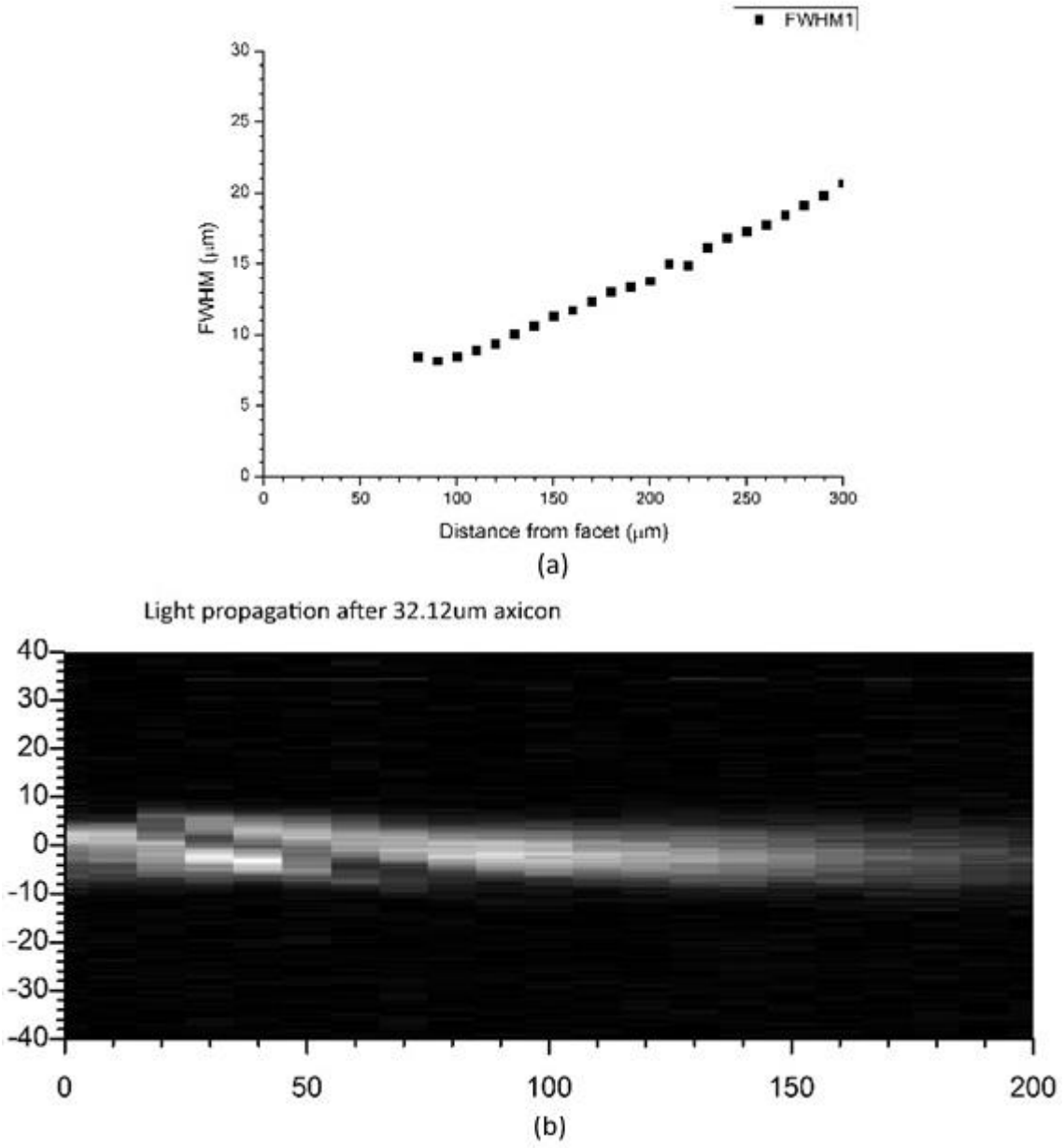

Figure 10.7 - Beam propagation after the end plane of the nanostructured axicon used in the experiments. The axicon is 32.1μm long, with spacer 78.0μm long. The diameter of the lens is 22.9μm. (a) FWHM measurements, (b) light intensity registered by the camera.

For the 32.1μm long axicon the FWHM equal to 10μm can be observed at a working distance of 130μm. Because of the length difference of fabricated elements, there is no possibility of direct comparison of depth of focus between the fabricated lens and the axicon. Fabricated lens with length equal to l_{lens} = 11.9μm has a FWHM equal to 10μm at a distance of D_{lens}=120μm. The axicon with length l_{axicon}= 32.1μm has a FWHM equal to 10μm at a distance D_{axicon}=130μm. As the simulations in section 10.1 show that for axicons with the same length as lenses $l_{axicon} \leq l_{lens}$ the depth of focus should be longer $D_{axicon} > D_{lens}$.

10.4. Conclusions

The first axicon tested was 22.7μm long with a 17.58μm spacer. The experiment confirmed the operation of the axicon with a beam waist at 20μm from the end plane of the element. At the waist beam, the FWHM is equal to 5μm. A FWHM equal to 10μm can be observed at the working distance of 120μm. This value is below that predicted by the simulations due to the fact that the refractive index distribution at the centre of the axicon differs from ideal refractive index distribution, as explained in Chapter 4.

The second of the tested axicons was 32.1μm long with a 78.0μm spacer. It shows severe asymmetry in light propagation. This was most likely caused by the fact that the spacer used is not completely flat-parallel. At a working distance of 130μm the FWHM of the beam is still 10μm, while for the fibre at that distance it was 15μm. The depth of focus for the l_{axicon}= 32.1μm axicon is longer then depth of focus for the l_{lens} = 11.9μm lens, which shows a significant improvement of the depth of focus.

11. CONCLUSIONS

As has been mentioned in the first Chapter the main theme of the thesis and thereby its main goal was the numerical and experimental verification of the concept of the fibre integrated nanostructured micro-optical elements.

Numerical verification of the fabricated elements shows that both nanostructured axicons and lenses are a good approximation of the axicons and lenses with continuous refractive index distribution. The best results from the SA algorithm correspond to lenses with 3.9% longer pitch length then the ideal lenses. With the increased length of the elements the effectiveness of the optical element decreases. In the ideal lens the field amplitude in the second focal plane along the propagation path is equal to 80% of the amplitude in the first focal plane. For the nanostructured lens the amplitude in the second focal plane is equal to 66% of the first focal plane amplitude. This suggests that the discrete distribution of nanorods cannot ideally replicate the ideal refractive index distribution. This implies that the refractive index distribution in the nanostructured lens is not ideally radial, resulting in additional light scattering inside the nanostructured element.

We were able to find two pairs of glasses that could be used in the fabrication of the nanostructured elements used in this thesis. Both the F2/NC21 and NC21/NC34 glass pairs provided us with a small enough refractive index difference, 0.085 and 0.0333 respectively. Both glass pairs have similar transition temperatures and expansion coefficients that allows them to be processed together in the drawing tower using the stack and draw method. The NC21/NC34 pair of glasses have an expansion coefficient difference of $\Delta\alpha=0.4\times10^{-7}$ K^{-1} while the F2/NC21 pair which has an expansion coefficient difference of $\Delta\alpha=5.3\times10^{-7}$ K^{-1}. For NC21/NC34 the difference in the curvature temperature is $\Delta Tc=50^{o}C$ and difference in the sphere temperature is $\Delta T_{kph}=35^{o}C$. The F2/NC21 pair of glasses has $\Delta T_{c}=100^{o}C$ and $\Delta T_{kph}=35^{o}C$. Those parameters allow both of these glass pairs to be safely jointly processed in the drawing tower.

While the basics of MMA polymerisation are well known, the exact process of obtaining optical grade PMMA that can be used after multiple thermal processes is kept a secret by manufacturing companies. By the end of the work on PMMA in this thesis the developed material was clear with transmission reaching 90%. Our knowledge of the exact chemical composition of the polymer allowed the development of doped PMMA with similar thermal and mechanical properties. Samples of BEN doped PMMA with refractive index different from clear PMMA were fabricated. Based on this work, further research will

allow the development of similarly doped PMMA materials with specific optical properties.

Two tests that concluded our preliminary PMMA research showed that it is possible to use PMMA in the stack and draw method, during which PMMA can be subjected to multiple thermal processes. The first showed that air-polymer microstructures can be obtained using multiple thermal processes. The second test shows that it is possible to jointly thermally process two separate polymers. Both of those tests show the future possibility of using two distinct polymer materials for creating various photonic and micro-optical structures utilising the stack and draw method.

The stack and draw method can be used for the fabrication of small diameter nanostructured optical elements. Due to the constraints of the used furnaces the external diameter of the final nanostructures is around 20μm, while the diameter of the whole element is comparable to that of industry standard optical fibre – 125μm. Such elements can be successfully cut, ground and polished in order to create optical elements with previously designed external dimensions. A three step process allows the preparation simultaneously of up to 30 elements for integration. Each optical element is actively aligned with the fibre with a ±2μm precision and then attached using UV-hardening optical cement. This integration method allows the attachment of multiple optical elements to the optical fibre.

By modifying the drawing process from two stage to three stage, larger optical elements can be fabricated. We have used nanostructured metarods composed of subwavelength scale glasses to create 5 artificial materials with a graded change in their refractive index. A preform of a 7-level graded index lens with elliptical shape was created. Thanks to the large capillaries with vacuum applied during the drawing process this structure has been stretched, resulting in an astigmatic step-index profile 75×125μm at the diagonals. This shows that by positioning air capillaries in a specific pattern during the preform assembly stage various shapes of the final structure can be obtained.

Computer simulations performed for the 125×75μm lenses show that the quarter pitch of the elliptical lenses is 190μm and 300μm for the orthogonal axes of the ideal GRIN elliptical lens, and 175μm and 295μm for the orthogonal axes of the quantized GRIN elliptical lens. Both simulations show good agreement and minor differences in effective parameters. Experiments were performed for the 140μm and 170μm length of lenses, which corresponds to 0.18 and 0.22 pitch length respectively for the incident wavelength of 1550nm. For the 140μm microlens we obtained working distances of 90μm and 200μm

for both orthogonal axes, respectively. For the 170μm lens the working distances for both orthogonal axes were 90μm and 180μm, respectively. Experiments performed with a 630nm laser source show that there is no observable focusing behaviour at this wavelength. This is in line with the theoretical predictions, which state that the feature size of the 'metarods' used for the development of the quantized elliptical GRIN lens are too large with respect to the wavelength, and in order for the lens to work the incident wavelength has to be 1550nm.

The fabricated lenses were designed to approximate a continuous refractive index distribution instead of a step-index one. The fabricated lens is 12μm long, which is well below the quarter pitch length of the lens. Simulations show that for such a short lens we should expect a weak focal plane which is positioned away from the lens (more than 40μm depending on the diameter of the lens and distance from the fibre). Experiment shows a focal spot 80μm from the end plane of the lens. At that distance the full width at half maximum (FWHM) of the focal spot is equal to 8μm. When compared to the results obtained from the bare fibre, a significant improvement is clearly visible.

The first tested axicon was 22.75μm long with an 18μm spacer. This relatively short spacer meant that light propagating through the axicon only illuminated its centre. Because of the structured nature of the axicon the tip of the gradient index distribution could not be as sharp as in the ideal axicon and the nanostructured element worked as a small lens. Experiment confirmed this, and the fact that it focuses light, with a beam waist 20μm from the end plane of the element. At the waist beam the FWHM is equal to 5μm.

The second of the tested axicons was 32μm long with a 78μm spacer. It showed severe asymmetry in light propagation. This was most likely due to the spacer not being completely flat-parallel. Due to this the optical element was attached at an angle to the fibre, resulting in the beam being propagated off of the optical axis. Despite this it was clearly visible that the light was focused by the optical element. At 90μm from the end plane of the axicon the FWHM of the beam is still 9μm, while for the fibre at that distance it was 11.5μm.

11.1. Future Work

In Chapter 4 of this thesis the polymerisation process that produced two PMMA based polymers with different refractive indices was described. To the best of our knowledge there are no commercially available PMMA material pairs that have a large difference in refractive index and are fabricated with the processing in the drawing tower at the same

time (similar viscosity and drawing temperature) in mind. Procedures of polymerisation and doping developed during this project can be modified to obtain other pairs of polymers, with different refractive indices. At the same time a stack and draw method that is taking into account the different properties of PMMA based materials will allow the simultaneous processing of such materials. Those procedures may be applied to any refractive index distribution which may in the future allow the creation of diverse photonic structures out of polymers in a similar manner to that currently used for glass.

The integration procedure has been successfully used to attach two optical elements (spacer and lens/axicon) to the optical fibre. The nature of this procedure allows an easy increase in the number of the attached elements. The integration of several optical elements to the optical fibre would allow better control of the shape of the propagating beam. The challenge in this research would be to increase the nanostructured elements effectiveness. Further optimisation of the nanostructured elements can be made possible with the increase of the computing power allocated to the simulated annealing.

In this thesis all of the structures were assembled by hand. This process is time consuming and the procedure is prone to errors. A mechanical/robotic assembly platform could simplify and speed up the preform assembly. The main challenge would stem from the fact that assembled nanorods are not uniform in diameter. The differences can be of the order of 10% diameter. When the structures considered have 100 rods on the diagonal of the hexagon the compound error from those differences can severely warp the assembled structure.